USING THE 1.64 MICRON [Fe II] EMISSION LINE TO DETECT SUPERNOVA REMNANTS IN NGC 6946

by

Justice E. Bruursema

A dissertation submitted to The Johns Hopkins University in conformity with the requirements for the degree of Doctor of Philosophy.

Baltimore, Maryland

August, 2014

Abstract

In the infrared (IR), shock models indicate, and observations show that supernova remnants (SNRs) emit strongly in [Fe II] at 1.64 μm. This thesis reports the results of a search for SNRs in NGC 6946 relying on [Fe II] 1.64 μm line emission, where we employed an adjacent $[\mathrm{Fe\,II}]_{\mathrm{Off}}$ filter to accurately assess the local continuum levels. In this study, we used the WIYN High Resolution Infrared Camera (WHIRC) on the WIYN 3.5m telescope to image NGC 6946 in broad bands J and H and narrow bands [Fe II], $[\mathrm{Fe\,II}]_{\mathrm{Off}}$, Pa$\beta$ and Paβ_{Off}. From our search, we have identified 72 supernova remnant candidates (SNRcs), 11 of which are coincident with sources found in prior radio, optical and/or x-ray studies. Six of the 11 coincident sources were specifically classified as SNRs in their respective studies. The measured [Fe II] luminosities of our SNRcs range from 4.02×10^{35} to 2.09×10^{37} erg s^{-1} and are among the highest of previously published extragalactic SNR [Fe II] luminosities. Using the measured [Fe II] luminosities, we calculate an estimated SN rate of 0.078 yr^{-1} for NGC 6946, which is comparable to the observed rate in the last 100 years of 0.09 yr^{-1}. We also compare our SNR candidates with SNRs that have been found at radio, optical and X-ray wavelengths. All of the candidates now need to be confirmed spectroscopically. However, the fact that we detect as many objects as we did, suggests that [Fe II] can be used as an effective search tool to find extragalactic SNRs.

Advisor: Margaret Meixner.

Acknowledgements

Any acknowledgement for my achievement in an education focused on physics must begin with the source of my interest, inspiration and support, Bruce Esser. An inspirational physics teacher at Marian High School in Omaha, NE, Bruce Esser went above and beyond the call of teaching to show that he cared deeply about his students and wanted them to have every opportunity in life and always be avid self-thinkers. Teaching at an all-girls Catholic school, he cleverly discarded the usual second semester physics material (after asking our class's opinion) and taught us astrophysics, quantum and subatomic physics, at which point I was hopelessly and inexorably drawn to physics.

Propelled with endless energy through my undergraduate education, I however encountered difficulties as my PhD program began. I would have never continued on without the words of support and encouragement from a dear advisor, Dr. Holland Ford. His friendship and offers of support meant everything to me at a time when I faced tremendous difficulties in life. Additionally, my mother, Ronnie J. Darling has ever increasingly become a grounding source of love and support and as such I am ever more motivated to be a source of pride for her. I also found nothing but support and encouragement from my dearest friends, Tim Brodie and Zhouhan Liang. I thank my mother, Holland, Tim and Zhouhan from the deepest parts of my heart for giving me the emotional support without which I would not have continued pursuing my PhD.

At last, and most certainly not least, I absolutely must acknowledge my dear advisor, Dr. Margaret Meixner, without whom I certainly would not have ever graduated. Margaret served, for me, so many functions, supporting me in every way. In the most essential role, Margaret adapted her mentoring, guidance and supervision approaches to accommodate and account for my particular needs to such a point that I honestly cannot imagine a more perfect graduate advisor. Through her supervision, I believe I was motivated and pushed at the highest level and pace possible which still allowed for me to remain healthy and free of excessive stress. Margaret offered a never ending supply of support, interest, input and attention which I think is well beyond the call of the standard supervisory role in most graduate programs. For that I am eternally grateful and will be in admiration of her.

Contents

List of Tables

List of Figures

For Ronnie J. Darling

Chapter 1

Introduction

1.1 Supernova Remnants (SNRs)

A *supernova remnant* (SNR) is an object consisting of the ejected material from a star which has exploded and circumstellar and interstellar material that has been shocked by the resulting shock wave. SNRs can radiate at many different wavelengths and can have various morphologies, depending on the initial conditions of the progenitor star and surrounding environment. Examples of some local SNRs are shown in Figure 1.1.

In general, when a supernova occurs, stellar material is ejected outward at speeds that approach a noticable fraction of the speed of light (perhaps $.01c$-$.1c$). Considering typical temperatures and compositions of the intersteller medium (ISM), such speeds are most certainly highly supersonic. Consequently, a shock wave propogates which largely has the effect of heating the ISM. Dust grains can be destroyed, introducing heavier elements into the ISM in gaseous form, while atoms can be ionized and excited. The shock wave also accelerates electrons, protons and ions to speeds that approach the speed of light creating what we call *cosmic rays*. The ejection of material from the exploded star also distributes heavy elements throughout the ISM. The shock wave slows as it expands and the energy from the explosion is absorbed by the ISM and radiated away through multiple radiative processes. Eventually, the energy dissipates to the point that the speed of the shock front falls below the local speed of sound.

1.1.1 SNR phases

As the process discussed above occurs, the supernova remnant passes through a number of evolutionary stages. Generally, we can categorize these into 4 phases (Shu 1992; Vink 2012; Woltjer 1972):

I. The ejecta dominated phase: In this initial phase, the mass ejected by the supernova (M_{ej}) is greater than the mass which has been swept up by the shock wave (M_{sw}) (see Figure 1.2 for a schematic diagram of these variables). As long as $M_{sw} \ll M_{ej}$, then the velocity of the shock front (v_s) remains relatively constant. Owing to this largely constant expansion velocity, this phase is sometimes referred to as free expansion, although sometimes it is called the blastwave phase. As M_{sw} increases, the pressure of the shocked ISM material eventually exceeds the thermal pressure of the ejecta and a reverse shock begins to propogate inward from the shock front, heating the previously unshocked ejecta. This phase can last up to a few hundred years.

II. The Sedov-Taylor phase: In this phase, $M_{sw} > M_{ej}$, but radiative losses are not yet energetically significant within the shock radius, so the expansion process remains approximately adiabatic and energy is conserved. The reverse shock has propogated to the origin of the explosion leaving much of the material within the shock radius highly ionized and heated . The ejecta become mixed up with the gas that was just shocked which enhances the magnetic field within the shock radius. The increasing magnetic field creates an increase in the SNR's synchrotron radiation. This phase lasts on the order of 10^4 years.

III. The pressure-driven phase: In this phase, radiative losses become significant. As temperatures drop below $\sim 10^6$ K, electrons start to recombine to form heavier elements. This process causes the formation of a thin, dense shell which surrounds the SNR's hot interior. Figure 1.2 displays the progression of forming this dense shell. In theory, the shell's momentum is conserved. Observationally, the pressure from the hot material within the shell is found to be large enough to add a significant push to the expanding shell material. Appropriately, this phase is sometimes referred to as the radiative phase or "snow plough" phase.

IV. The merging phase: In this final phase, the supernova remnant slows to the speed of the random velocities of the surrounding ISM. The end of this phase marks the

nominal end of a SNR's existence, which, depending on the particular ISM in question, could potentially be some hundreds of thousands up to some millions of years after the original supernova event.

The phases outlined above roughly describe the evolution of a SNR, however inhomogeneities in the ISM, previously ejected stellar matter and other factors can contribute to complex types of SNRs where different parts of the SNR could be in different phases at the same time. Notably, Rayleigh-Taylor instabilities will disrupt the shock front, causing the formations of filimentary-like structures as can be seen in Figure 1.3. Figures 1.1 and 1.3 display complex morphologies observed in local SNRs. Clearly, the SNRs in these Figures, like the SNRs we will study in this thesis, are radiating substantially and therefore alre most exclusively expected in to be in the pressure-driven phase.

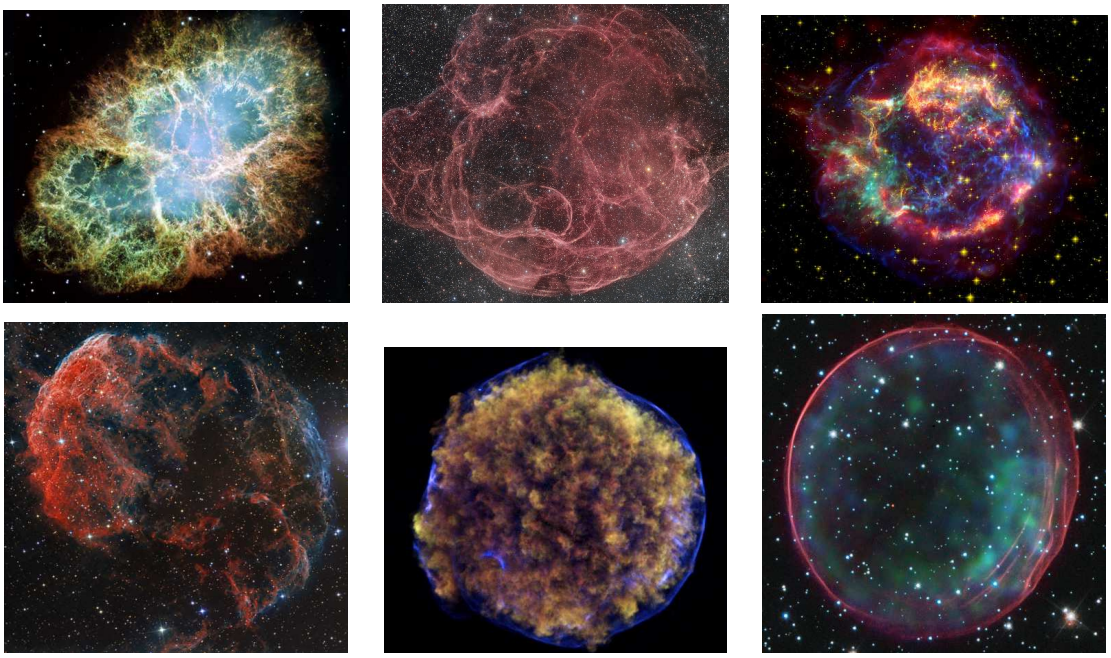

Figure 1.1 These APOD[1] images display some of the complex morphologies observed in local SNRs. From top left to bottom right: (1) The Crab Nebula from HST, APOD Dec 2 2005, (2) Simeis 147 showing Hα and [O III], APOD Feb 12 2011, (3) Multi-epoch Cass A image with Spitzer, APOD June 15 2005, (4) IC443 showing Hα and [O III], APOD Jan 9 2013, (5) Tycho's SNR with Chandra, APOD April 30 2011, (6) SNR 0509-67.5 combined HST and Chandra image, APOD Jan 12 2012.

[1]http://apod.nasa.gov is originated, written, coordinated and edited since 1995 by Robert Nemiroff and Jerry Bonnell

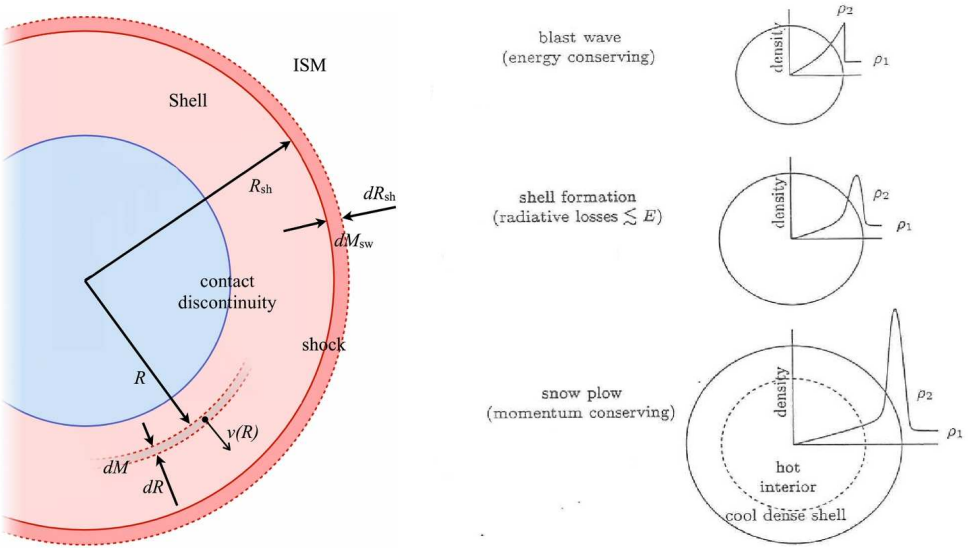

Figure 1.2 *Left:* A schematic of a SNR at a time, t, as it expands through the ISM and sweeps up mass. *Right:* Phases of a SNR indicating density as a function of radius to highlight the formation of a dense shell in the snow plough phase (Shu 1992).

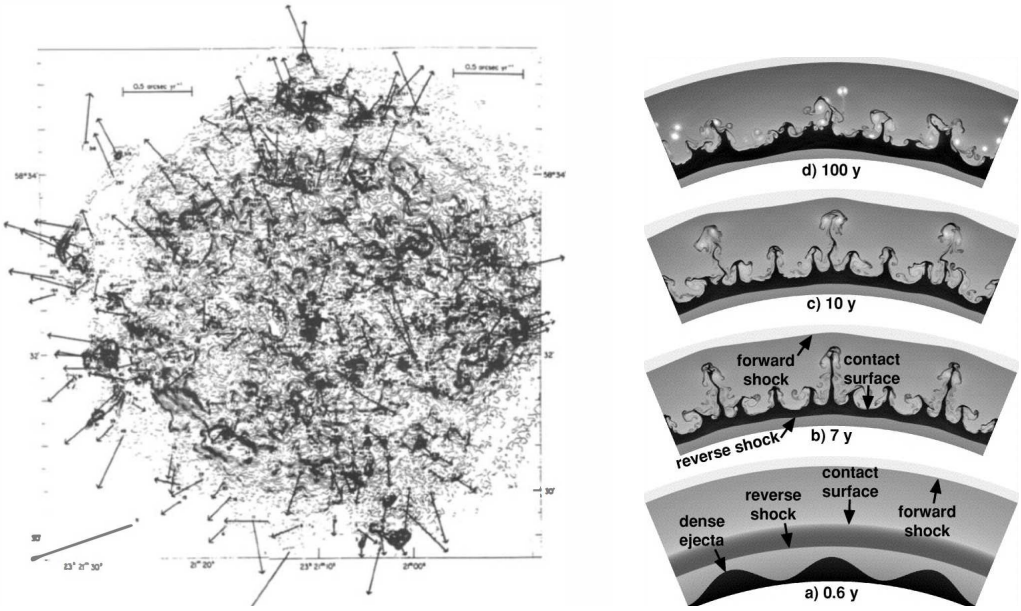

Figure 1.3 *Left:* An image of CasA with arrows indicating the direction of proper motions of emitting material as found in the multi-epoch image from Chandra portrayed in Figure 1.1. Note the complex morphology of the SNR. (Weiler & Sramek 1988) *Right:* A representative diagram of the formation of Raleigh Jeans instabilities which form in the dense shell during the snow plough phase, further complicating a SNR's morphology (Kane et al. 1999).

1.1.2 SNR types

In addition to evolutionary phases, SNRs are often classified based on their appearance or morphology in various wavebands. The three primary classes are: *shell type*, *plerionic* or *composite*. Shell type SNRs are characterized by a limb brightened shell showing the shock heated plasma created by the passage of the supernova's shock wave. Most of their radiation originates from this shell of shocked material. A clear example of a limb brightened shell can be seen in the image of SNR 0509-67.5 in Figure 1.1. A strikingly different morphology can be seen in the image of the Crab Nebula in the same figure. The Crab Nebula is classified as a plerionic SNR, and as the most famous plerion, many plerionic SNRs are referred to using the term *crab-like*. The appearance of these SNRs is created by a wind of relativistic electrons and protons originating from the rotating neutron star remnant of the supernova progenitor. This is known as a *pulsar wind nebula* and is why a plerionic SNR emits most of its radiation from within the region interior to the expanding shock wave shell. It follows, then, that composite SNRs have both a clearly visible shell and also a pulsar wind nebula. The shell-like and crab-like appearance is often seen at differt wavelengths and so-called *thermal composite* remnants are specifically those found to be crab-like in X-ray emission and shell-like in at radio wavelengths.

1.1.3 Studies of SNRs

Studying supernova remnants (SNRs) can help us understand topics such as the origin of cosmic rays, the structure and composition of interstellar media, star formation rates, star formation histories, and more. Detailed galactic studies of individual SNRs help us understand topics like these on small scales and reveal the intricate nature of SNRs, but are also complicated by uncertainties in distance and high absorption or extinction (see Magnier et al. 1995, for a review). Extragalactic studies can be less affected by these difficulties and can inform our knowledge on a less-biased, more global scale. Extragalactic studies of SNRs are greatly affected by the number of observable SNRs, thus there is a need for an efficient method of locating the most complete sample of SNRs we can find.

Past searches for extragalactic SNRs have generally been based on optical, radio and/or x-ray observations. Optical searches look for excited ionized species and usually measure [S II]/Hα flux ratios. This ratio is higher in most SNRs than in H II regions because most

of the sulfur in H II regions exists as S^{++} (Mathewson & Clarke 1973; Long et al. 1990; Matonick & Fesen 1997, hereafter MF). SNRs can also be differentiated from H II regions with radio observations where synchrotron emission caused by the magnetic field of the SNR causes its radio spectrum to be more steep than the flatter spectrum of the thermal environments of the galactic ISM. Thus SNRs are identified in the radio as discrete sources of strong radio emission with a specified spectral index, α, of their energy spectra $S = \nu^{+\alpha}$ (non-thermal emitters) (Gordon et al. 1999; Hyman et al. 2000; Lacey & Duric 2001). It is also expected that at least the young SNRs, if not others, will be sources of strong, localized x-ray emission since the shock from a supernova explosion can raise local temperatures to 10^6-10^7 K as it collides with the surrounding interstellar medium (ISM) (Itoh & Masai 1989).

1.2 Using [Fe II] to Search for SNRs

Infrared (IR) emission lines can also be used to identify SNRs, but have been used to a much lesser extent than the methods listed above. However, it has become clear that SNRs are linked to strong emission of [Fe II], most notably at λ=1.64 μm (Oliva et al. 1989). Dust in the ISM of a galaxy contains iron, and when the fast shock of a SNR propagates through the interstellar material, the dust grains are destroyed which introduces gaseous iron into the ISM. This gas-phase iron can be excited through collisions (Greenhouse et al. 1991). It has also been suggested, based on a detailed study of the crab nebula, that UV and x-ray heating from photoionization could account for a portion of the [Fe II] emission from SNRs as well (Graham et al. 1990). Regardless, [Fe II] emission is certainly prevalent in SNRs, and is virtually absent from H II regions. A study by Alonso-Herrero et al. (2003) reported as much as 70% of the total [Fe II] 1.64 μm flux in two nearby starbursting galaxies was associated with SNRs while only 6-8% was from H II regions. Thus, [Fe II] can be used as a diagnostic tool in identifying SNRs. Additionally, searches for SNRs using [Fe II] may be more efficient than optical searches in cases where significant reddening or extinction along the line of sight is present.

Table 1.1. Historically Observed SNe in NGC 6946.

Name	Peak Mag	Position (arcsec)		Type	Discovered by	Discovered on (DD.MM.YYYY)
SN 1987A	14.6	37 W	105 S	II	Richley	19.07.1917
SN 1939C	13.0	215 W	24 N	II	Fritz Zwicky	17.07.1939
SN 1948B	14.9	222 E	60 N	II	Mayall	06.07.1948
SN 1968D	13.5	45 E	20 N	II	Wild and Dunlap	29.02.1968
SN 1969P	13.9	5 W	180 S	II	Rosino	11.12.1969
SN 1980K	11.4	280 E	166 S	II	Wild	28.10.1980
SN 2002hh	15.0	61 W	114 S	II	LOTOSS project	31.10.2002
SN 2004et	12.3	247 E	115 S	II	Stefano Moretti	22.09.2004
SN 2008S	18.0	53 W	196 S	IIn-pec	Ron Arbour	01.02.2008

Note. — This table lists the nine historically observed SNe in NGC 6946 from the last century. Positions are reported in arcseconds from the center of the galaxy. The coordinates of the galactic center are listed in Table 1.2.

1.3 The Starburst Galaxy NGC 6946

Our selected target is the galaxy NGC 6946, sometimes called the 'Fireworks Galaxy'. This name comes from the high number of supernovae that have been observed in NGC 6946 throughout the past century, in comparison to other galaxies. As seen in Table 1.1, there have been 9 observed SN in NGC 6946 over the last ∼90 years, leaving us with a lower estimate for its SN rate which is very much higher than any other local measured or calculated galactic SN rates. NGC 6946 makes an ideal candidate for our study for a few different reasons. First, referring to values in Table 1.2, NGC 6946 is an intermediate sized galaxy which is relatively close and largely face on. This allows for high resolution imaging through lines of sight that have low reddening and extinction internal to NGC 6946. Additionally, NGC 6946 has a well documented high star formation rate (Kennicutt et al. 2009) which implies a potentially abundant field of SNRs to study. Finally, NGC 6946 has been a target of SNR searches in the past (Lacey & Duric 2001, MF), which allows us to correlate our findings with those from other wavelength regimes, as will be described in more detail within Sections 2.4 and 3.4.2 of this thesis.

Table 1.2. Properties of the Starburst Galaxy NGC 6946.

Parameters	Values	References
Position (J2000)	RA=$20^h34^m52.3^s$/DEC=$+60°09^m14^s$	Evans et al. (2010)
Distance	5.9 ± 0.4 Mpc	Karachentsev et al. (2000)
Inclination	38°	Carignan et al. (1990)
Galaxy Type	Sc	Larsen et al. (2002)
$E(B-V)$	∼0.34	Schlegel et al. (1998)
$A_{\rm H}$	0.154	Schlafly & Finkbeiner (2011)
H II region SFRs	$\sim10^{-4}$ – $3.1\times10^{-3} M_\odot$ yrs^{-1}	Cedrés et al. (2013)
SFR Densities	∼0.1 – 1.6 $M_\odot$ yrs^{-1} kpc^{-2}	Li et al. (2013)
log(O/H)+12	∼8.2 – 8.7	Gusev et al. (2013) , Cedrés et al. (2012)

Note. — The first six rows of this table report global properties of NGC 6946 or properties along the line of sight to the galaxy. The last three rows of this table give ranges of the various internal properties of NGC 6946 as determined by measurements of H II regions within the galaxy. 'SFR' means star formation rate, where both reported ranges were calculated from extinction corrected Hα methods.

1.4 This thesis

The first major studies of SNRs involving or relying on [Fe II] emission were initially published approximately 20 years ago (Greenhouse et al. 1991; Oliva et al. 1989). However, most [Fe II] emission studies have either been too low in resolution to observe individual SNRs or they have been pointed observations of selected SNR targets from previous data sets in other wavelengths. Two recent studies (Alonso-Herrero et al. 2003; Labrie & Pritchet 2006) have been done that is similar to the work in this thesis, however both studies use other methods to estimate the continuum level in the [Fe II] filter where this study obtains data using a [Fe II]$_{\rm Off}$ filter which is specifically designed to detect the continuum level for the [Fe II] filter. In this way, the work in this thesis is a novel approach to detecting extragalactic SNRs.

The aim of this thesis is to present a list of viable SNR candidates (SNRcs) which have been found using this particular method for locating SNRs, specifically comparing [Fe II] versus [Fe II]$_{\rm Off}$ emission. In this method, objects are identified that emit strongly in [Fe II] while having little to no emission in the [Fe II]$_{\rm Off}$ filter. Backing up these detections with a check on the emission seen in broadbands J and/or H, we can be reasonably confident

that we have found sources of strong [Fe II] emission. As such, the probability that these objects are SNRs is expected to be high, although future spectroscopic confirmations would be needed before that assertation could be made.

Chapter 2 of this thesis reports the results of the initial investigation of this method and the initial list of SNRcs as was published in Bruursema et al. (2014). Chapter 3 describes the follow-up observations that were taken in order to better understand the results and fill in gaps of the original study. Furthermore in Chapter 3, an analysis of the followup observations is given and a final list of SNRcs is presented. A summary of the results of this work is presented in Chapter 4.

Chapter 2

A Search for SNRs in NGC 6946 Using [Fe II]

Note: This chapter is adapted from the text within Bruursema et al. (2014).

2.1 Introduction

This chapter is outlined as follows. In Section 2.2, the imaging and data reduction techniques that produced our mosaiced images of NGC 6946 are discussed. Section 2.3 describes the search method and criteria implemented to find SNR candidates (SNRcs), as well as the method for measuring fluxes. Also in Section 2.3, a catalog is presented of the 48 candidates found in this initioal search, along with their associated fluxes and photometric parameters. Section 2.4 describes how these SNRcs compare in luminosities to [Fe II] observations of SNR populations in the Milky Way, the LMC, and five starbursting galaxies. Section 2.4 also compares the [Fe II] SNRc population to radio, optical and x-ray sources and SNRc populations of NGC 6946. Conclusions from this initial investigation are summarized in Section 2.5.

2.2 Observations and Data Processing

We imaged NGC 6946 in six filters: narrow bands [Fe II], $[\text{Fe II}]_{\text{Off}}$, Pa$\beta$ and Paβ_{Off} and broad bands J and H using the WIYN High Resolution Infrared Camera (WHIRC; Meixner et

Table 2.1. WHIRC Filter Characteristics.

Filter:	J	H	[Fe II]	$[\text{Fe II}]_{\text{Off}}$	Paβ	Paβ_{Off}
λ_c (μm)	1.250	1.651	1.646	1.668	1.280	1.303
$\Delta\lambda$ (μm)	0.1619	0.3009	0.0164	0.0162	0.0158	0.0130

Note. — λ_c lists the central wavelength and $\Delta\lambda$ indicates the filter width for each of the WHIRC filters listed.

al. 2010). $[\text{Fe II}]_{\text{Off}}$ is a filter shifted ∼4500 km s^{-1} redward from the central wavelength of [Fe II] filter, designed to measure the continuum level directly adjacent to the [Fe II] 1.64 μm line, and Paβ_{Off} is similarly shifted ∼4500 km s^{-1} redward from the central wavelength of Paβ filter as seen in Table 2.1, where the center wavelengths and widths of all six filters are listed. The detector was a Raytheon 2048×2048 HgCdTe VIRGO array with a pixel size of 20 μm. The plate scale was ∼0.1″ pixel^{-1} as measured from a distortion corrected image and a single image field of view is 3.3′×3.4′. The H-band imaging observations were carried out through the NOAO open use program (PI: M. Otsuka; ID:2009B-0516). The other WHIRC observations were carried out using STScI guaranteed observation time (P.I.: M. Meixner).

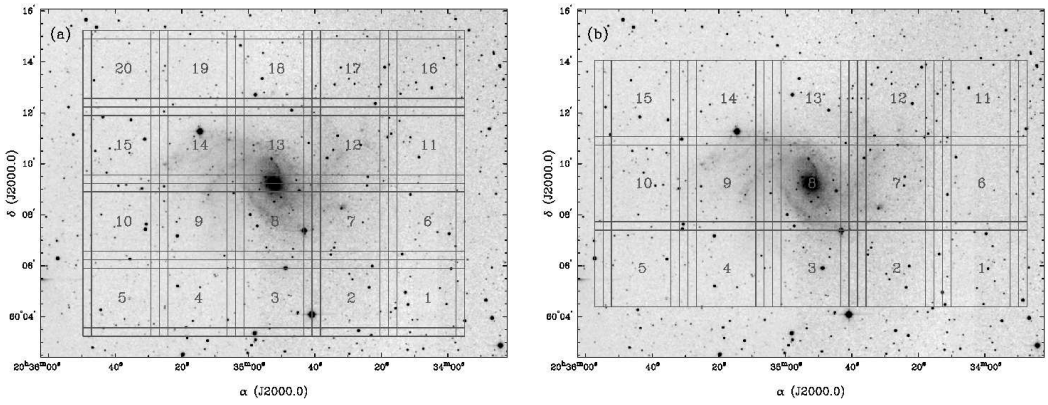

Figure 2.1 (*left*) The mosaic pattern for the broad-band images. (*right*) The narrow-band mosaic map. North is up and east is left. Each pointing is numbered and represents 4 and 3 dithers for the broad and narrow bands, respectively.

Table 2.2. Observation Log.

Band	Obs-Date (YY-MM-DD)	Total Exp. per Pointing (sec)	Mosaic Size (frames)/(′)	N Dithers (Dither Pattern)	Seeing FWHM (″)	Airmass	Comments
J	10-09-25	640	5×4/15×12	4(2×2)	1.4	1.1-1.4	windy, photometric
H	09-08-29	720	5×4/15×12	4(2×2)	0.5-1.0	1.1-1.9	photmetric
[Fe II]	11-06-17	780	5×3/17×10	3(1×3)	0.6-1.1	1.1-1.7	thin clouds
$[\mathrm{Fe\,II}]_{\mathrm{Off}}$	11-06-17	780	5×3/17×10	3(1×3)	0.7-1.2	1.1-1.4	clear
Paβ	11-06-18	480	5×3/16×10	3(1×3)	0.8-1.2	1.3-2.0	clear
$\mathrm{Pa}\beta_{\mathrm{Off}}$	11-06-18	480	5×3/16×10	3(1×3)	0.6-0.9	1.1	clear

Note. — In Column 5, $DitherPattern$ gives the number of images east to west by number of images north to south, the resulting total number of images in a pointing is reported as $NDithers$, and the total exposure time for a pointing is given in Column 3, meaning each image has an exposure time found by dividing the time given in Column 3 by $NDithers$.

Table 2.2 lists the observation parameters, which varied for each filter. The observations were taken from 2009 to 2011 with varying weather conditions, as noted in the last column. The thin clouds noted during the [Fe II] observations resulted in a highly variable sky, which will be discussed later. We selected the Fowler 4 readout mode, which reduces the read noise to $\sim$17 e^-. Exposure times are reported as a total of the number of dithers at each pointing in the mosaic, multiplied by a single image's exposure time. Exposure times per frame are 160 sec for J, Paβ, and $\mathrm{Pa}\beta_{\mathrm{Off}}$, 180 sec for H, and 260 sec for [Fe II] and $[\mathrm{Fe\,II}]_{\mathrm{Off}}$. Originally, we chose shorter exposures and more dithers per pointing, but later moved to longer exposures and less dithers per pointing as we aimed to achieve higher signal to noise. Depending on the filter, we took either 20 or 15 pointings to map NGC 6946, as shown in Figure 2.1. For all observations, the separation between pointings is 180″. The smaller number of pointings in the narrow bands was due mainly to time constraints, and to perform deeper imaging of the main star forming disk of NGC 6946. These observations were the first ones to be done using the WHIRC mosaicing tool, WHOMP. The interface of the telescope with the observating system was being debugged, therefore there are a couple unintended offsets to the J, [Fe II] and $[\mathrm{Fe\,II}]_{\mathrm{Off}}$ mosaics, which resulted in various mosaic sizes, as reported in the fourth column. The seeing measured from stars in the detector was

from $\sim 0.5''$ in H to $\sim 1.4''$ in J, as listed in the sixth column.

The data reductions were done mainly using our house made python script which utilizes various NOAO/IRAF[4] `MSCRED` packages and the `wprep.cl` IRAF script as given on the WIYN/WHIRC web page. The `wprep.cl` script was used on all data as the first step of the process. This script trims off the 96 columns of reference pixels on the right side of the chip, in addition to two rows on the top, then scales the pixel values to 1/4th their value if the camera was in Fowler mode 4, applies a linearity correction to the counts, and finally checks and fixes header keywords if necessary. Next, we created the instrumental normalized flat for each filter by median combining all dome flats taken with the dome lamp on, and subtracting from it the median combination of all the flats taken with the dome lamp off. The `MSCRED` package was then used to remove the pupil ghost from the bias-subtracted flat-field before the flat-fielding correction was applied to the images, which ensured that the signal level at the center of the chip represented its true value. The bias-subtracted and pupil ghost-corrected flat-field was then fixed so that any pixels with very small or negative values were reassigned to have a value of one, and the resulting image was then normalized to one. Finally, all images were flat-fielded (divided by the bias-subtracted flat-field).

The sky subtraction process subtracts a sky image from a pointing in the mosaic. The details of the subtraction varied for the filters and the weather conditions. We did not have dedicated sky fields, and instead, for any spot on the mosaic, a sky field was determined by choosing the pointing that was nearest to the outer edges of the galaxy while also having been taken very close to the same time. In general, the sky level was not largely different between pointings, however it was often found that the sky changed enough over the course of completing a mosaic row, that it was necessary to use both the east-most and west-most pointings of the row as skys for their nearest neighbor. When dealing with a pointing in the center of the mosaic, either the east-most or west-most pointing in the same row could have been used, so the sky field was determined by trying both and taking the better result.

Once a pointing was selected to serve as a sky field, a sky model was constructed by masking the brightest stars in each dither at that pointing, then median combining the dithers. The resulting sky model was scaled by an experimentally determined amount before being subtracted from each image. For the [Fe II] observations, the sky was highly

[4]IRAF is distributed by the National Optical Astronomy Observatories, which are operated by the Association of Universities for Research in Astronomy (AURA), Inc., under a cooperative agreement with the National Science Foundation.

variable from image to image, resulting in more complicated sky modeling, which may have included combining multiple pointings to model the sky. After the appropriately chosen and scaled skys were subtracted from the images, a DC offset correction was applied such that the median sky value at the four corners of the mosaic would be zero, and adjacent frames would have the same median sky value for the same area of sky. In the Paβ, Pa$\beta_{\rm Off}$ and H filters, we sometimes observed fringing, which is the presence of Newton's Rings fringes, most likely due to atmospheric OH emission lines. When fringing was present, a precise scaling of the sky model before sky subtraction was the key to removing this effect, and sometimes required a sky model's scaling constant be determined to the hundredths in accuracy.

In order to fix bad pixels, a single dome flat was chosen and divided by the final bias-subtracted flat. Any pixels in the resulting image that did not have a value very near to one were marked as bad pixels, and were added to the bad pixel map as given on the WHIRC website. The IRAF routine `fixpix` was used to replace all bad pixels with a value based on a linear interpolation along pixels in the same column, or if there were adjacent bad pixels in the same column, then in the same row. Then, using the IRAF tasks `geomap` and `geotran`, in combination with the filter-dependent distortion files downloaded from the WIYN/WHIRC webpage, the images were corrected for the field distortion.

Finally, we corrected minor offsets in each image's world coordinate system. To do this, we measured the positions of at least 40 of the brightest stars in each field using IRAF's `daofind` routine and compared these to positions of stars detected in Two Micron All-Sky Survey (2MASS) in the same field. The positions of 2MASS stars were downloaded using WCSTOOLS. We used WCSTOOLS to correct the coordinate systems of the reduced images to match that of the 2MASS images. To increase signal-to-noise and coordinate accuracy, the images of each filter were combined into mosaics using the mosaicing software Montage[5].

[5]http://montage.ipac.caltech.edu

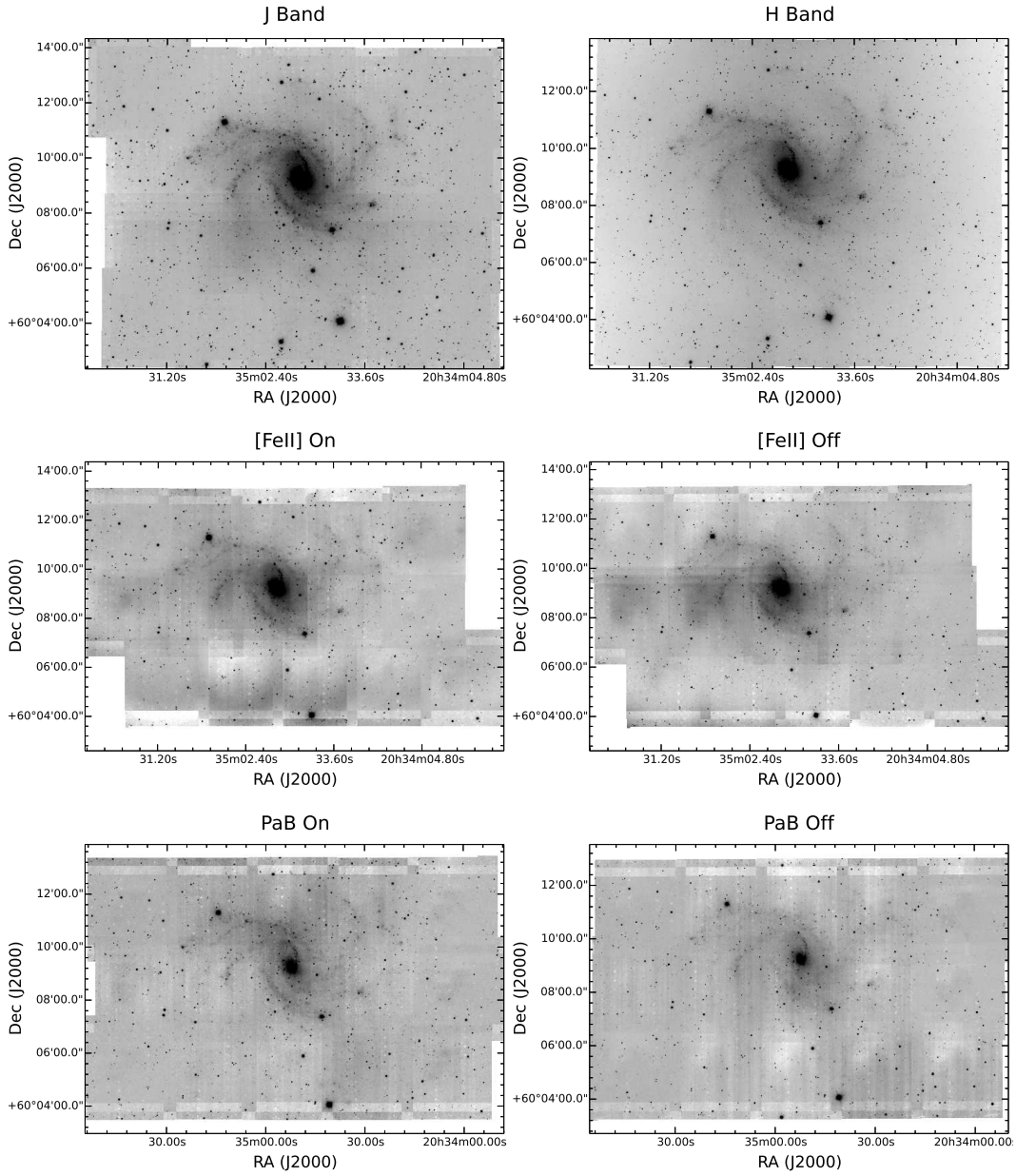

Figure 2.2 Mosaics of NGC 6946 were created from our WHIRC camera imaging in six different bands and are all oriented with north up and east to the left. The J and H broad bands show general continuum levels and largely trace the stellar content. [Fe II] and $[\mathrm{Fe\,II}]_{\mathrm{Off}}$ narrow bands, when compared together, show specific regions of strong emission at 1.64 μm which largely traces the supernova remnant sources within the galaxy. The Paβ (1.28 μm) and Paβ_{Off} narrow bands, when compared, indicate regions of ionized gas in the galaxy.

2.3 Analysis and Procedure

Figure 2.2 displays the results of our data reduction and mosaicing processes. We created six mosaics of NGC 6946, all of which were used to search for SNRs, as described in the following section. Originally, we collected Paβ imaging (an indicator of ionized gas) with the idea that the ratio of [Fe II] to Paβ would provide guidance in selecting candidate SNRs. The [Fe II]$_{\rm Off}$ and Pa$\beta_{\rm Off}$ filters provide a clean way to measure the continuum for the [Fe II] and Paβ filters because they are adjacent to these 1.64 μm and 1.28 μm lines (respectively), while being relatively free of any other emission lines. Each of the [Fe II] and Paβ filters must be compared carefully to its corresponding 'Off' filter to reveal sources that have detectable emission line flux.

The broad band H filter covers the narrowband [Fe II] and [Fe II]$_{\rm Off}$ filters and provides a stellar continuum reference frame for astrometric and flux calibration purposes. We also use the H band as an independent check on the continuum for possible SNRcs. The broad band J filter covers the narrowband Paβ and Pa$\beta_{\rm Off}$ filters and also provides an independent check on potential SNRs and useful calibration data. The use of multiple filters helps to ensure that our sample is not contaminated by stellar objects in a field that can often be crowded and noisy, despite the high resolution of the WHIRC camera.

2.3.1 Finding supernova remnant candidates

SNRcs were carefully selected through a visual search of the [Fe II] mosaic, primarily using the [Fe II]$_{\rm Off}$ image as an indication of continuum emission. Candidates were chosen that had significant [Fe II] emission while having none or negligible emission in the [Fe II]$_{\rm Off}$ filter. We also checked broad band filters J and H to ensure that little to no continuum flux could be seen. SNRcs were allowed to have observable Paβ emission, although most every object meeting the above criteria showed negligible emission in the Paβ filter. The area we searched was comprised only of the areas of sky where all six bands overlapped. Due to the large size of the mosaics, it was necessary to create a search grid to ensure no objects were left out. In Figure 2.3, the searched area is displayed and the search grid is shown.

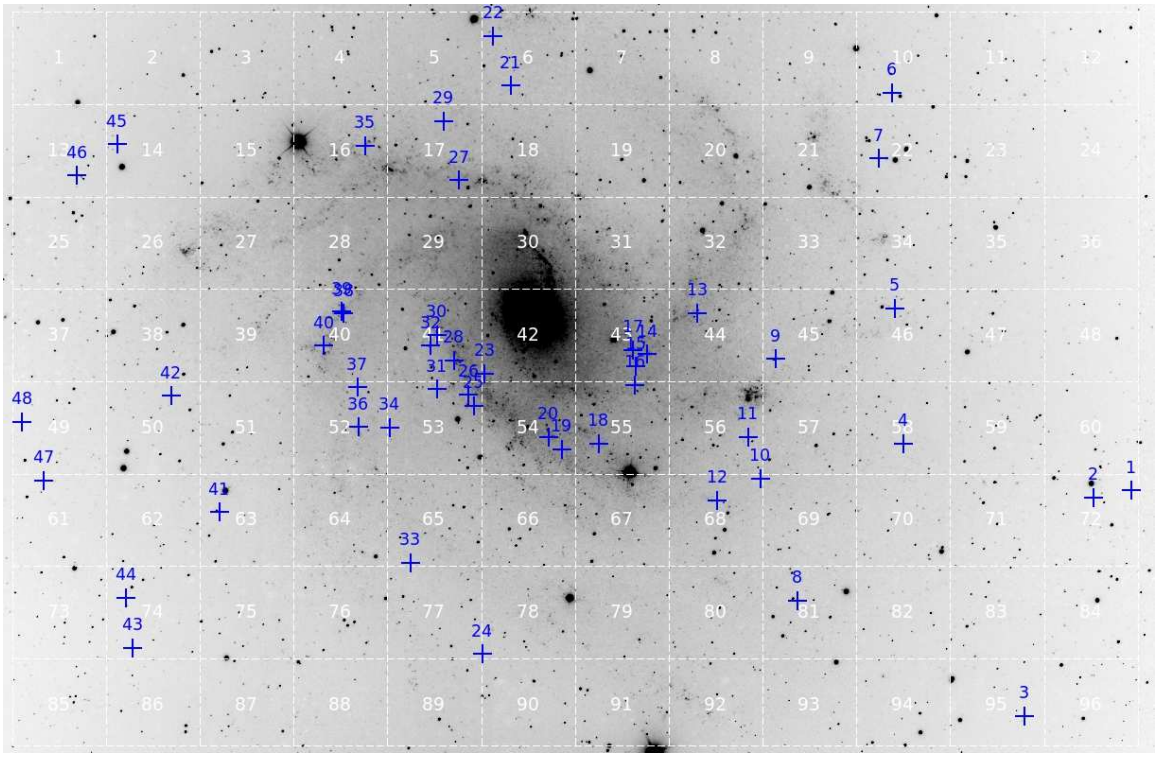

Figure 2.3 A $13.2' \times 8.6'$ selection of our WHIRC H band mosaic illustrates the structure of NGC 6946 while the overlying grey numbered grid designates the area searched in our visual inspection. North is up, east is left. The blue crosses show the distribution of the SNRcs while also indicating their identification numbers.

SNRcs were assigned flags corresponding to visual quality and photometric concerns. Due to the fact that much of [Fe II] mosaic was created from stacking only three images at any one spot, the mosaicing process did not completely remove all artifacts present in the individual images. Some artifacts had an appearance similar to that of the SNRcs and so all of the initial candidates had to undergo a further, in-depth process of examination. The appearance of each SNRc was examined in all of the individual images which had stacked to make the final mosaic. Initial candidates which appeared to be due to a significant source in only one frame while being absent in all other frames were classified as image artifacts and thrown out. Initial candidates that were only seen in two frames and seemed to be consistent with local sky deviations were also removed from the final list in an effort to keep only those objects that were clearly real. At this point, 93 SNRcs remained, of which only 48 would survive the final flux cut as described in Section 2.3.2. Figure 2.4 shows a sample of six of these SNRcs, illustrating their appearance in all filters.

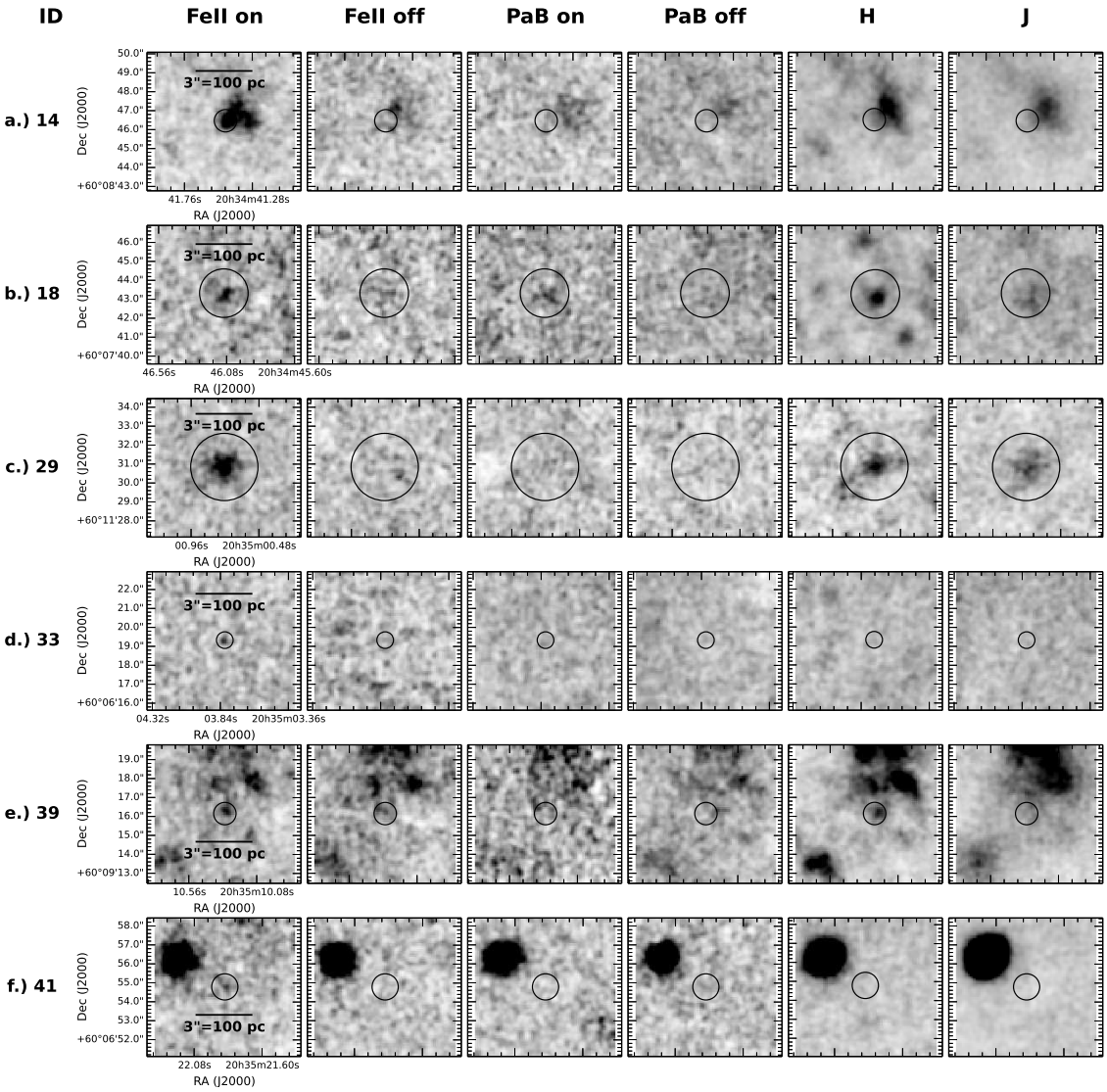

Figure 2.4 Each row shows a SNRc as it appears in each of our six filters. Circles indicate the size of the photometric aperture, coordinates indicated on the first image of every row apply to all images in that row. All images are $7.2'' \times 7.2''$ in dimension, and a scale bar indicating the physical scale is provided in the first image of each row, but is the same for all images in the entire figure. As per our criteria, objects should appear in the [Fe II] images (first column) while being largely absent in the $[\mathrm{Fe\,II}]_{\mathrm{Off}}$ images (second column). There should be negligible emission seen in the Paβ, Paβ_{Off} and J images, however some emission in the H image is expected since the spectral range of the H filter encompasses that of the [Fe II] filter.

In Figure 2.4, the six rows display six different candidates, where each column displays their appearance in a different filter. To qualitatively compare the relative flux levels in

the other bands, all mosaics were set to a linear greyscale display where the minimum and maximum levels of the white-black balance were adjusted such that the sky level and continuum sources appeared as similar as possible between the different filters. The first column of Figure 2.4 shows the [Fe II] filter where the object appears most prominent. A range of [Fe II] morphologies can be seen from slightly extended objects (c) to pointlike objects (b, d, e and f), and an object (a) that is associated with or projected as adjacent to a larger complex of continuum emission. Considering the seeing conditions for our [Fe II] data, SNRs with diameters less than about 40 pc should appear as point sources. SNRs in NGC 6946 and other nearby galaxies have been observed to have diameters ranging from about 10 parsecs to upwards of 200 pc, with a distribution such that it is uncommon to find diameters over 100 pc and in fact, the median reported diameter is just under 40 pc (Matonick & Fesen 1997; Morel et al. 2002; Long et al. 2010). Complexes of SNRs may also exist, which can account for the larger, more extended objects, but we would expect the majority of candidates to appear near point-like in our data, which is indeed the case.

All candidates were chosen such that they appear largely or completely absent in the $[\mathrm{Fe\,II}]_{\mathrm{Off}}$ filter (column 2 of Figure 2.4). Nearly all candidates that met all of the criteria for our final candidate list as described in the following section are also essentially undetectable in the Paβ and Paβ_{Off} filters (columns 3 and 4). However, the SNRcs are identifiable in the H band, as shown in column 5. This is expected since the [Fe II] filter lies completely within the spectral range of the H band, meaning that some emission should be visible in the H band which comes solely from the [Fe II] 1.64 μm line. A visual assessment was made as to the relative brightness in the H band as compared to other continuum sources, and a potential source was retained as a SNRc if it seemed to be less prominently identifiable than its [Fe II] counterpart. In the last column, the J band is displayed and while some objects (b and c) have a small amount of identifiable emission, others do not. Some slight J band emission is also not unexpected, as other [Fe II] lines, most notably the $\lambda = 1.257$ μm line is located in the J band and has been detected in spectra of SNRs (Rosenberg et al. 2012; Kokusho et al. 2013). Considering the range of J and H band emission for objects in Figure 2.4, we would like to underscore the usefulness of using a dedicated $[\mathrm{Fe\,II}]_{\mathrm{Off}}$ filter to assess the local continuum.

Of further note is the fact that objects 14 and 29 (a and c) in Figure 2.4 have counterparts at radio, optical and/or x-ray wavelengths, and both of these objects were previously

identified as SNR candidates in radio and/or optical studies. These two objects along with four more will be discussed further in Section 2.4.2 of this thesis, which will show that six of our 48 candidates have counterparts. SNRcs 14 and 29 have been displayed in Figure 2.4 to help demonstrate the range of morphologies seen in the candidates, although the majority of SNRcs have fainter, point-like morphologies like SNRcs 18, 33, 39 and 41, as can be seen in Figures 2.7 - 2.9.

2.3.2 Flux measurements

We measured the SNRc fluxes in the [Fe II], $[\text{Fe II}]_{\text{Off}}$ and H bands using aperture photometry and used the flux information to further constrain our SNRc list. To begin, we calibrated these three mosaics using stars from the 2MASS catalog. We visually inspected all stars listed in the 2MASS catalog within our search region and specifically removed stars that were flagged in the 2MASS catalog or appeared saturated, extremely bright or confused with a nearby bright object in our images, leaving us with 315 stars. The [Fe II] and $[\text{Fe II}]_{\text{Off}}$ filters lay within the H filter of 2MASS, and WHIRC's H filter overlaps the spectral range of 2MASS's H filter. We can calculate the expected flux through these WHIRC filters for our calibration stars using the H-band magnitudes as given in the 2MASS catalog ($m_{H,2MASS}$), and the appropriate filter width from Table 2.1 ($\Delta\lambda$). The H-band flux for 0 magnitude stars in the 2MASS survey is $f_{H=0}$=1.133 $\times 10^{-13} \pm 2.212\ 10^{-15}$ W cm^{-2} μm^{-1} (Carpenter 2001). For the [Fe II] filter, the expected flux is:

$$F_{measured}([\text{Fe II}]) = f_{H=0}\Delta\lambda_{[\text{Fe II}]}\ 10^{-0.4\ m_{H,2MASS}} \tag{2.1}$$

However, to enable a comparison to other reported fluxes, we want to calculate the flux corrected for extinction. Although there is evidence of patchy internal extinction within NGC 6946 (Belley & Roy 1992; Hyman et al. 2000; Cedrés et al. 2012), for the purposes of this paper we only correct for foreground extinction. This extinction adds a modestly significant correction due to the galactic latitude of NGC 6946, as seen in the values reported in Table 1.2. The extinction corrected fluxes can be found by modifying Equation 2.1 so that:

$$F([\text{Fe II}]) = f_{H=0}\Delta\lambda_{[\text{Fe II}]}\ 10^{-0.4(m_{H,2MASS}-A_H)} \tag{2.2}$$

$$= (1.858 \times 10^{-8}) \times 10^{-0.4(m_{H,2MASS}-0.154)} \tag{2.3}$$

These fluxes in erg s^{-1} cm^{-2} were then plotted against the counts measured from applying aperture photometry with $r_{\rm aper}$=2.5″, $r_{\rm skyann}$=3″ and $d_{\rm ann}$=1″ to all of the 315 calibration stars in each of the [Fe II], $[\mathrm{Fe\,II}]_{\rm Off}$ and H band WHIRC mosaics. Figure 2.5 shows this plot for the [Fe II] band where the linear regression yielded the following flux calibration:

$$F([\mathrm{Fe\ II}]) = 1.20 \times 10^{-18}\ S_{[\mathrm{Fe\ II}]}, \tag{2.4}$$

while similarly, we found:

$$F([\mathrm{Fe\ II}]_{\rm Off}) = 1.05 \times 10^{-18}\ S_{[\mathrm{Fe\ II}]\rm Off} \quad \text{and} \tag{2.5}$$

$$F(H) = 1.50 \times 10^{-18}\ S_{H}. \tag{2.6}$$

S in Equations 2.4 through 2.6 represents the total number of counts measured from the mosaic image within the photometric aperture, subtracting the sky contribution, and F is the extinction corrected flux of the object in erg s^{-1} cm^{-2}. A list of our SNRcs is given in Table 2.3 and reports the corrected fluxes in these three bands.

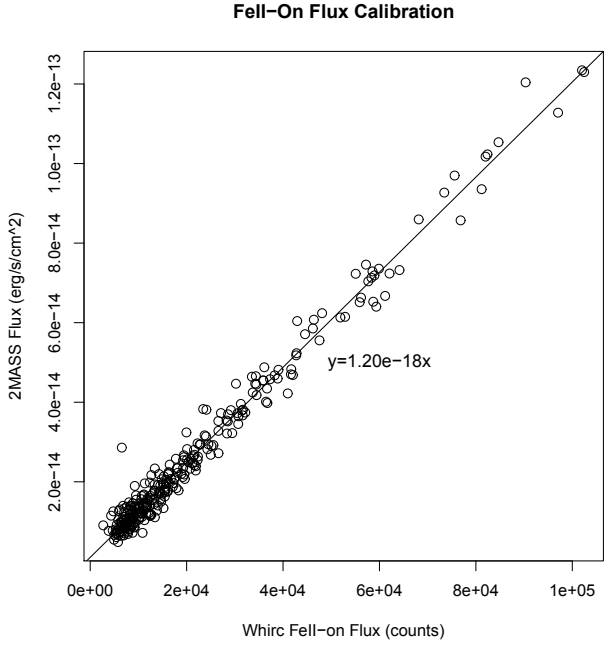

Figure 2.5 Above, a linear fit to the realtion of counts measured using aperture photometry on our WHIRC [Fe II] mosaic versus [Fe II] fluxes as derived from the 2MASS H-band magnitudes, for 215 stars located in the searched area of the mosaic field.

Table 2.3. Fluxes for SNR Candidates.

SNRc ID	RA (J2000) (deg.)	DEC (J2000) (deg.)	$F([\mathrm{Fe\,II}])$ ($10^{-16}\frac{erg}{s\ cm^2}$)	[Fe II] S/N	$F([\mathrm{Fe\,II}]_{\mathrm{Off}})$ ($10^{-16}\frac{erg}{s\ cm^2}$)	$F(H)$ ($10^{-16}\frac{erg}{s\ cm^2}$)	Aper (pixels)	InSkyAnn (pixels)	AnnD (pixels)	Phot[a] (flag)
1	308.48267	+60.1193123	2.17 ± .02	7.1	-1.59 ± .03	1.83 ± .18	5	7	7	0
2	308.49762	+60.1179543	3.51 ± .04	9.2	1.03 ± .04	5.58 ± .15	7	8	5	0
3	308.52478	+60.0751953	5.68 ± .06	7.3	1.15 ± .04	15.30 ± .15	9	11	6	0
4	308.57217	+60.1286392	4.30 ± .04	8.6	2.08 ± .05	8.70 ± .11	8	9	6	0
5	308.57523	+60.1551170	3.11 ± .03	6.7	0.58 ± .06	20.99 ± .13	6	8	7	0
6	308.57643	+60.1973360	2.69 ± .03	6.4	1.19 ± .04	10.05 ± .13	6	8	7	1
7	308.58175	+60.1844380	1.75 ± .02	6.3	0.21 ± .04	-0.42 ± .13	4	5	7	0
8	308.61377	+60.0979347	1.96 ± .02	6.9	-0.51 ± .04	5.76 ± .21	4	6	8	0
9	308.62234	+60.1452675	9.12 ± .09	11.1	-0.16 ± .06	74.94 ± .20	8	36	2	1
10**	308.62851	+60.1218643	13.88 ± .14	11.2	9.15 ± .04	89.67 ± .19	14	16	4	0
11	308.63330	+60.1299706	4.55 ± .05	6.7	-1.59 ± .06	0.48 ± .19	7	9	6	1
12	308.64529	+60.1175385	2.66 ± .03	7.5	0.55 ± .05	2.35 ± .17	4	6	8	0
13	308.65308	+60.1542206	2.37 ± .02	6.4	1.15 ± .06	10.43 ± .17	4	6	8	1
14**	308.67279	+60.1462402	14.92 ± .15	30.2	5.15 ± .05	33.55 ± .25	6	16	2	1
15**	308.67725	+60.1437569	22.92 ± .23	15.5	12.59 ± .05	101.08 ± .23	15	16	4	0
16*	308.67773	+60.1401901	5.06 ± .05	9.9	2.39 ± .06	23.11 ± .31	6	7	4	1
17	308.67841	+60.1470680	3.04 ± .03	6.8	-0.74 ± .06	-4.56 ± .27	5	7	7	0
18	308.69208	+60.1287003	16.35 ± .16	13.8	3.43 ± .05	158.95 ± .25	13	14	3	0
19	308.70657	+60.1276321	3.29 ± .03	6.8	-0.14 ± .06	19.61 ± .23	5	7	7	1

Table 2.3 (cont'd)

SNRc ID	RA (J2000) (deg.)	DEC (J2000) (deg.)	$F([\mathrm{Fe\,II}])$ ($10^{-16}\frac{erg}{s\ cm^2}$)	[Fe II] S/N	$F([\mathrm{Fe\,II}]_{\mathrm{Off}})$ ($10^{-16}\frac{erg}{s\ cm^2}$)	$F(H)$ ($10^{-16}\frac{erg}{s\ cm^2}$)	Aper (pixels)	InSkyAnn (pixels)	AnnD (pixels)	Phot[a] (flag)
20	308.71173	+60.1299858	7.40 ± .07	8.5	0.42 ± .06	3.80 ± .29	8	10	5	1
21	308.72655	+60.1988090	3.29 ± .03	7.6	1.11 ± .05	6.87 ± .23	5	6	7	0
22	308.73356	+60.2085220	2.15 ± .02	6.1	0.96 ± .05	-0.60 ± .16	4	6	8	0
23	308.73688	+60.1423874	8.03 ± .08	8.7	-0.34 ± .06	21.38 ± .20	8	10	6	1
24	308.73770	+60.0875282	5.85 ± .06	6.2	0.30 ± .06	3.76 ± .12	7	9	6	0
25	308.74103	+60.1361008	7.23 ± .07	10.1	-0.68 ± .05	3.50 ± .19	7	9	6	1
26	308.74304	+60.1383057	5.77 ± .06	8.0	0.94 ± .06	11.09 ± .22	7	9	6	0
27	308.74688	+60.1802710	2.30 ± .02	6.6	0.86 ± .04	12.75 ± .21	4	5	7	0
28**	308.74896	+60.1449738	10.36 ± .10	18.9	5.75 ± .05	46.54 ± .33	5	6	6	1
29**	308.75303	+60.1919010	46.18 ± .46	28.2	15.14 ± .04	121.41 ± .17	18	20	3	0
30	308.75552	+60.1499600	6.19 ± .06	10.7	1.30 ± .05	46.87 ± .27	6	7	5	0
31	308.75562	+60.1393929	2.62 ± .03	6.1	-0.38 ± .05	12.67 ± .16	5	7	7	0
32	308.75797	+60.1478653	5.15 ± .05	7.0	0.26 ± .04	18.40 ± .19	7	9	6	0
33	308.76587	+60.1053696	2.40 ± .02	6.7	0.55 ± .05	-0.77 ± .15	3	5	8	0
34	308.77426	+60.1318092	3.12 ± .03	6.5	0.96 ± .04	23.84 ± .15	7	9	6	1
35	308.78394	+60.1870340	16.36 ± .16	19.9	2.74 ± .06	149.22 ± .33	11	13	5	1
36	308.78644	+60.1319656	2.45 ± .02	6.0	-0.30 ± .05	6.21 ± .17	4	6	6	0
37	308.78677	+60.1397591	3.21 ± .03	6.3	-0.32 ± .05	6.30 ± .16	5	6	7	1
38*	308.79218	+60.1541748	4.37 ± .04	7.6	3.54 ± .05	17.18 ± .31	6	7	5	1

Table 2.3 (cont'd)

SNRc ID	RA (J2000) (deg.)	DEC (J2000) (deg.)	$F([\mathrm{Fe\,II}])$ ($10^{-16}\frac{erg}{s\ cm^2}$)	[Fe II] S/N	$F([\mathrm{Fe\,II}]_{\mathrm{Off}})$ ($10^{-16}\frac{erg}{s\ cm^2}$)	$F(H)$ ($10^{-16}\frac{erg}{s\ cm^2}$)	Aper (pixels)	InSkyAnn (pixels)	AnnD (pixels)	Phot[a] (flag)
39**	308.79294	+60.1544860	6.80 ± .07	10.2	4.25 ± .05	7.56 ± .38	6	7	3	1
40*	308.80002	+60.1478691	6.05 ± .06	8.0	3.10 ± .05	47.06 ± .25	8	10	5	0
41	308.84110	+60.1152200	4.16 ± .04	7.1	-0.68 ± .04	5.18 ± .15	7	9	6	1
42	308.86008	+60.1379738	2.01 ± .02	7.5	0.43 ± .03	1.66 ± .13	3	5	7	0
43	308.87500	+60.0885811	2.81 ± .03	6.5	-0.40 ± .06	-1.76 ± .11	5	7	7	0
44	308.87766	+60.0983963	5.60 ± .06	6.7	-1.76 ± .06	9.96 ± .15	11	13	5	1
45	308.88158	+60.1872070	2.34 ± .02	7.9	-0.49 ± .04	6.48 ± .14	6	7	7	1
46	308.89725	+60.1811020	1.69 ± .02	7.4	-1.34 ± .03	0.47 ± .15	4	5	5	1
47*	308.91010	+60.1213608	4.81 ± .05	8.3	1.86 ± .04	9.92 ± .15	7	9	6	0
48	308.91873	+60.1327972	1.93 ± .02	6.5	0.53 ± .05	-1.26 ± .16	3	5	7	0

Note. — All reported flux errors are σ_{sky}/pixel extraction errors only. Negative fluxes are interpreted as being zero, thus the range of magnitudes of the negative fluxes reported in the $[\mathrm{Fe\,II}]_{\mathrm{Off}}$ and H bands gives a better indication of the overall flux error in those bands, which would include calibration errors and errors in 2MASS measurements.

[a]The photometric flag indicates a 1 if a nearby object may have affected the flux in the SNRc's photometric aperture or sky annulus.

*These objects have $[\mathrm{Fe\,II}]_{\mathrm{Off}}$ S/N values greater than 3.

**These objects have both $[\mathrm{Fe\,II}]_{\mathrm{Off}}$ S/N values greater than 3 and $[\mathrm{Fe\,II}]_{\mathrm{Off}}/[\mathrm{Fe\,II}]$ flux ratios greater than 0.5.

Table 2.3 also lists the photometric aperture and sky annulus chosen for each candidate. The various apertures shown were chosen through a combination of curve-of-growth inspection and considerations of local seeing conditions in the H, [Fe II], and [Fe II]$_{\rm Off}$ mosaics. Due to the crowded nature in many parts of the field, some of the sky annuli had to be adjusted to avoid contamination by nearby objects. Images of the SNRcs in Figures 2.4 and 2.7 through 2.9 show the chosen photometric aperture as a black circle. For reference, Table 2.3 also provides a photometric flag to indicate if a bright object was observed to be near the candidate and so may have contributed flux to pixels within the aperture and/or sky annulus.

When we measured the counts for each SNRc, S, using the NOAO `PHOT` package in IRAF, we also noted an estimate of the local statistical noise, $\sigma_{\rm sky}$, the standard deviation of counts for the pixels within the sky annulus. Using these values, a statistical signal to noise value (S/N) was calculated as:

$$S/N = \frac{S}{\sigma_{\rm sky}\sqrt{\pi r_{aper}^2}}, \tag{2.7}$$

where r_{aper} is the radius of the object's photometric aperture in pixels. A careful consideration of the visual appearance of each SNRc showed this S/N parameter to be a useful tool in selecting objects of high confidence. We chose to define a S/N level of 6 in the [Fe II] band to be a defining criteria in our selection process based on the visual appearance of the candidates. Objects with with a [Fe II] S/N less than 6 were not included in our final list.

The [Fe II]$_{\rm Off}$ and H band fluxes were also checked to ensure our original visual inspection was successful, and so additional criteria were considered before our candidate list was finalized. Primarily, we set limits such that candidates should have a [Fe II]$_{\rm Off}$ band flux which is no more than half the [Fe II] flux, and H band flux no more than 10 times the [Fe II] flux. We assigned these numerical values to properly ensure our candidate list was free of continuum sources. However, six objects (marked with double asterisks in Tables 2.3 and 2.4) were allowed to exceed the [Fe II]$_{\rm Off}$/[Fe II] flux ratio limit, as determined by considerations of the flux and corresponding S/N values for all three bands as a whole, in addition to visual appearance. After employing these final flux and S/N cuts, but allowing for a few exceptions, we were left with 48 objects we can confidently name as supernova remnant candidates.

To elucidate the allowance of exceptions, we will discuss the most dubious source in our final list, SNRc 38, which has an abberantly high [Fe II]$_{\rm Off}$/[Fe II] flux ratio of 0.8. This object would generally have been excluded from the final candidate list, but was not cut when all information was considered as a whole. It had a strong visual appearance in the [Fe II] band, an unimpressive appearance in the [Fe II]$_{\rm Off}$ band, relatively low S/N levels in all bands, and most interestingly, a H/[Fe II] flux ratio of less than 4. If this object was a continuum object, and assuming a flat spectrum across the H band, the ratio of the H and [Fe II] bandwiths imply that the H/[Fe II] flux ratio should be 18.35. Thus SNRc 38 seems to be emitting its H band flux mostly in the [Fe II] and [Fe II]$_{\rm Off}$ band regions, which was reason to suspect this as a possible [Fe II] emission object. The six exceptions highlight the issue of non-diffuse continuum emission being present in the area of the SNRcs, which requires us to do a continuum subtraction to find the true [Fe II] emission line fluxes.

As the flux measurements in Table 2.3 illustrate, there is some considerable noise in our images. This noise varies across the mosaics in such a way that it was not found feasible to produce a globally continuum-subtracted image. Thus, to estimate continuum-subtracted fluxes, we investigated the range of [Fe II]$_{\rm Off}$ fluxes and their associated S/N values. We determined that objects would need to be continuum-subtracted only if their [Fe II]$_{\rm Off}$ S/N was more than 3. S/N levels below 3 in the [Fe II]$_{\rm Off}$ band must be considered non-detections due to the scatter of measured [Fe II]$_{\rm Off}$ flux values, especially those values below zero. This method will be further clarified in Chapter 3 (Section 3.4) of this thesis.

In all, 10 candidates were found to have significant 'continuum' flux, these candidates include the six exceptions with high [Fe II]$_{\rm Off}$/[Fe II] flux ratios. These 10 candidates are designated in Table 2.4 by an asterisk or double asterisk, depending on their [Fe II]$_{\rm Off}$/[Fe II] flux ratio, and these 10 candidates had luminosities calculated from F([Fe II]) $-$ F([Fe II]$_{\rm Off}$) values, to ensure all reported luminosities are continuum-subtracted. All other objects in Table 2.4 have luminosities calculated from just F([Fe II]), since we consider their [Fe II]$_{\rm Off}$ fluxes to be essentially zero.

Table 2.4. Luminosities for SNR Candidates.

SNRc ID	$L_{[Fe\,II]}$ $(10^{33}\frac{erg}{s})$	Alternate Names	SNR ID	$L_{[Fe\,II]}$ $(10^{33}\frac{erg}{s})$	Alternate Names
1	903 ± 26		25	3013 ± 85	MF:14
2	1463 ± 41		26	2402 ± 68	
3	2365 ± 67		27	958 ± 27	
4	1791 ± 51		28**	1805 ± 220	
5	1296 ± 37		29**	12557 ± 997	LDG:85, MF:16, HSHP:58
6	1118 ± 32		30	2579 ± 73	
7	730 ± 21		31	1092 ± 31	
8	818 ± 23		32	2144 ± 61	
9	3797 ± 107		33	998 ± 28	
10**	1793 ± 311		34	1299 ± 37	
11	1895 ± 54		35	6815 ± 193	LDG:101, HSHP:65
12	1108 ± 31		36	1020 ± 29	
13	985 ± 28		37	1338 ± 38	
14**	3963 ± 332	LDG:26, HSHP:21	38*	273 ± 90	
15**	4050 ± 508		39**	980 ± 137	
16*	1065 ± 109		40*	1170 ± 118	
17	1267 ± 36		41	1732 ± 49	
1 8	6811 ± 192		42	838 ± 24	
19	1371 ± 39		43	1172 ± 33	
20	3082 ± 87	LDG:47, HSHP:42	44	2332 ± 66	
21	1370 ± 39		45	976 ± 28	
22	896 ± 25		46	704 ± 20	
23	3343 ± 94	HSHP:50	47*	1194 ± 92	
24	2435 ± 69		48	802 ± 23	

Note. — Luminosity was calculated using a distance of 5.9 Mpc and [Fe II] flux values in Table 2.3, except objects marked with * or **, where luminosities are based off [Fe II]-$[Fe\,II]_{Off}$ fluxes due to siginificant continuum detections at those locations. Luminosity errors reflect σ_{sky}/pixel extraction error as well as a nominal 2% flux calibration error. LDG refers to radio sources from Lacey et al. (1997), MF refers to optical SNRcs from Matonick & Fesen (1997) and HSHP refers to x-ray sources from Holt et al. (2003).

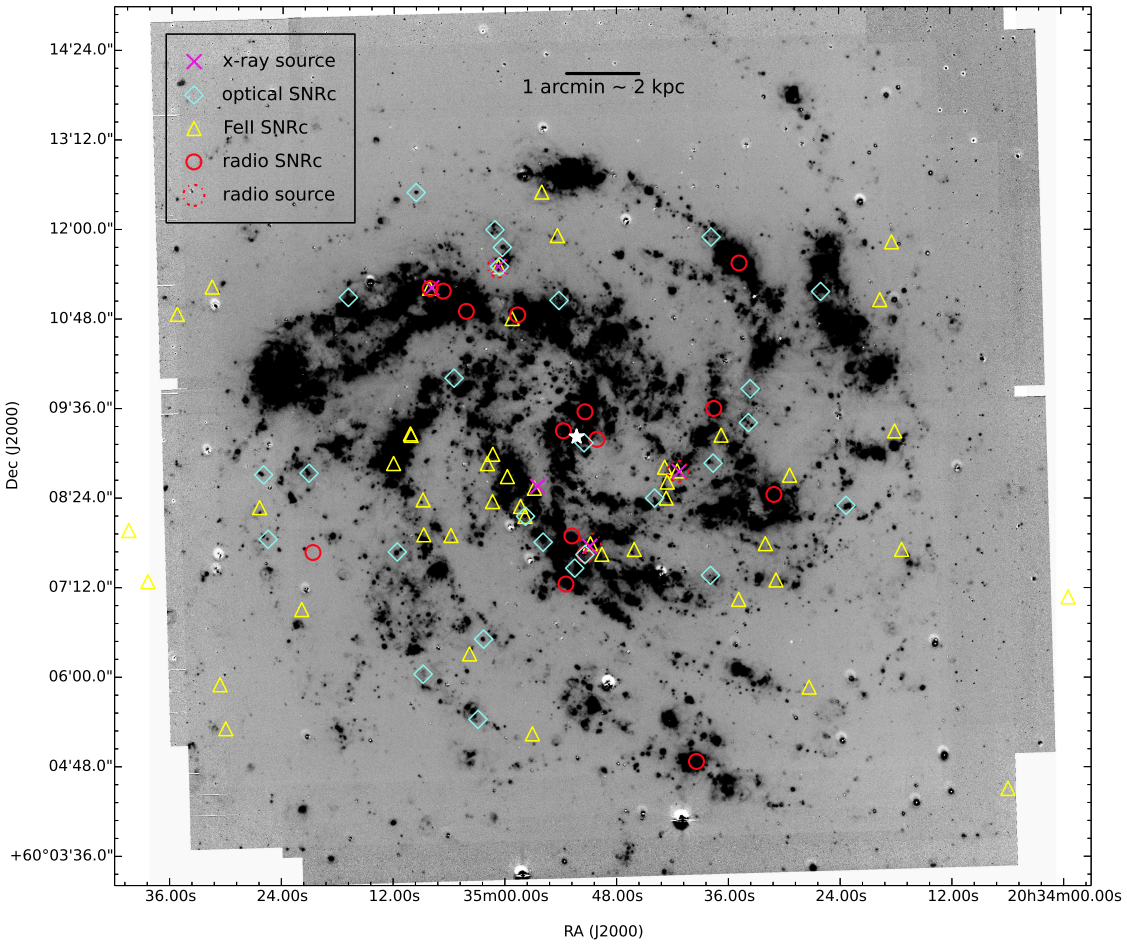

Figure 2.6 Above, an Hα image obtained by F. Winkler and K. Long at WIYN is overlayed with markers that show the distribution of our [Fe II] identified SNRcs (triangles) as well as optical and radio identified SNRcs, marked by diamonds and circles and taken from Matonick & Fesen (1997) and Hyman et al. (2000), respectively. Additionally, if any x-ray sources from Holt et al. (2003) or radio sources from Lacey et al. (1997) were identified as counterparts to our [Fe II] selected SNRcs, they are also indicated above, with dashed circles and x's, as indicated in the legend. As can be seen, distributions of SNRcs from all wavelengths are highly concentrated on the dense, spiral arm regions of the galaxy, while avoiding the interarm regions. The center of the galaxy is marked with a star, and note that the area within an arcminute of the galaxy center was largely obscured in our search due to a high level of continuum emission.

2.4 Discussion

Figure 2.3 shows the spatial distribution of the final 48 SNRcs. As can be seen, the spatial distribution of the SNRcs is highly correlated with the denser, dusty star-rich environment of the spiral arms of NGC 6946. Indeed, plotted on an Hα image of NGC 6946 in Figure 2.6, only five of the furthest SNRcs cannot clearly be seen to be lying within a spiral arm, a fact due to the limited size of the Hα image we have displayed, but it is not hard to extrapolate that these five objects likely lie on extended, fainter regions of the dense spiral arms. Certainly, no SNRc within $\sim$7 kpc of the core of NGC 6946 is located in an interarm region. Note that there is an apparent region of avoidance for our SNRcs located north of the bulge (most apparent in Figure 2.3). This region corresponds to an approximately $1' \times 6'$ region of our [Fe II] mosaic where the general observational conditions led to a reduced image quality and generally made it impossible to identify objects with high confidence.

2.4.1 [Fe II] fluxes of SNRs in various galaxies

Strong [Fe II] emission can be produced when the destruction of dust grains by shocks increases gas phase iron abundances and/or when partially ionized regions are created by shock heating or by power law photionization from UV or x-ray radiation (Mouri et al. 2000). Strong 1.64 μm [Fe II] line emission has been observed in galactic SNRs and is generally observed to originate in filamentary-like structures (see Graham et al. 1989; Burton & Spyromilio 1993; Lee et al. 2009, and sources for examples). It is often difficult to calculate an integrated flux for galactic SNRs due to their complex extended nature, not to mention uncertainties involved in distance, and issues of extinction and absorption. However, a number of studies exist which have investigated the total 1.64 μm [Fe II] flux from galactic SNRs and the resulting luminosities have a range of 9×10^{32} to 7×10^{35} erg s^{-1} (Oliva et al. 1989; Keller et al. 1995; Lee et al. 2009). Oliva et al. (1989) also reported 1.64 μm [Fe II] luminosities of SNRs in the Large Magellanic Cloud which ranged from 1×10^{35} to 3×10^{36} erg s^{-1}. In a study of near IR emission in local starbursting galaxies (Labrie & Pritchet 2006), NGC 1569 and NGC 5253 were reported to have [Fe II] 1.64 μm luminosities for SNRcs ranging from 2×10^{35} to 2×10^{36} erg s^{-1}, inclusively. In the local starbursting galaxy M33, an [Fe II] imaging survey of optically selected SNRs by Morel et al. (2002) derived [Fe II] 1.64 μm luminosities on order of 2×10^{36} erg s^{-1}. Yet it has been seen

that [Fe II] luminosities of SNRs in starbursting galaxies can generally be much higher than those measured in our own galaxy or in other, non-starbursting local galaxies. A study of 1.64 μm [Fe II] emission in M82 and NGC 253 reported [Fe II] luminosities of SNRs from 3 $\times$ 10^{36} to 2 $\times$ 10^{38} erg s^{-1} (Alonso-Herrero et al. 2003). These luminosities reported by Alonso-Herrero et al. (2003) were in agreement with prior [Fe II] measurements of SNRs in M82 (Greenhouse et al. 1997) while Forbes & Ward (1993) derived even higher luminosities for SNRs in NGC 253.

Using a distance to NGC 6946 of 5.9 Mpc, the 48 SNRcs identified in our study have 1.64 μm [Fe II] luminosities ranging from 2.7 $\times$ 10^{35} to 1.2 $\times$ 10^{37} erg s^{-1}, as reported in Table 2.4. These luminosities are higher than those reported for galactic SNRs and are are consistent with the luminosities of SNRs in other starbursting galaxies. Unfortunately, the range of luminosities of our candidates is not comparable to the studies listed above in a clearly quantitative sense, owing at least in part to a difference of techniques employed. When comparing the [Fe II] luminosity ranges reported above, there are a number of factors that should be considered.

The studies by Labrie & Pritchet (2006) and Alonso-Herrero et al. (2003) are most similar to ours, however neither of these studies obtained $[\mathrm{Fe\,II}]_{\mathrm{Off}}$ band imaging, and instead used other methods by which to estimate the [Fe II] continuum contamination. Labrie & Pritchet (2006) used H band observations to estimate the continuum for the [Fe II] filter. In Alonso-Herrero et al. (2003), the continuum level was estimated from a linear regression of the flux as it appeared in three different filters. Our study hinged on the use of a carefully constructed, dedicated continuum filter adjacent to the [Fe II] filter, in order to ensure that no contamination by various [Fe II], H_2 or other emission lines would affect our estimate of the continuum level. Another difference of techniques, Alonso-Herrero et al. (2003) used an automated method (`DAOFIND`) to detect sources while we identified sources through a visual inspection method. Labrie & Pritchet (2006) also visually searched for sources, but removed non-compact sources from their SNRc list, whereas we allow some slightly extended sources in our SNRc list.

The study by Morel et al. (2002) chose 42 objects from a catalog of 98 optically selected targets in M33, and firmly detected just 7 of these objects, while our study was a blind search across the entire galaxy, without using a priori information about the location of previously detected objects. On later comparison, we independently detected 2 of a catalog

of 27 optically identified SNRcs within the galaxy (as will be discussed in Section 2.4.2), but detecting 46 objects that were not optically identified. However in comparing the numbers of SNRcs found in the various studies referenced above, more factors need to be accounted for, including the fact that dwarf galaxies like those in the study by Labrie & Pritchet (2006) are much smaller galaxies and likely have lower SFRs and thus a smaller number of SNRs. Also of note is that Alonso-Herrero et al. (2003) surveyed a much smaller percent of their target galaxies than the other studies mentioned here.

Overall, what we can say is that the number of SNRcs and the general luminosities we found in NGC 6946 are consistent with similar studies in other starbursting galaxies. This adds to our confidence that we have been successful in detecting SNRs. And considering the observed range of SNR [Fe II] luminosities that exist as a whole, with galactic SNRs showing us the fainter values which might be beyond our current sensitivity limits, we have likely observed only the brightest population of SNRs in NGC 6946. The reason why SNRs in starbursting galaxies have ranges of [Fe II] luminosities that reach much higher values than galactic SNRs is not well understood, but may result from a number of environmental factors including metallicity or density of the local ISM as well as the age or type of the SNR.

2.4.2 NGC 6946 SNRcs from studies using different wavelengths

There have been three previous searches for SNRs in NGC 6946. An optical search by Matonick & Fesen (1997), here after referred to as MF, used a [S II]/Hα criteria to identify 27 SNRcs. In the radio, Hyman et al. (2000) and Lacey & Duric (2001) both analyzed the observations and catalog of 118 radio sources reported in Lacey et al. (1997), hereafter referred to as LDG. Out of the 118 LDG sources, Hyman et al. (2000) lists 15 as SNR candidates (or nonthermal sources) and 43 as candidate H II regions (with a possible contamination by nonthermal plerionic SNRs). These classifications were made based on their spectral index, α, where $S = \nu^{+\alpha}$. Lacey & Duric (2001) used a similar criterion for choosing SNR candidates, but listed 35 SNRcs which actually include all SNRcs from Hyman et al. (2000) except one. For simplicity, the 36 total candidates from both studies are considered here as radio SNRcs, and referred to by their LDG catalog number. These

optical and radio SNRcs are plotted in Figure 2.6 as diamonds and circles, respectively, along with our [Fe II] identified SNRcs which appear as triangles.

As previously stated, the distribution of our SNRcs largely follows the spiral arm structure of NGC 6946. Similarly, a qualitative assessment of Figure 2.6 shows that optical and radio SNRcs are also spread throughout the spiral arms, avoiding the inner-most interarm regions. As discussed more thoroughly in Lacey & Duric (2001), though, the radio SNRcs seem to be more tightly correlated with the densest spiral arm regions, while the optical SNRcs are spread more to the edges of the spiral arms. Our [Fe II] SNRcs are located in all parts of the spiral arms, including the faint, extended arm regions. While both optical and radio selected SNRcs exist in these extended regions as well, it appears that our [Fe II] identified SNRcs are found further out than any other previously reported population. This is likely due to the difference in surveyed area between the studies. MF imaged an $8.7' \times 8.7'$ area about the center of the galaxy which, referring to Figure 2.3, would leave off the first column and a half of our search grid, as well as the last two and a half columns. LDG's largest surveyed area was $11' \times 9'$, which misses the first half column and last column and a half of our search grid. Due to these differences, five of our furthest candidates were not imaged in the radio and nine were not imaged in the optical.

In addition to the published SNR candidates, we examined the distribution of all 118 LDG radio sources in NGC 6946 as well as 72 Chandra x-ray sources published by Holt et al. (2003), hereafter HSHP (this x-ray study surveyed an $8' \times 8'$ area about the center of the galaxy). While the general distribution of these radio and x-ray sources is a bit scattered, it is still true that a very small percent of these sources are located in the sparsest interarm regions (as defined by an Hα map), as is true for the SNRcs. But while the inner-core region of NGC 6946 contains a number of cataloged point sources at other wavelengths, especially in the radio regime, we did not detect SNRcs in this central region (our closest SNRc being 1.8 kpc from the galaxy's center). The main factor that contributed to this fact is the extreme difficulty in applying our search method in the innermost region of the galaxy, within a $1'$ (2 kpc) radius of the center of the galaxy, where the steep gradients of the light distribution made it difficult to clearly image the area, and the high values of the background due to stellar continuum contributions decreased the signal to noise, making it harder to identify objects.

We searched for coincident sources between our candidates and radio, optical and/or

X-ray sources, and found tha 6 of our 48 SNRcs had at least one counterpart. Coincident sources are specified in the *alternate names* column in Table 2.4. Optical and radio counterparts were $\leq 1''$ from our SNRcs, while x-ray counterparts were between $0.15''$ and $3''$. As an overview, we identified 3 of the 36 radio SNRcs, 2 of the 27 MF SNRcs as well as one more radio source and 5 x-ray sources as coincident with our [Fe II] SNRcs. At this point, it is important to note that our [Fe II] SNRc list was strongly affected by our preference to confidently report sources, instead of ensuring completeness. In this regard, it is interesting to note that 3 of the 45 potential SNRcs we discarded in our final S/N cut have associations with previously published optical or radio SNRcs. This may suggest that with deeper imaging, we would have detected more of the previously published SNRcs.

Below, we give details of the six SNRcs which have counterparts:

SNRc 14: One of the brightest [Fe II] sources in our list of SNRcs, this object is located about 2.8 kpc south-west of the galaxy center in an area dense with SNRcs. This candidate was classified as a radio SNRc (LDG 26) and has a corresponding x-ray counterpart (HSHP 21).

SNRc 20: An intermediately bright [Fe II] source, this object is located in the southern spiral arm about 2.9 kpc south of the galaxy center. This candidate was classified as a radio source (LDG 47) and has a corresponding x-ray counterpart (HSHP 42).

SNRc 23: An intermediately bright [Fe II] source, this object is located about 1.8 kpc south-east of the galaxy center, closer in on the same spiral arm as SNRc 20 and in another area dense with SNRcs. This candidate has an x-ray counterpart (HSHP 50).

SNRc 25: An intermediately bright [Fe II] source, this object is located about 2.5 kpc south-east of the galaxy center, near SNRc 23. This candidate has a counterpart classified as an optical SNRc (MF 14).

SNRc 29: The brightest [Fe II] source in our SNRc list, by far, this object is located in the north-eastern spiral arm about 5 kpc north-east of the galaxy center. This candidate was classified as a radio SNRc (LDG 85), an optical SNRc (MF 16) and has a corresponding x-ray counterpart (HSHP 58).

SNRc 35: Our third brightest [Fe II] source in out list of SNRcs, this object is located in the same north-eastern spiral arm as SNRc 29, a distance of 5.6 kpc north-east of the galaxy center. This candidate was classified as a radio SNRc (LDG 101) and has a corresponding x-ray counterpart (HSHP 65).

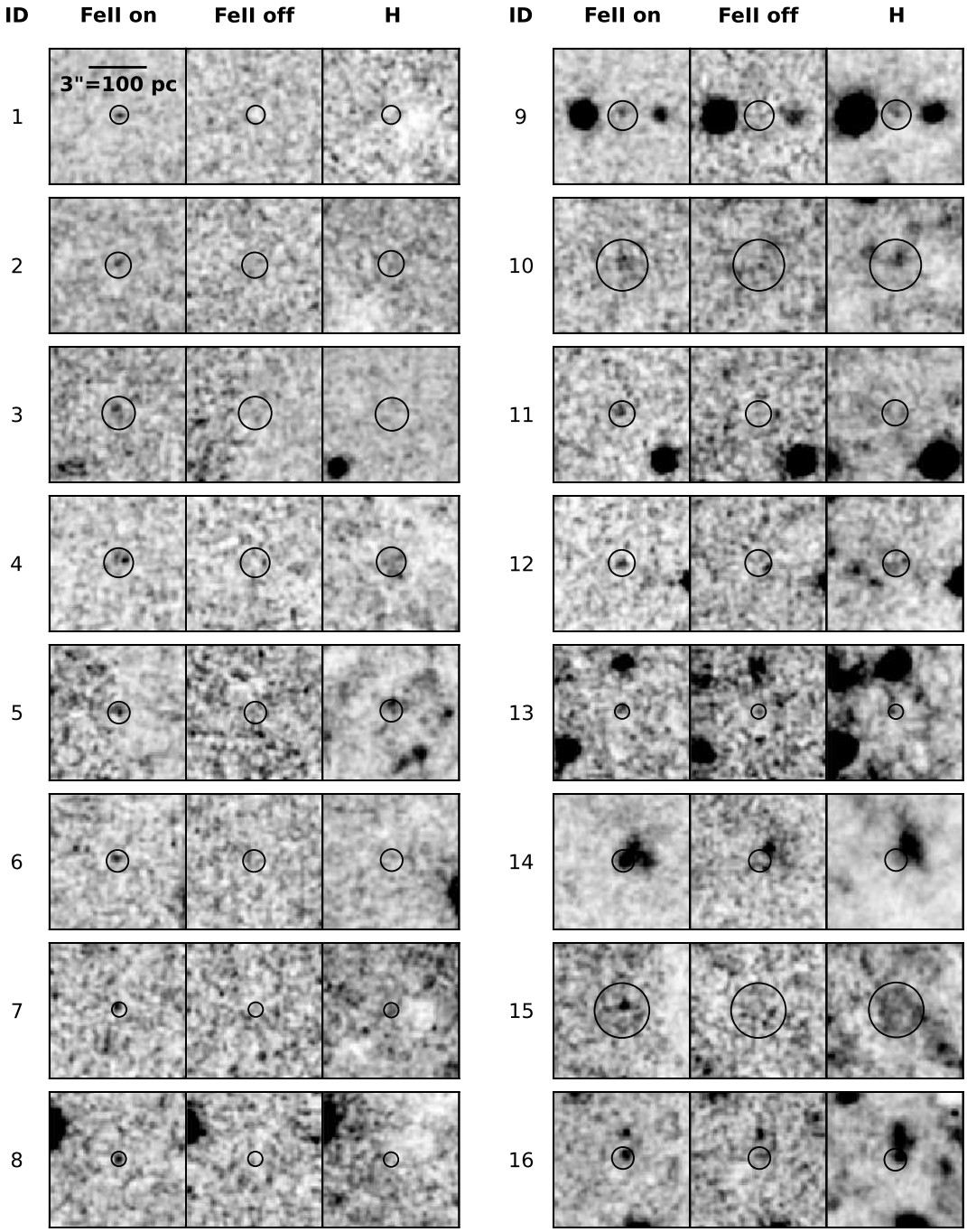

Figure 2.7 Images show how our SNRcs appear in the [Fe II], $[\mathrm{Fe\,II}]_{\mathrm{Off}}$ and H bands. Circles indicate the photometric aperture used to measure the flux for each SNRc, and are the same size for each candidate in every band. Every thumbnail is oriented such that north is up and east is left, all are $7.2'' \times 7.2''$ and a scalebar in the first image indicates the size scale that applies to all images. All images are displayed on a greyscale with an x^2 stretch but limits were chosen independently for each image such that nearby contiunuum sources and sky levels have a similar appearance for each object in all bands. Above, SNRcs 1-16: Note 14 has radio and x-ray counterparts.

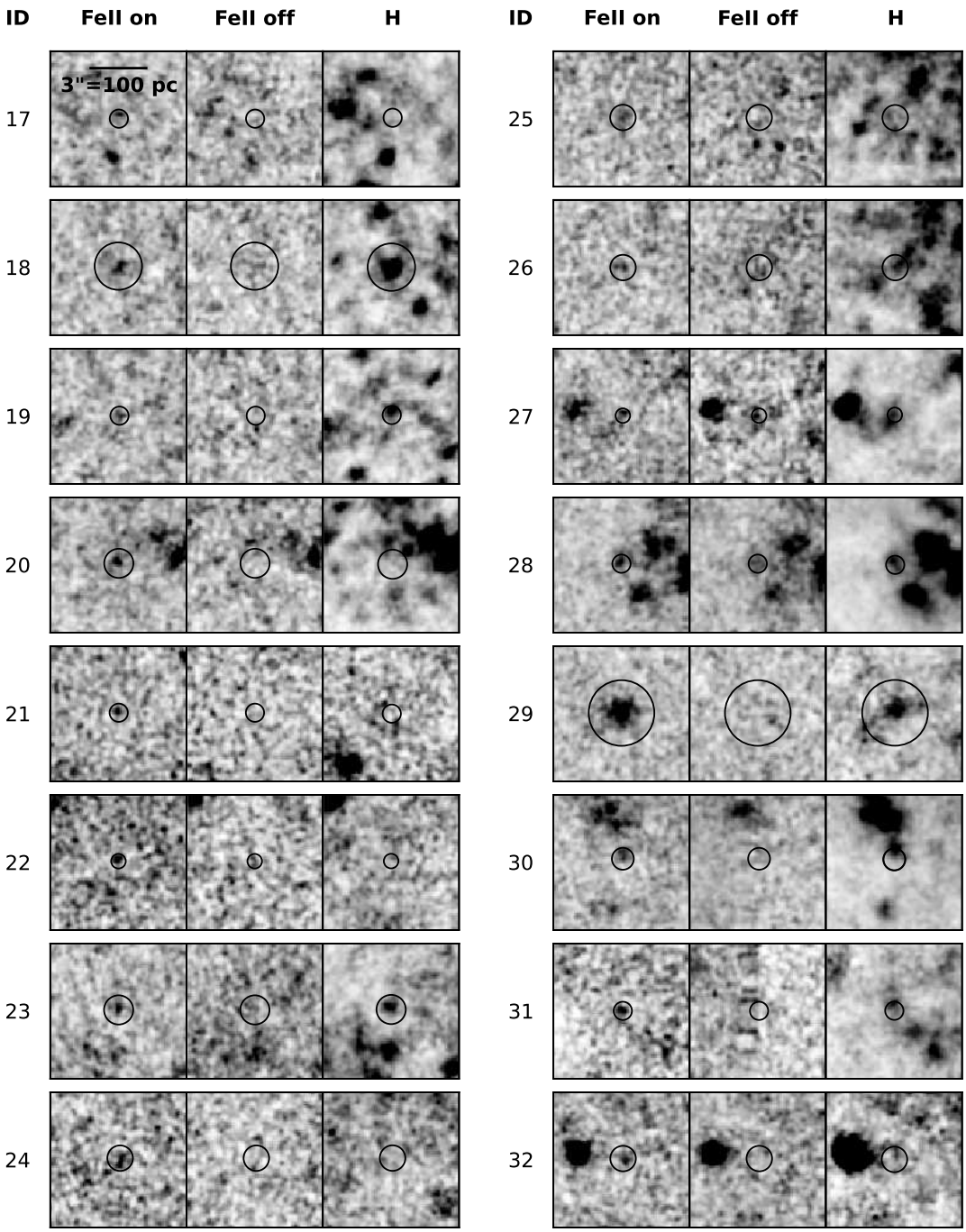

Figure 2.8 See Figure 2.7 caption for details. Above, SNRcs 17-32: Note 20 has radio and x-ray counterparts and 23 has an x-ray counterpart. 25 and 29 were identified as SNRcs in Matonick & Fesen (1997). Furthermore, 29 also has radio and x-ray counterparts and has been the subject of a number of previous studies due to its luminous nature.

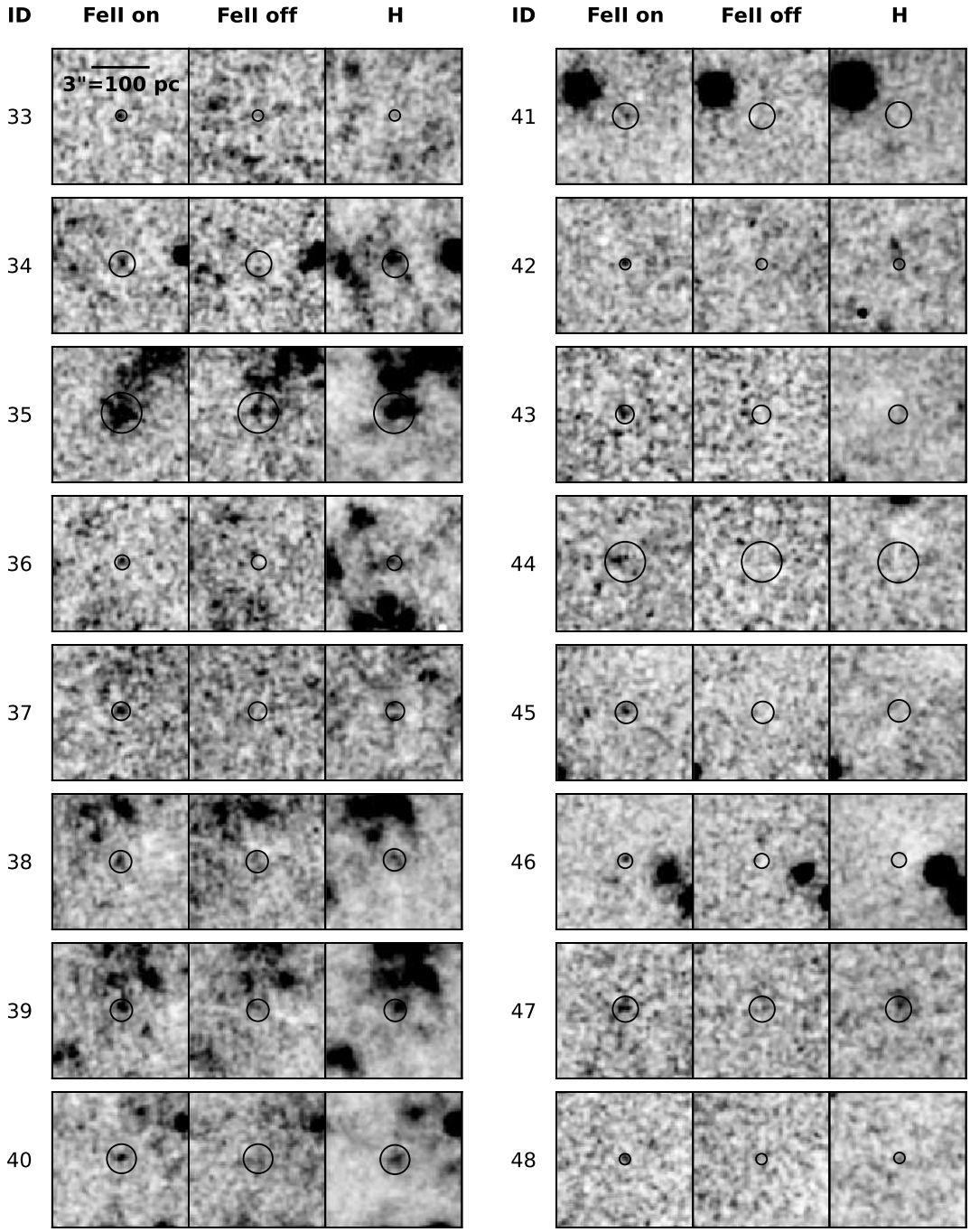

Figure 2.9 /smallSee Figure 2.7 caption for details. Above, SNRcs 33-48: Note 35 was classified as a SNRc in Hyman et al. (2000) based on radio observations and also has an x-ray counterpart.

A more quantitative analysis of the other objects along with potential implications for their nature and the local environments within NGC 6946 will be given in an upcoming paper. The associations with previously identified SNRcs adds to our confidence that we have successfully identified SNRs in NGC 6946. Finally, thumbnails of all 48 [Fe II]SNRcs are displayed in Figures 2.7, 2.8 and 2.9, showing how each SNRc appears in the [Fe II], $[\mathrm{Fe\,II}]_{\mathrm{Off}}$ and H bands.

2.5 Summary and Conclusions

We have used the WIYN High Resolution Infrared Camera (WHIRC) on the WIYN 3.5m telescope to image NGC 6946 in narrow bands [Fe II], $[\mathrm{Fe\,II}]_{\mathrm{Off}}$, Pa$\beta$, Pa$\beta_{\mathrm{Off}}$ and broad bands, J and H. Our goal was to evaluate the potential usefulness of using [Fe II] imaging combined with dedicated $[\mathrm{Fe\,II}]_{\mathrm{Off}}$ imaging to locate extragalactic SNRs. We identified 48 objects as supernova remnant candidates (SNRcs) based on their visual appearance in the [Fe II] and $[\mathrm{Fe\,II}]_{\mathrm{Off}}$ bands, in addition to their appearance, or lack thereof, in the J and H bands. Our SNRcs generally have the point-like appearance we expect and are distributed spatially along the spiral arm structure of NGC 6946 while few are found in the sparse interarm or outer regions of the galaxy.

Our SNRcs range in luminosity from 6×10^{35} to 1.8×10^{37} erg s^{-1}. Compared to galactic and extragalactic SNRs with measured [Fe II] fluxes , our SNRcs have some of the highest measured [Fe II] luminosities, especially when compared to galactic SNRs. The measured [Fe II] fluxes of our SNRcs is consistent with those found in other local starbursting galaxies. When compared to results from previous surveys of NGC 6946, six of our [Fe II] SNRcs are coincident with sources or SNRcs from radio, optical or x-ray methods. Additionally, the spatial distribution of our sources throughout the spiral arms is qualitatively similar to the types of distributions seen for SNRcs found through various wavelength searches in NGC 6946, as well as in other galaxies such as M33 (Long et al. 2010) and M83 (Blair et al. 2012).

We are reasonably confindent that our candidates are SNRs, but would like to emphasize that spectroscopy is needed for confirmation. Most of our [Fe II] SNRcs are not coincident with SNRs identified from previous radio, x-ray or optical searches. [Fe II] imaging favors the detections of SNRs in dusty areas of the galaxy. We suspect, however, that the pri-

mary reason that NGC 6946's SNRc samples from different wavelengths are so disjoint is that none of the surveys is sufficiently sensitive to detect the bulk of the SNR population. Clearly, deeper [Fe II] observations are needed to determine the the IR properties of these other candidates, and to determine what environmental factors favor detection of SNRs as [Fe II] emissison nebulae. Nonetheless, we have shown that using [Fe II] imaging with dedicated $[\mathrm{Fe\,II}]_{\mathrm{Off}}$ band imaging is an effective way to detect a significant number of extragalactic candidate SNRs which will help us to better understand issues such as these.

Chapter 3

Refining the [Fe II] SNRc list for NGC 6946

3.1 Introduction

This chapter is outlined as follows. Section 3.2 discusses the purpose for and layout of our re-imaging of NGC 6946, as well as the image processing method. Section 3.3 explains the measurements of flux and the following results from analyzing the new [Fe II] images, first in a 'test field' to verify previous results and then in our 'north field' to fill in gaps from our original investigation. Section 3.4 presents our final list of 72 [Fe II] SNR candidates (SNRcs) and their associated luminosities. This is followed by an exploration of the estimated SN rate for NGC 6946 and also on the connection between radio, [Fe II], optical and X-ray sources in NGC 6946. Section 3.5 summarizes the major points from this follow-up investigation.

3.2 Observations & Image Processing

In October 2013, we imaged selected regions of NGC 6946 in the [Fe II] and $[\text{Fe II}]_{\text{Off}}$ filters with the WIYN High Resolution Infrared Camera (WHIRC; Meixner et al. 2010). As discussed in Chapter 2, we had previously obtained imaging of NGC 6946 (between 2009 and 2011) to form mosaics in six filters: narrow bands [Fe II], $[\text{Fe II}]_{\text{Off}}$, Pa$\beta$ and Paβ_{Off} and broad bands J and H. Our new observations were chosen so as to verify and add to this

previous data set.

In the original data set, weather conditions caused variable seeing and data quality across the [Fe II] mosaic such that it was difficult to perform our data analysis in a region, approximately $6' \times 1'$ in size, located just north of the central core of NGC 6946. This region (we have labeled as the 'north field') had a very small number of identifiable SNRcs in the original analysis, a fact we suspected was due to image quality issues. We designed our new observations to re-image this area in the [Fe II] band. Additionally, we chose a region with a large number of SNRcs to serve as a 'test field', with which we could verify our previously obtained results. Figure 3.1 displays the chosen locations of the north field and test field overlayed on the original H band mosaic, and shows the 48 originally identified SNRcs for reference. On the right hand side, a combined mosaic of the new [Fe II] observations is shown.

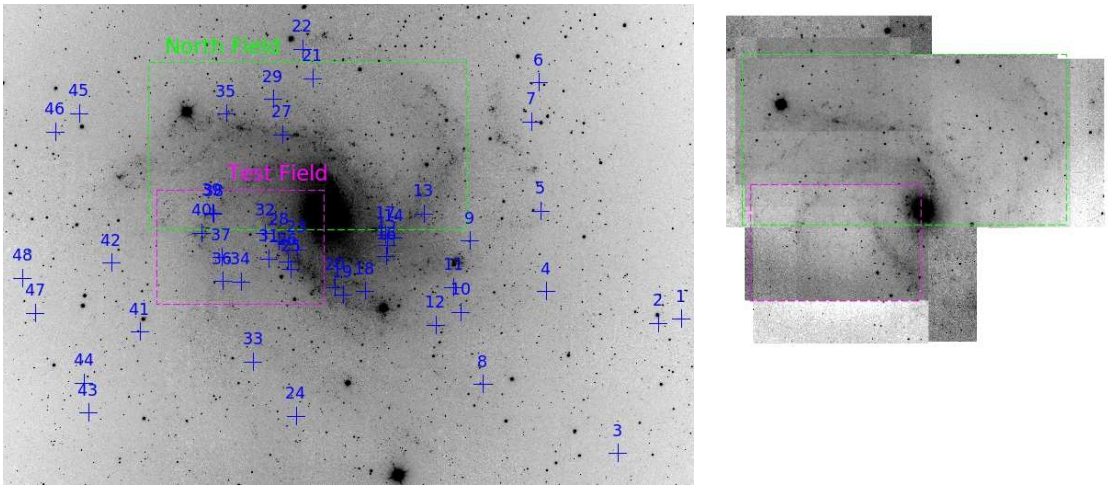

Figure 3.1 (*left*) The 48 SNRcs from Chapter 2 are indicated as crosses on the H band mosaic while dashed lines outline the north field and test field. (*right*) A mosaic of the new [Fe II] observations is shown with dashed lines indicating the north and test fields.

The observational parameters for the new data set are given in Table 3.1. The data reductions were done using the same process as described in Bruursema et al. (2014). An in-house python-wrapped IRAF script was used for most basic image processing such as flat-fielding, sky subtractions and fixing bad pixels. For our new data, a dedicated sky field was obtained and used on the test field. However, for the north field, the sky was estimated using a scaled, median addition, of 5 star-masked images from the north field data set. The north field sky was estimated this way to offer some uniformity, since our intention was to

Table 3.1. New Observations Log.

Band	Obs-Date (YY-MM-DD)	Total Exp. per Pointing (sec)	Mosaic Size (frames)/(′)	N Dithers (Dither Pattern)	Seeing FWHM (″)	Airmass	Comments
			Test Field				
[Fe II]	13-10-18	1040	NA /3×3	4(2×2)	0.8	1.4	clear
$[Fe\,II]_{Off}$	13-10-18	1040	NA /3×3	4(2×2)	0.8	1.5	clear
			North Field				
[Fe II]	13-10-19	1040	2×1/6×3	4(2×2)	0.7-0.9	1.2	clear

Note. — In Column 5, $DitherPattern$ gives the number of images east to west by number of images north to south, the resulting total number of images in a pointing is reported as $NDithers$, and the total exposure time for a pointing is given in Column 3, meaning each image has an exposure time found by dividing the time given in Column 3 by $NDithers$.

combine the results from the north field with our previous data set for analysis. The world coordinate system for all images was fixed using WCSTOOLS to match stellar positions as listed in the 2MASS catalog and Montage[5] was used to combine all images.

3.3 Data Analysis

We tested our previous work by analyzing the test field in order to ensure agreement between our newer data and our previous data sets. There are a number of reasons why we would expect our new test field image to be a superior image for identifying SNRcs over our previous mosaic image. These reasons include better weather while observing, deeper imaging, and additional pointings added in each dither set (to help combat the effects of spurrious image defects). The results of the test field analysis are discussed in Section 3.3.2. Additionally, the north field was visually searched for SNR candidates using our previously developed process, as is described in Section 3.3.3. These analyses rely largely on measured

[5]http://montage.ipac.caltech.edu

[Fe II] flux values, as well as $[\text{Fe II}]_{\text{Off}}$ and H band fluxes as well, which shall be discussed first.

3.3.1 Flux measurements

The new [Fe II] fluxes were calibrated using 2MASS stars located within the combined region of both the test field and the north field. Stars that had 2MASS data quality flags, or that seemed confused with a nearby object or were exceedingly bright were removed from the calibration leaving us with 100 of the possible 217 2MASS stars in the field. Then, since the [Fe II] filter lies within the H filter of 2MASS, the expected flux for these stars in the WHIRC [Fe II] filter can be calculated using their H-band magnitudes as given in the 2MASS catalog ($m_{H,2MASS}$), and the appropriate filter width from Table 2.1 ($\Delta\lambda$). Correcting also for line of sight extinction yields the following equation:

$$F([\text{Fe II}]) = f_{H=0}\Delta\lambda_{[\text{Fe II}]}\ 10^{-0.4(m_{H,2MASS}-A_H)} \tag{3.1}$$

where $f_{H=0}$=1.133 $\times 10^{-13} \pm 2.212\ 10^{-15}$ W cm^{-2} μm^{-1} is the H-band flux for 0 magnitude stars in the 2MASS survey (Carpenter 2001) and A_H=0.154 as given in Table 1.2.

Aperture photometry with r_{aper}=2.5″, r_{skyann}=3″ and d_{ann}=1″ was used to measure counts from our [Fe II] image for the 100 calibration stars. When plotting these results against the fluxes in erg s^{-1} cm^{-2} found using Equation 3.1, a linear regression yields the following flux calibration:

$$F([\text{Fe II}]) = 7 \times 10^{-19}\ S_{[\text{Fe II}]}, \tag{3.2}$$

where S represents the total amount of counts measured from the WHIRC image within the photometric aperture, subtracting the sky contribution, and F is the extinction corrected flux of the object in erg s^{-1} cm^{-2}. The same method gives similar calibrations for the $[\text{Fe II}]_{\text{Off}}$ and H band fluxes as reported in Bruursema et al. (2014).

Fluxes for SNRcs were determined using Equation 3.2, where S was measured with aperture photometry, so that local diffuse components of [Fe II] or diffuse continuum would be automatically removed. Apertures and sky annuli were carefully chosen with the aid of a curve-of-growth inspection, considerations of local seeing conditions and locations of nearby objects. Additionally, we noted the appearance of the object in all photometric bands, to ensure all fluxes would be accurate while using the same aperture set. The apertures and sky annuli are noted in Tables 3.2 and 3.3.

In most cases, when measuring fluxes for previously identified SNRcs, the aperture and sky annuli parameters are unchanged from our original analysis. In some cases though, adjustments on the scale of 1-4 pixels were made to object locations or photometric apertures to properly encompass the desired objects within the new image. These adjustments are reasonable considering the seeing conditions were measured as having FWHM between 6 and 11 pixels in the original mosaic, and about 8 pixels in the test field. This also informs us of the approximate astrometric accuracy of our work.

For an estimate of the local statistical noise for each object, we also measured $\sigma_{\rm sky}$, the standard deviation of counts for the pixels within the sky annulus. Then, a statistical S/N was calculated as:

$$S/N = \frac{S}{\sigma_{\rm sky}\sqrt{\pi r_{aper}^2}}, \tag{3.3}$$

where r_{aper} is the radius of the object's photometric aperture in pixels. This parameter, when combined with a careful consideration of each object's visual appearance, was found to be a useful tool in selecting objects of high confidence.

3.3.1.1 Continuum subtraction

The [Fe II] fluxes discussed above are subtracted for diffuse components of [Fe II] or continuum emission. Yet there is always the possibility of localized continuum emission at the location of a SNRc. Therefore, to estimate the [Fe II] emission for all objects, we must subtract any continuum emission measured at that location. By investigating the range of [Fe II]$_{\rm Off}$ fluxes and their associated S/N values, all [Fe II]$_{\rm Off}$ flux measurements with S/N values less than 3 were determined to be non-detections, thus effectively have [Fe II]$_{\rm Off}$ flux values of zero. Therefore, the only objects which need to be continuum subtracted are those with [Fe II]$_{\rm Off}$ S/N values greater than 3. For such objects, final reported [Fe II] emission luminosities are calculated from $F([\text{Fe II}]) - F([\text{Fe II}]_{\rm Off})$ values, to ensure all reported luminosities correctly account for continuum emission..

3.3.2 Test Field

The test field contained 13 of our previously identified SNRcs. We investigated the [Fe II] and [Fe II]$_{\rm Off}$ band appearance of our previously identified [Fe II] SNRcs, with the

expectation that the SNRcs would be identifiable in the new data if they were real objects. In this assesment, we were able to confirm that 11 of these were clearly present. We believe we would have re-identified these 11 objects as SNRcs if we were to repeat the visual search method initially used to identify them. However we found that 2 objects, SNRc32 and SNRc37, could not be identified via our visual search method within the new data set.

To understand the visual assessment and to further investigate our previous results, we examined the flux for these 13 candidates and compared the [Fe II] fluxes and S/N levels to those values measured from the original data set. Table 3.2 reports the newly measured [Fe II] fluxes for these 13 test field SNRcs. The two SNRcs which could not be visually confirmed were found to have the two lowest S/N values in the new [Fe II] image.

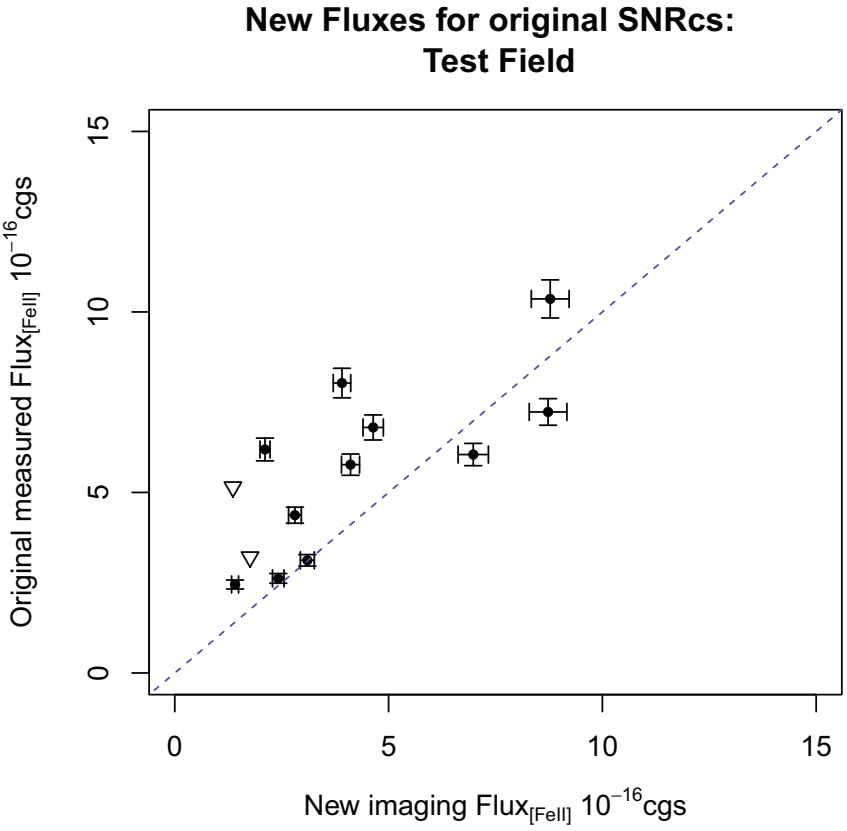

Figure 3.2 The 13 previously identified SNRcs which were re-observed in the test field are displayed, showing how the newer, deeper imaging flux compares to the originally measured flux. The two triangle points indicate [Fe II] flux upper limits SNRcs 32 and 37, which had a S/N < 4.4 in the new [Fe II] imaging, and so were considered non-detections in [Fe II].

Table 3.2. New Flux Measurements for Previously Identified SNRcs.

Prev ID	New ID	RA (J2000) (deg.)	DEC (J2000) (deg.)	$F([\mathrm{Fe\,II}])$ ($10^{-16}\frac{erg}{s\ cm^2}$)	[Fe II] S/N	$F([\mathrm{Fe\,II}]_{\mathrm{Off}})$ ($10^{-16}\frac{erg}{s\ cm^2}$)	$F(H)$ ($10^{-16}\frac{erg}{s\ cm^2}$)	Aper (pix.)	SkyAnn (pix.)	AnnD (pix.)
				Test Field						
23	42	308.73687	+60.1423810	3.91 ±0.86	4.5	<0.87	<2.86	8	10	16
25	44	308.74091	+60.1361070	8.73 ±0.71	12.4	<0.63	<2.51	7	9	15
26	45	308.74305	+60.1382950	4.11 ±0.64	6.4	<0.76	<2.93	7	10	15
28	49	308.74896	+60.1449738	8.78 ±0.58	15.3	3.72 ±.54	111.02 ±3.10	6	7	12
30	54	308.75552	+60.1499540	2.11 ±0.48	4.4	<0.58	44.88 ±3.34	6	7	12
31	55	308.75561	+60.1393840	2.42 ±0.53	4.5	<0.48	<0.87	5	7	14
32		308.75798	+60.1478530	<1.41	2.9	<0.53	<1.57	5	6	12
34	57	308.77426	+60.1318110	3.10 ±0.62	5.0	<0.59	<2.03	7	8	13
36	60	308.78644	+60.1319640	1.41 ±0.31	4.5	<0.36	<1.33	4	6	10
37		308.78678	+60.1397550	<1.82	3.5	<0.48	<3.13	5	6	13
38		308.79219	+60.1541680	2.81 ±0.49	5.7	3.41 ±.43	16.18 ±5.34	6	7	12
39	61	308.79294	+60.1544730	4.64 ±0.50	9.3	3.68 ±.60	<4.08	6	7	10
40	62	308.80002	+60.1478660	6.98 ±0.79	8.8	3.58 ±.77	43.17 ±3.79	8	9	15
				North Field						
13		308.65307	+60.1542130	<1.30	2.1	<0.75	12.04 ±2.19	4	6	12
21		308.72656	+60.1988060	<0.93	2.7	<0.58	<3.54	5	6	11
27	46	308.74688	+60.1802720	1.51 ±0.29	5.2	<0.41	<2.10	5	6	11
29	52	308.75303	+60.1918990	48.44 ±1.06	45.9	15.66 ±1.44	121.43 ±6.32	18	20	23
35	59	308.78390	+60.1870360	14.94 ±0.79	18.9	<1.22	153.02 ±7.02	11	13	16

Note. — The listed flux errors are σ_{sky} extraction errors. [Fe II] fluxes reported in column 5 are not continuum subtracted, they are the extinction corrected fluxes measured from the [Fe II] image. Sources with [Fe II] S/N measurements < 4.4 are defined as non-detections. $[\mathrm{Fe\,II}]_{\mathrm{Off}}$ and H, fluxes with S/N < 3 and 2, respectively, are considered non-detections. For flux measurements considered non-detections, upper limits are reported.

Considering this, we set a corresponding defining threshold of [Fe II] S/N $\geq$ 4.4 to be the criteria for a [Fe II] flux detection, meaning any object in the new data set with a [Fe II] S/N $<$ 4.4 would be a non-detection. Figure 3.2 shows the new [Fe II] flux values plotted vs. the originally measured [Fe II] fluxes. The two triangle symbols represent upper limits for the two non-detections. From this comparison, we can see that while our photometric errors are likely a bit larger than we have reported, there is a strong correlation between the fluxes measured from the two different images. This raises our confidence in the accuracy of our flux measurements.

Thus far, through our flux analysis of the test field, we eliminated SNRcs 32 and 37 as SNR candidates and were able to set defining criteria for confident [Fe II] detections. Additionally, we found that with a $[\text{Fe II}]_{\text{Off}}/[\text{Fe II}]$ ratio of 1.21, SNRc38 was likely to be a continuum source as opposed to an [Fe II] emission source. Therefore, SNRc 38 was also eliminated as a SNR candidate. As shown in Table 3.2, SNRc39 (the extremely close neigbor of SNRc38) has a very high $[\text{Fe II}]_{\text{Off}}/[\text{Fe II}]$ ratio for a SNRc, at 0.79. Regardless, this candidate is allowed in our final SNRc list because it is clear that there is a strong source of [Fe II] emission very close to that location, although there seems to be some confusion of sources as well which is making it difficult to isolate the precise continuum level for the [Fe II] emission source. However, the coordinates for SNRc39 seems to be the best estimate of the location of this [Fe II] source.

Finally, to further compare [Fe II] flux measurements from the original data set with the new data set, the 5 SNRcs located in the North field were analyzed in combination with the 13 test field SNRcs. As can be seen in Table 3.2, two of these 5 SNRcs (SNRc13 and SNRc21) were non-detections in the new mosaic and as such, were eliminated as SNRcs. Figure 3.3 combines the north field data points with those of the test field as plotted in Figure 3.2. The north field SNRc flux values, plotted in purple, further illustrate the linear correspondence and help form a picture of the accuracy of our measured [Fe II] flux values.

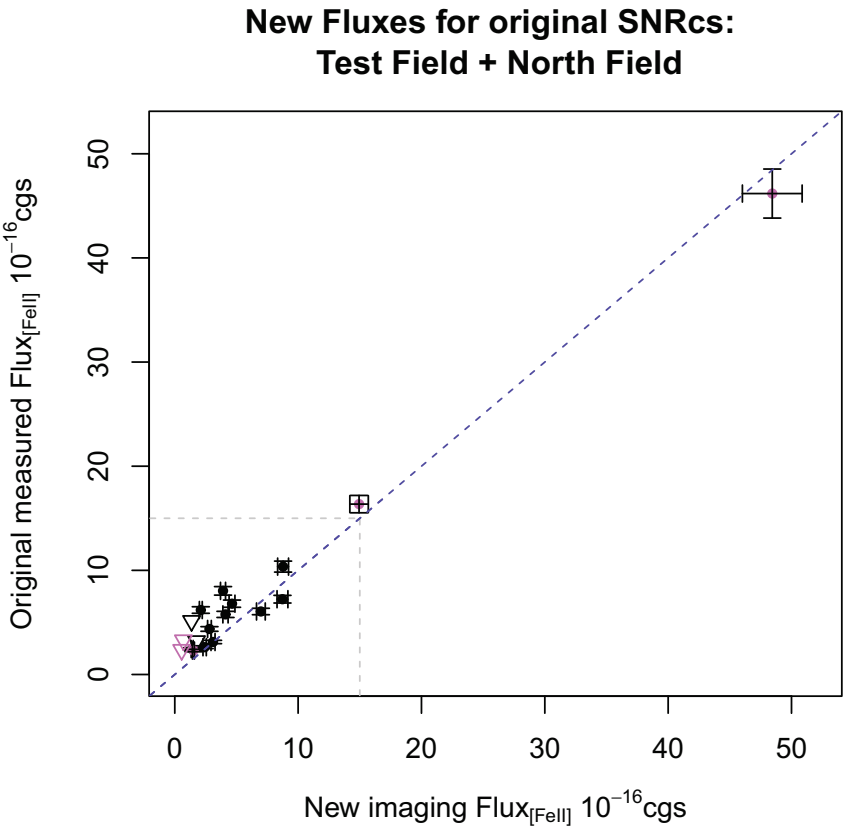

Figure 3.3 This is an expanded view of the graph shown in Figure 3.2 (the limits of which are denoted by gray dashed lines). Added in purple are the 5 previously identified SNRcs present in the north field data set, to give a full 'new vs. old' flux comparison for the SNRcs. Again, triangles indicate upper limits where SNRcs had a S/N < 4.4 in the new [Fe II] imaging.

3.3.3 North Field - SNRc identification

The north field region in the original [Fe II] mosaic had a lower image quality which made it effectively impossible to identify any but the very brightest SNRcs (only 5 SNRcs were previously identified in this area). Thus, to fill in the gap of our previous analysis, we performed a careful visual search of the north field to identify new SNRcs. As before, this search was done with no a priori indication of locations of previously identified SNRcs (from any study), and due to the high resolution imaging, it was not even always clear which part of the galaxy was being searched.

The search was conducted by comparing the north field ([Fe II] image) to the corresponding fields in our previously obtained $[\mathrm{Fe\,II}]_{\mathrm{Off}}$ and H band images. The goal was to identify objects which were clearly identifiable in the north field while being very much less significant or absent in the $[\mathrm{Fe\,II}]_{\mathrm{Off}}$ and H filters. Together, the $[\mathrm{Fe\,II}]_{\mathrm{Off}}$ and H band images give a very good estimate of the continuum levels, and when compared to the [Fe II] image, reveal [Fe II] emission objects.

In the initial visual search, all potential strong [Fe II] emission objects were noted, but due to the existence of image artifacts, the individual frames which comprised the final image had to be examined to ensure all objects were real. The small, bright, image artifacts were not always removed by the image stacking process, for example, when only 3 frames combined for the final image, at the edges of the field. Due to the existence of these artifacts, which had a range of visual appearances, we eliminated all objects from our list that appeared to be largely the result of a significantly bright source in just one frame.

It should be noted that, due to the expected faintness of these SNR objects and the variable seeing conditions in each frame, it would be possible for a SNR to appear substantially brighter in just one frame. However, to ensure high confidence in all objects, we required that any SNRc be visible in at least 2 frames. After analyzing the individual frames of the new [Fe II] north field objects, we decided to re-examine the individual frame appearance of the original SNRcs from the first [Fe II] mosaic. Through this process, SNRc46 was only found to be substantially visible in one frame, and so was eliminated as a SNR candididate.

In order to make it onto our final list as a SNRc, these objects had to have measured fluxes that agreed with our visual assessment. Therefore, we measured [Fe II], $[\mathrm{Fe\,II}]_{\mathrm{Off}}$ and H fluxes for all objects and investigated the $[\mathrm{Fe\,II}]_{\mathrm{Off}}/[\mathrm{Fe\,II}]$ and $H/[\mathrm{Fe\,II}]$ flux ratios to eliminate any continuum sources. As defined previously, any objects with a [Fe II] S/N <4.4 were cut as non-detections. Objects that had $[\mathrm{Fe\,II}]_{\mathrm{Off}}/[\mathrm{Fe\,II}]$ flux ratios greater than 0.5 or $H/[\mathrm{Fe\,II}]$ flux ratio greater than 10 were considered to be continuum sources. However, in the central core region of the galaxy (within 1 kpc of the galaxy center), these flux ratio limits were increased to allow for the increased likelihood of localized continuum source contamination near the SNRc. In all, 4 objects were allowed to exceed the limits, and these objects have $H/[\mathrm{Fe\,II}]$ flux ratios greater than 10, but less than 18.35, where 18.35 is the ratio that would be expected for a continuum object, assuming a flat spectrum across the H band.

Following the analysis described above, 30 new objects were identified as SNRcs. These new candidates have measured fluxes as reported in Table 3.3 and are displayed as cyan crosses in Figure 3.4. Also in Figure 3.4, the original SNRcs are colored red if they were eliminated as SNR candidates and are blue if they remain candidates after the secondary analysis. Adding the 30 new candidates to the 48 previous candidates and eliminating SNRcs 13, 21, 32 and 37 as non-dections, SNRc 38 as a continuum source and SNRc 46 as a defect, we are left with a total of 72 final [Fe II] selected SNR candidates in NGC 6946. A discussion of these 72 final SNRcs will follow in the next section.

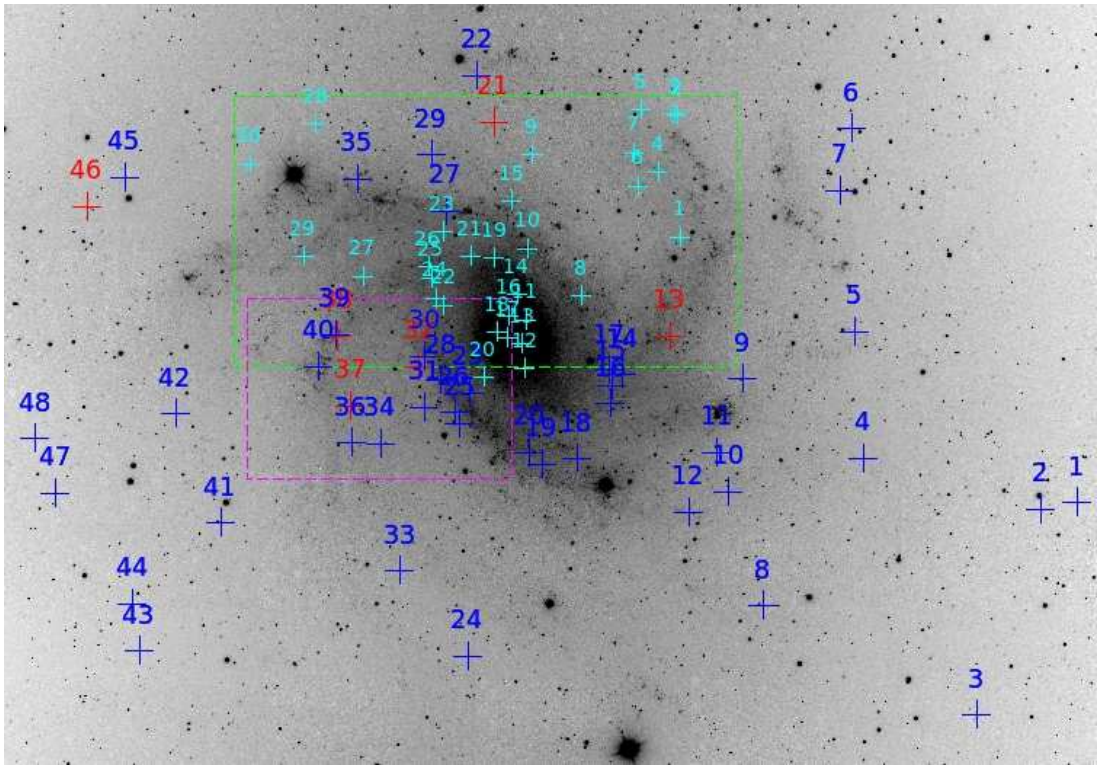

Figure 3.4 Cyan crosses indicate new SNRcs from the new north field data. Blue crosses are the original [Fe II] SNRcs which remain as SNRcs while red crosses are the original [Fe II] SNRcs which were eliminated as SNR candidates. The north and test fields are denoted with dashed lines.

Table 3.3. Flux Measurements for Newly Identified SNRcs.

New ID	RA (J2000) (deg.)	DEC (J2000) (deg.)	$F([\mathrm{Fe\,II}])$ ($10^{-16}\frac{erg}{s\ cm^2}$)	[Fe II] S/N	$F([\mathrm{Fe\,II}]_{\mathrm{Off}})$ ($10^{-16}\frac{erg}{s\ cm^2}$)	$F(H)$ ($10^{-16}\frac{erg}{s\ cm^2}$)	Aper (pix.)	SkyAnn (pix.)	AnnD (pix.)
13	308.64875	+60.1748830	3.25 ±0.37	8.8	<0.43	6.29 ±1.49	6	7	11
14	308.64971	+60.2001850	2.93 ±0.41	7.2	<0.49	12.27 ±2.15	6	7	11
15	308.65106	+60.2004000	3.48 ±0.36	9.6	<0.42	22.73 ±1.78	6	7	11
16	308.65779	+60.1883200	1.95 ±0.35	5.6	<0.50	<2.73	6	7	11
17	308.66501	+60.2013860	2.07 ±0.42	4.9	<0.39	19.75 ±1.91	6	7	11
18	308.66605	+60.1855120	4.24 ±0.34	12.6	1.13 ±0.36	18.78 ±1.95	6	7	11
19	308.66815	+60.1923550	3.31 ±0.38	8.7	<0.31	<2.13	6	7	11
24	308.68993	+60.1625640	1.86 ±0.25	7.4	<0.28	5.72 ±1.77	4	5	9
27	308.71071	+60.1919130	8.38 ±0.70	11.9	<1.03	62.45 ±4.44	10	11	15
29	308.71223	+60.1724360	61.76 ±0.72	86.2	11.62 ±1.07	447.46 ±7.11	11	45	48
30	308.71337	+60.1575380	3.87 ±0.41	9.4	<0.58	63.78 ±4.78	6	7	11
31	308.71360	+60.1473950	13.92 ±1.01	13.9	4.26 ±1.06	15.78 ±6.02	10	11	15
32	308.71484	+60.1525640	5.25 ±0.64	8.2	<0.81	75.01 ±7.49	6	7	9
33	308.71688	+60.1629280	1.22 ±0.25	4.8	<0.44	6.95 ±2.06	4	5	9
34	308.71899	+60.1822380	2.06 ±0.25	8.3	<0.36	11.38 ±2.09	4	5	9
35	308.72016	+60.1584490	7.78 ±0.39	20.0	<0.61	88.27 ±2.99	6	7	11
36	308.72080	+60.1540120	20.11 ±1.63	12.4	9.62 ±1.29	192.69 ±24.95	6	7	9
37	308.72516	+60.1549420	2.72 ±0.29	9.4	<0.49	43.64 ±2.19	4	5	9
38	308.72629	+60.1704240	3.68 ±0.38	9.7	<0.54	8.67 ±3.29	6	7	11
39	308.73079	+60.1455770	8.32 ±0.51	16.4	2.60 ±0.65	62.05 ±2.28	6	7	11
41	308.73650	+60.1707910	1.68 ±0.31	5.4	<0.34	<1.49	4	5	9
47	308.74779	+60.1606710	10.45 ±0.69	15.2	<1.05	39.65 ±3.62	10	11	15
48	308.74796	+60.1759270	1.84 ±0.35	5.3	<0.55	<2.04	6	7	11
50	308.75090	+60.1621550	9.47 ±0.59	16.1	4.00 ±0.68	74.27 ±3.01	10	11	15
51	308.75285	+60.1664350	9.05 ±0.65	13.9	<0.94	86.15 ±3.60	10	11	15
53	308.75399	+60.1686120	2.66 ±0.39	6.8	<0.57	<2.46	6	7	11
58	308.78147	+60.1666020	1.98 ±0.37	5.3	<0.55	<2.31	6	7	11
63	308.80126	+60.1983290	6.33 ±0.63	10.1	<0.94	21.08 ±4.26	10	11	15
64	308.80662	+60.1707250	3.79 ±0.43	8.9	1.81 ±0.57	16.28 ±2.45	6	7	11
65	308.82910	+60.1899970	3.08 ±0.46	6.7	<0.56	4.81 ±1.61	6	7	11

Note. — All reported flux errors are σ_{sky} extraction errors. [Fe II] fluxes reported in column 5 are not continuum subtracted, they are the extinction corrected fluxes measured from the [Fe II] image. $[\mathrm{Fe\,II}]_{\mathrm{Off}}$ and H, fluxes with S/N < 3 and 2, respectively, are considered non-detections. For flux measurements considered non-detections, upper limits are reported.

3.4 Results & Discussion

The final 72 [Fe II] selected SNRcs are distributed as shown in Figure 3.5. In general, the majority of these candidates are seen to be associated with the denser, star-forming regions of the spiral arms. This was the case for the initial candidate list in Chapter 2, and continues to be the case for the 30 new candidates from the north field inspection.

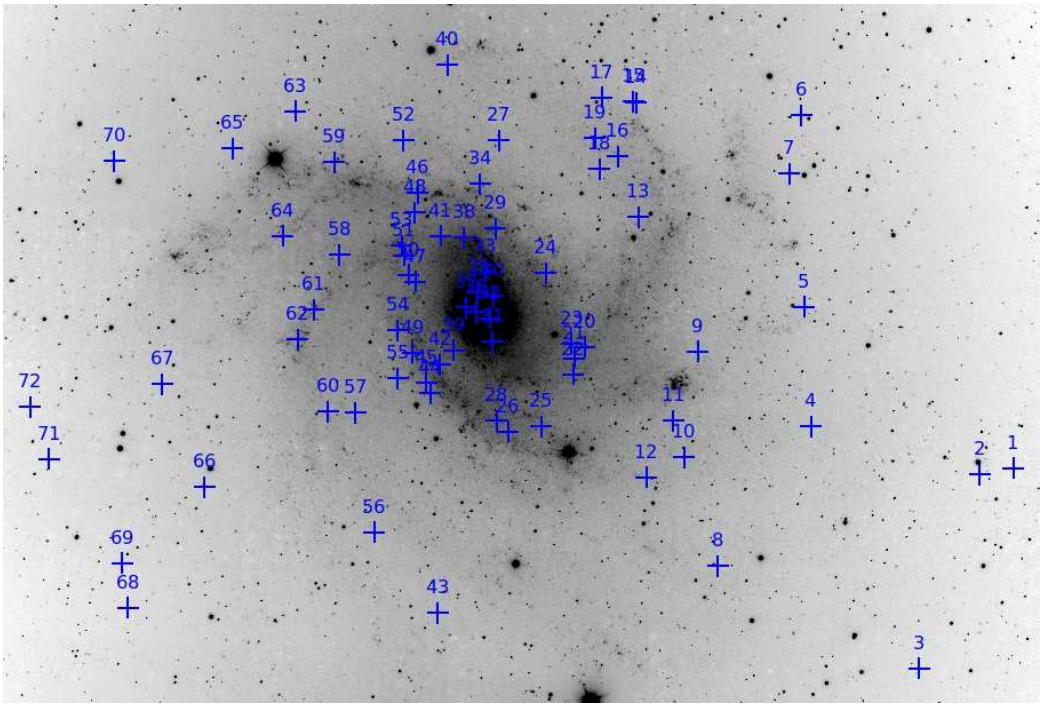

Figure 3.5 The final 72 SNRcs are displayed here. These include all except 6 of the previous SNRcs (from Chapter 2) plus 30 new ones. They have been assigned new identification numbers so they are numbered sequentially in order of increasing Right Ascension.

Extinction corrected flux measurements for all 72 candidates are presented in Table 3.4, although upper limits are reported where measurements were determined to be non-detections. By plotting the distribution of $[\mathrm{Fe\,II}]_{\mathrm{Off}}$ fluxes for our total list of 72 SNRcs, we can clarify the use of various S/N cuts to determine non-detections versus confident detections. To this end, Figure 3.6 displays the distribution of $[\mathrm{Fe\,II}]_{\mathrm{Off}}$ fluxes for the SNRcs.

Generally, as per the design of the $[\mathrm{Fe\,II}]_{\mathrm{Off}}$ filter, there should be zero flux measured in the $[\mathrm{Fe\,II}]_{\mathrm{Off}}$ band, unless there is local contamination by a continuum source. Thus, the majority of measured fluxes can be seen to be normally about zero, where the gaussian's

properties indicate the noise statistics of the [Fe II]$_{\rm Off}$ image. A few outliers from the normal distribution are expected on the positive end, as there can be some SNRcs which are located near continuum sources. In Figure 3.6, SNRcs are colored red if they had been previously determined to be non-zero based on an investigation of the range of measured fluxes and the range of calculated "S/N" parameter. The red bins show that our previous assessment corectly identified the desired outliers from the normal distribution about zero. The distribution was empirically fit with a gaussian and yielded a σ_{sys} of approximately 1×10^{-16} erg s^{-1} cm^{-2}. This uncertainty in [Fe II]$_{\rm Off}$ flux should represent error from systematics in the data such as structured emission and possible undetected artifacts. We think the uncertainty in the [Fe II] filter should be comparable to this [Fe II]$_{\rm Off}$ uncertainty.

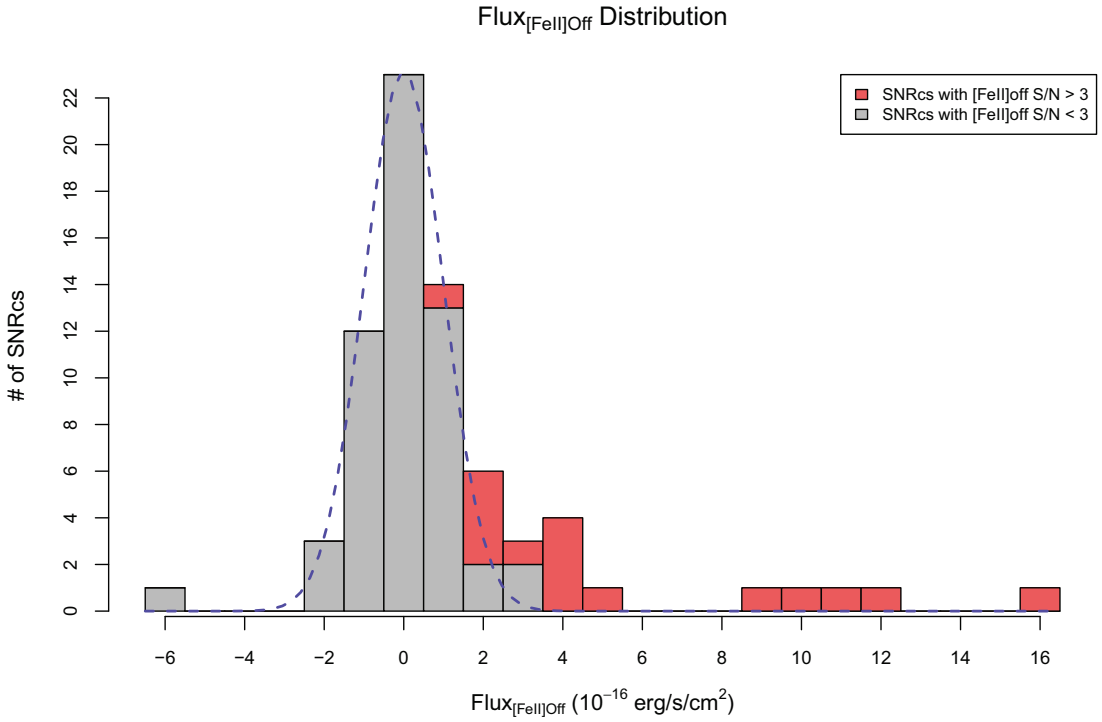

Figure 3.6 The [Fe II]$_{\rm Off}$ fluxes for the final 72 SNRcs are displayed in this histogram. Red bins indicate SNRcs that were determined to have significant continuum components while the rest are considered to be consistent with a [Fe II]$_{\rm Off}$ flux of zero. Most SNRcs are normally distributed about zero indicating poission noise at the level of σ_{sys}= 1$\times$ 10^{-16} erg s^{-1} cm^{-2}. The previously defined "S/N" cuts correctly identified the outliers of the normal distribution.

Table 3.4. Flux Measurements for the final 72 SNRcs.

New ID	Prev ID	RA (J2000) (deg.)	DEC (J2000) (deg.)	$F([\mathrm{Fe\,II}])$ ($10^{-16}\frac{erg}{s\ cm^2}$)	[Fe II] S/N	$F([\mathrm{Fe\,II}]_{\mathrm{Off}})$ ($10^{-16}\frac{erg}{s\ cm^2}$)	$F(H)$ ($10^{-16}\frac{erg}{s\ cm^2}$)	publ. c.p.	unpubl. c.p.
1	1	308.48267	+60.1193123	2.17 ± 0.30	7.1	<0.31	<1.70		
2	2	308.49762	+60.1179543	3.51 ± 0.38	9.2	<0.50	<2.07		
3	3	308.52478	+60.0751953	5.68 ± 0.78	7.3	<0.77	<2.54		
4	4	308.57217	+60.1286392	4.30 ± 0.50	8.6	<0.84	<1.76		
5	5	308.57523	+60.1551170	3.11 ± 0.46	6.7	<0.64	<1.55		
6	6	308.57643	+60.1973360	2.69 ± 0.42	6.4	<0.46	<1.56		
7	7	308.58175	+60.1844380	1.75 ± 0.28	6.3	<0.32	<0.98		
8	8	308.61377	+60.0979347	1.96 ± 0.29	6.9	<0.34	<1.59		
9	9	308.62234	+60.1452675	9.12 ± 0.82	11.1	<0.86	74.94 ± 3.13		
10	10	308.62851	+60.1218643	13.88 ± 1.24	11.2	9.15 ± 1.18	89.67 ± 5.13		
11	11	308.63330	+60.1299706	4.55 ± 0.67	6.7	<0.76	<2.59		
12	12	308.64529	+60.1175385	2.66 ± 0.36	7.5	<0.38	<1.29		
13		308.64875	+60.1748830	3.25 ± 0.37	8.8	<0.43	6.29 ± 1.49		
14		308.64971	+60.2001850	2.93 ± 0.41	7.2	<0.49	12.27 ± 2.15		
15		308.65106	+60.2004000	3.48 ± 0.36	9.6	<0.42	22.73 ± 1.78		
16		308.65779	+60.1883200	1.95 ± 0.35	5.6	<0.50	<2.73		
17		308.66501	+60.2013860	2.07 ± 0.42	4.9	<0.39	19.75 ± 1.91		
18		308.66605	+60.1855120	4.24 ± 0.34	12.6	1.13 ± 0.36	18.78 ± 1.95		
19		308.66815	+60.1923550	3.31 ± 0.38	8.7	<0.31	<2.13		
20	14	308.67279	+60.1462402	14.92 ± 0.49	30.2	5.15 ± 0.62	33.55 ± 2.84	Rx	x
21	15	308.67725	+60.1437569	22.92 ± 1.48	15.5	12.59 ± 1.51	101.08 ± 6.67		
22	16	308.67773	+60.1401901	5.06 ± 0.51	9.9	2.39 ± 0.73	23.11 ± 3.64		
23	17	308.67841	+60.1470680	3.04 ± 0.44	6.8	<0.57	<2.57		
24		308.68993	+60.1625640	1.86 ± 0.25	7.4	<0.28	5.72 ± 1.77		
25	18	308.69208	+60.1287003	16.35 ± 1.19	13.8	<1.20	158.95 ± 6.23		
26	19	308.70657	+60.1276321	3.29 ± 0.49	6.8	<0.54	19.61 ± 2.25		o
27		308.71071	+60.1919130	8.38 ± 0.70	11.9	<1.03	62.45 ± 4.44		
28	20	308.71173	+60.1299858	7.40 ± 0.87	8.5	<0.88	<4.45	rx	ox
29		308.71223	+60.1724360	61.76 ± 0.72	86.2	11.62 ± 1.07	447.46 ± 7.11	Rx	ox
30		308.71337	+60.1575380	3.87 ± 0.41	9.4	<0.58	63.78 ± 4.78		
31		308.71360	+60.1473950	13.92 ± 1.01	13.9	4.26 ± 1.06	15.78 ± 6.02		
32		308.71484	+60.1525640	5.25 ± 0.64	8.2	<0.81	75.01 ± 7.49	O	
33		308.71688	+60.1629280	1.22 ± 0.25	4.8	<0.44	6.95 ± 2.06		
34		308.71899	+60.1822380	2.06 ± 0.25	8.3	<0.36	11.38 ± 2.09		
35		308.72016	+60.1584490	7.78 ± 0.39	20.0	<0.61	88.27 ± 2.99	r	
36		308.72080	+60.1540120	20.11 ± 1.63	12.4	9.62 ± 1.29	192.69 ± 24.95		
37		308.72516	+60.1549420	2.72 ± 0.29	9.4	<0.49	43.64 ± 2.19		x
38		308.72629	+60.1704240	3.68 ± 0.38	9.7	<0.54	8.67 ± 3.29		

Table 3.4 (cont'd)

New ID	Prev ID	RA (J2000) (deg.)	DEC (J2000) (deg.)	$F([\mathrm{Fe\,II}])$ ($10^{-16}\frac{erg}{s\ cm^2}$)	[Fe II] S/N	$F([\mathrm{Fe\,II}]_{\mathrm{Off}})$ ($10^{-16}\frac{erg}{s\ cm^2}$)	$F(H)$ ($10^{-16}\frac{erg}{s\ cm^2}$)	publ. c.p.	unpubl. c.p.
39		308.73079	+60.1455770	8.32 ± 0.51	16.4	2.60 ± 0.65	62.05 ± 2.28		
40	22	308.73356	+60.2085220	2.15 ± 0.35	6.1	<0.39	<1.25		
41		308.73650	+60.1707910	1.68 ± 0.31	5.4	<0.34	<1.49		
42	23	308.73687	+60.1423810	3.91 ± 0.86	4.5	<0.87	<2.86		
43	24	308.73770	+60.0875282	5.85 ± 0.94	6.2	<0.86	<1.66		
44	25	308.74091	+60.1361070	8.73 ± 0.71	12.4	<0.63	<2.51	O	
45	26	308.74305	+60.1382950	4.11 ± 0.64	6.4	<0.76	<2.93		
46	27	308.74688	+60.1802720	1.51 ± 0.29	5.2	<0.41	<2.10		
47		308.74779	+60.1606710	10.45 ± 0.69	15.2	<1.05	39.65 ± 3.62		
48		308.74796	+60.1759270	1.84 ± 0.35	5.3	<0.55	<2.04		
49	28	308.74896	+60.1449738	8.78 ± 0.58	15.3	3.72 ± 0.54	111.02 ± 3.10		
50		308.75090	+60.1621550	9.47 ± 0.59	16.1	4.00 ± 0.68	74.27 ± 3.01		
51		308.75285	+60.1664350	9.05 ± 0.65	13.9	<0.94	86.15 ± 3.60		
52	29	308.75303	+60.1918990	48.44 ± 1.05	45.9	15.66 ± 1.44	121.43 ± 6.32	ROx	x
53		308.75399	+60.1686120	2.66 ± 0.39	6.8	<0.57	<2.46		
54	30	308.75552	+60.1499540	2.11 ± 0.48	4.4	<0.58	44.88 ± 3.34		
55	31	308.75561	+60.1393840	2.42 ± 0.53	4.5	<0.48	<1.57		
56	33	308.76587	+60.1053696	2.40 ± 0.36	6.7	<0.32	<0.86		
57	34	308.77426	+60.1318110	3.10 ± 0.62	5.0	<0.59	<2.03		
58		308.78147	+60.1666020	1.98 ± 0.37	5.3	<0.55	<2.31		
59	35	308.78390	+60.1870360	14.94 ± 0.79	18.9	<1.22	153.02 ± 7.02	Rx	x
60	36	308.78644	+60.1319640	1.41 ± 0.31	4.5	<0.36	<1.33		
61	39	308.79294	+60.1544730	4.64 ± 0.50	9.3	3.68 ± 0.60	<4.08		x
62	40	308.80002	+60.1478660	6.98 ± 0.79	8.8	3.58 ± 0.77	43.17 ± 3.79		
63		308.80126	+60.1983290	6.33 ± 0.63	10.1	<0.94	21.08 ± 4.26		
64		308.80662	+60.1707250	3.79 ± 0.43	8.9	1.81 ± 0.57	16.28 ± 2.45		
65		308.82910	+60.1899970	3.08 ± 0.46	6.7	<0.56	4.81 ± 1.61		
66	41	308.84110	+60.1152200	4.16 ± 0.58	7.1	<0.58	<2.03		
67	42	308.86008	+60.1379738	2.01 ± 0.27	7.5	<0.17	<0.76		
68	43	308.87500	+60.0885811	2.81 ± 0.43	6.5	<0.58	<1.02		
69	44	308.87766	+60.0983963	5.60 ± 0.83	6.7	<1.20	<3.25		
70	45	308.88158	+60.1872070	2.34 ± 0.30	7.9	<0.41	<1.66		
71	47	308.91010	+60.1213608	4.81 ± 0.58	8.3	1.86 ± 0.55	<1.97		
72	48	308.91873	+60.1327972	1.93 ± 0.30	6.5	<0.29	<0.92		

Note. — All reported flux errors are σ_{sky} measurement errors only. [Fe II] fluxes reported in column 5 are not continuum subtracted, they are the extinction corrected fluxes measured from the [Fe II] image. $[\mathrm{Fe\,II}]_{\mathrm{Off}}$ and H, fluxes with S/N < 3 and 2, respectively, are considered non-detections. For flux measurements considered non-detections, upper limits are reported. See Section 3.4.2 for a description of counterpart (c.p.) flags. Unpublished counterparts come from private communication about work done by F. Winkler and K. Long.

The continuum subtracted luminosities for the final 72 candidates are reported in Table 3.5, and were calculated using 5.9 Mpc as the distance to NGC 6946. The distribution of these luminosities can be seen in the log-scaled histogram displayed in Figure 3.7. This luminosity funcion has an approximate power-law slope and, more importantly, the turnover in the function indicates that our data is incomplete below a flux of about 2.85×10^{-16} erg s^{-1} cm^{-2} (corresponding a luminosity of 1.18×10^{36} erg s^{-1}). Notice from the earlier investigation of $[\mathrm{Fe\,II}]_{\mathrm{Off}}$ flux uncertainties, if the uncertainties are comparable in the $[\mathrm{Fe\,II}]_{\mathrm{Off}}$ and [Fe II] bands, then we are essentially showing inclompleteness below about $3 \times \sigma_{sys}$, and showing that we cut all objects below σ_{sys} from our final SNRc list.

In Section 3.4.1, the measured [Fe II] luminosities are used in calculating an estimated supernova rate for NGC 6946. The [Fe II] emission of the candidates is further explored in Section 3.4.2 as it relates to emission at other wavelengths for objects in NGC 6946.

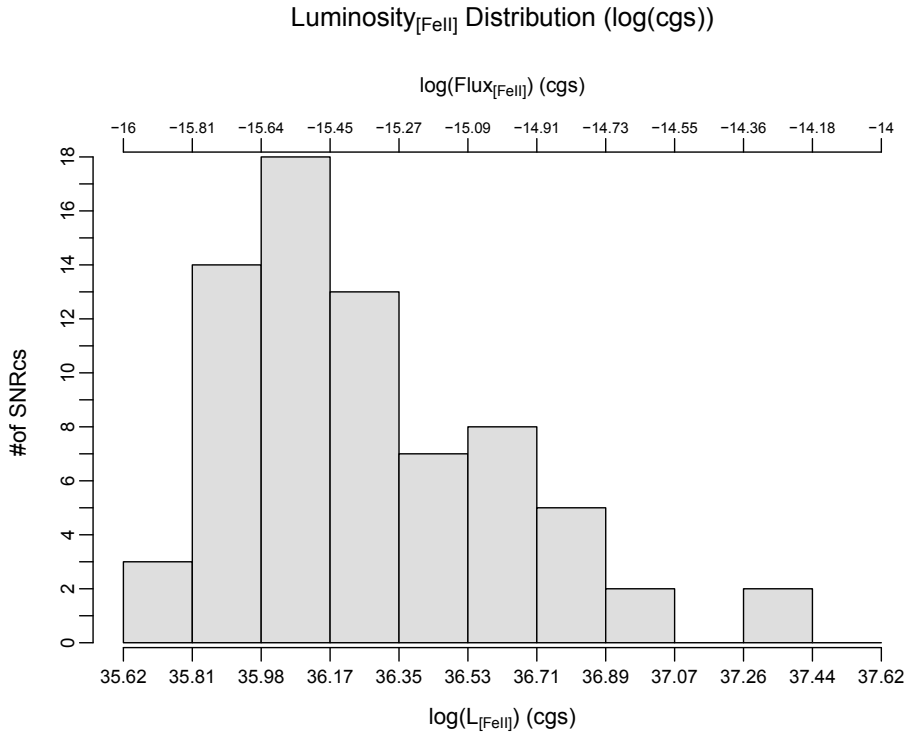

Figure 3.7 The distribution of [Fe II] Luminosities for the final 72 [Fe II] selected SNRcs is displayed in this log-scale histogram. An additional axis at the top of the graph indicates the corresponding flux values. Luminosities were calculated using 5.9 Mpc as the distance to NGC 6946.

Table 3.5. Final SNRc Luminosities.

New ID	Prev ID	$L_{[Fe\,II]}$ ($10^{33}\frac{erg}{s}$)	Alternate IDs	**New ID**	Prev ID	$L_{[Fe\,II]}$ ($10^{33}\frac{erg}{s}$)	Alternate IDs
1	1	903 ± 126		**37**		1134 ± 120	
2	2	1463 ± 159		**38**		1533 ± 157	
3	3	2365 ± 324		**39**		2381 ± 211	
4	4	1791 ± 209		**40**	22	896 ± 146	
5	5	1296 ± 194		**41**		698 ± 129	
6	6	1118 ± 175		**42**	23	1627 ± 360	
7	7	730 ± 116		**43**	24	2435 ± 391	
8	8	818 ± 119		**44**	25	3638 ± 295	MF14
9	9	3797 ± 342		**45**	26	1711 ± 268	
10	10	1974 ± 516		**46**	27	630 ± 121	
11	11	1895 ± 281		**47**		4354 ± 286	
12	12	1108 ± 148		**48**		765 ± 145	
13		1352 ± 154		**49**	28	2109 ± 240	
14		1219 ± 170		**50**		2279 ± 245	
15		1448 ± 151		**51**		3771 ± 272	
16		814 ± 144		**52**	29	13650 ± 439	LDG85 MF16 HSHP58
17		863 ± 174		**53**		1109 ± 162	
18		1294 ± 140		**54**	30	878 ± 202	
19		1380 ± 159		**55**	31	1007 ± 223	
20	14	4065 ± 206	LDG26 HSHP21	**56**	33	998 ± 148	
21	15	4299 ± 615		**57**	34	1293 ± 258	
22	16	1112 ± 213		**58**		824 ± 155	
23	17	1267 ± 185		**59**	35	6224 ± 329	LDG101 HSHP65
24		773 ± 104		**60**	36	588 ± 131	
25	18	6811 ± 495		**61**	39	402 ± 207	
26	19	1371 ± 203		**62**	40	1415 ± 329	
27		3490 ± 294		**63**		2635 ± 262	
28	20	3082 ± 363	LDG47 HSHP42	**64**		825 ± 178	
29		20883 ± 298	LDG48 HSHP43	**65**		1282 ± 191	
30		1611 ± 172		**66**	41	1732 ± 243	
31		4023 ± 419		**67**	42	838 ± 112	
32		2186 ± 268	MF10	**68**	43	1172 ± 181	
33		510 ± 106		**69**	44	2332 ± 346	
34		856 ± 103		**70**	45	976 ± 124	
35		3241 ± 162	LDG61	**71**	47	1230 ± 241	
36		4370 ± 678		**72**	48	802 ± 123	

Note. — The reported errors are σ_{sky} measurement errors. Luminosites for the new or re-imaged SNRcs (in Tables 3.2 and 3.3) were calculated using a distance of 5.9 Mpc and [Fe II]-$[Fe\,II]_{Off}$ fluxes, where $[Fe\,II]_{Off}$ is considered zero if it is reported as an upperlimit, since it is considered a non-detection. See Table 2.4 for a description of 'Alternate ID' abbreviations.

3.4.1 Estimating the SN rate for NGC 6946

In Morel et al. (2002), an intuitive estimate for calculating a galaxy's supernova (SN) rate is given as:

$$\eta = \frac{L_{[\mathrm{FeII}]tot}}{t_{[\mathrm{FeII}]} L_{[\mathrm{FeII}]}}, \tag{3.4}$$

where $L_{[\mathrm{FeII}]tot}$ is the total [Fe II] luminosity of a galaxy, $t_{[\mathrm{FeII}]}$ is the lifetime of [Fe II] emission for a SNR and $L_{[\mathrm{FeII}]}$ is a typical [Fe II] luminosity for a SNR. This quation appears in Vanzi & Rieke (1997) as well and it should be noted that this equation is presented more as an attempt to make quantitative comparisons between the SN rate and [Fe II] emission of particular galaxies, and not expected to be a definitive physical law. Keeping this in mind, we will estimate the SN rate for NGC and further investigate the parameters of Equation 3.4 in this section.

To begin with, we will adopt the very general, nominal value of $t_{[\mathrm{FeII}]} = 10^4$ yr, as is done in Morel et al. (2002) and is also generally assumed to be the approximate lifetime for significant emission from a SNR. Due to overall data quality issues in the [Fe II] mosaic, we unfortunately could not measure a value for $L_{[\mathrm{FeII}]tot}$ directly. However, since all significant sources of [Fe II] emission were visually identified, we can add them up to estimate a lower limit. Totaling all SNRcs, this value comes to $L_{[\mathrm{FeII}]SNRs}$=1.64×10^{38} erg s^{-1}. This value is generally reasonable considering the range of values for $L_{[\mathrm{FeII}]nucleus}$ for NGC 6946 by Engelbracht et al. (1996) in the range of 8.75×10^{37} - 1.92×10^{38} erg s^{-1}

However, one might consider that a diffuse component of [Fe II] exists, which Labrie & Pritchet (2006) find is 86% and 93% of the total [Fe II] emission for galaxies NGC 1569 and NGC 5253, respectively. Alonso-Herrero et al. (2003) find 80% and 70% for M82 and NGC 253, with a caveat that M82 could be as low as 30%. Another similar estimate for this value in M82 is 86%, given by Greenhouse et al. (1997). Considering these values, and the fact that these galaxies are similar in type to NGC 6946, we might expect NGC 6946's diffuse [Fe II] component to be significant as well.

To investigate this we measured the total [Fe II] emission in a small region of uniform image quality, located within the core of NGC 6946, outlined with white dashed lines in figure 3.8. This region contained 3 SNRcs, and a ratio of the total emission from these sources to the total light was measured to be 0.15. This value implies there is a diffuse component which accounts for 85% of the total [Fe II] emmision in NGC 6946, at least in the core. We might assume the diffuse [Fe II] component to be a less significant in the outer

regions of the galaxy than in the core, so we should keep in mind that using this value would provide an upper limit on η. With this in mind, $L_{[\mathrm{FeII}]tot}$=(1-.85)$^{-1}L_{[\mathrm{FeII}]SNRs}$=1.09×10^{39} erg s^{-1}.

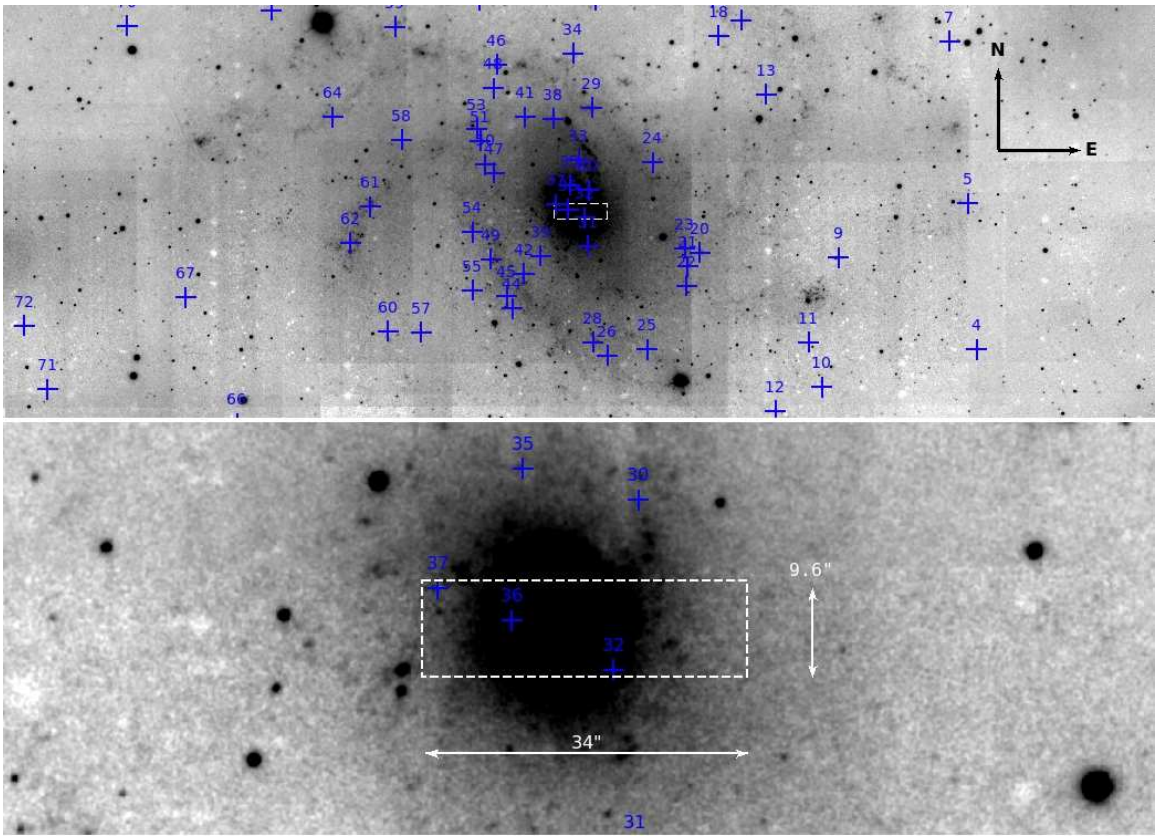

Figure 3.8 The total flux was measured within the boxed region in both the [Fe II] and [Fe II]$_{\mathrm{Off}}$ images, subtracted and then compared to the total emission from the three SNRcs located within the boxed region. Approximately 15% of the total [Fe II] emission was found to come from the SNRcs.

Finally, to choose a representative [Fe II] luminosity for typical SNRs, we can look at the distribution of [Fe II] luminosities in Table 3.5. Representing these luminosities in a 'box and whiskers' plot, Figure 3.9 displays the median value for $L_{[\mathrm{FeII}]}$ as well as statistical ranges that indicate where the majority of the data points are located within the spread of SNRc $L_{[\mathrm{FeII}]}$ values. Because of the wide range and skewed distribution of $L_{[\mathrm{FeII}]}$ values, it is illustrative to carry a few statistically significant values of $L_{[\mathrm{FeII}]}$ through our calculation of η. These values are listed in Table 3.6 where it can be seen that our median and mean values are very close to the typical galactic SNR $L_{[\mathrm{FeII}]}$=2×10^{36} erg s^{-1}, as reported by

Oliva et al. (1989).

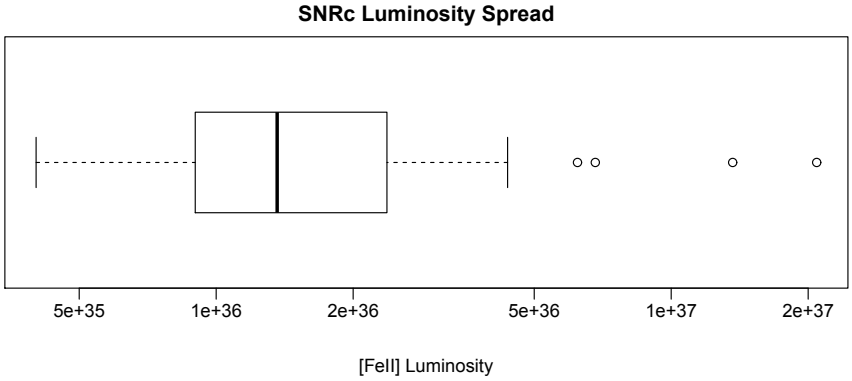

Figure 3.9 This is a box and whisker plot of the [Fe II] luminosities for the final 72 SNRcs. The thick black line represents the median $L_{[FeII]}$ value while the edges of the box represent the first and third quartile points of the data so that 50% of the data lies within the range of the box. The whiskers are meant to define the limits of the distribution outside of which, any points are considered outliers. Outliers are plotted as circles in this plot.

Arguably, the most uncertain parameter in Equation 3.4 is the representative $L_{[\text{Fe II}]}$ value, since reported [Fe II] luminosities for SNRs can vary by orders of magnitudes and are found to vary by a factor of 100 for our SNRcs alone. If we adopt values of $t_{[\text{Fe II}]} = 10^4$ yr and $L_{[\text{Fe II}]tot} = 1.09{\times}10^{39}$ erg s^{-1} as discussed above, then we can explore the range of potential SN rate values associated with the various values for $L_{[\text{Fe II}]}$ listed in Table 3.6

$L_{[\text{FeII}]}$ (erg s^{-1})	Min: $4.0{\times}10^{35}$	1st Quartile: $9.0{\times}10^{35}$	Median: $1.4{\times}10^{36}$	Mean: $2.3{\times}10^{36}$	3rd Quartile: $2.4{\times}10^{36}$	Max: $2.1{\times}10^{37}$
For $t_{[\text{FeII}]} = 10^4$ yr, $L_{[\text{FeII}]tot} = 1.09{\times}10^{39}$ erg s^{-1} :						
η (yr^{-1})	0.273	0.121	0.078	0.048	0.046	0.005
For $\eta = 0.01$ yr^{-1}, $L_{[\text{FeII}]tot} = 1.09{\times}10^{39}$ erg s^{-1} :						
$t_{[\text{Fe II}]}$) (yr)	270,000	120,000	78,000	48,000	46,000	5,200
For $\eta = 0.078$ yr^{-1}, $L_{[\text{FeII}]tot} = 1.09{\times}10^{39}$ erg s^{-1} :						
$t_{[\text{Fe II}]}$) (yr)	35,000	16,000	10,000	6,100	5,800	670

Table 3.6 Various distribution statistics for the SNRc [Fe II] luminosities are reported along with the associated SN rates or [Fe II] emission lifetimes calculated from them.

From these values, a tentative estimate for the SN rate of NGC 6946 would be η=0.078 yr^{-1}, but a more robust statement would say that η is in the range of 0.046 - 0.121 yr^{-1}.

Although lower values for SN rates are calculated for the Milky Way and other nearby galaxies in the neighborhood of 0.005 - 0.04 yr^{-1}, there is reason to believe our estimated value is reasonable. In the last century, there have been 9 observed supernovae within NGC 6946, as listed in Table 1.1. If the recent history of supernovae observations is an indication of the actual SN rate, then η would actually be $9/97 = 0.09$ yr^{-1}. From our estimates, it seems possible that the recent history of a high SN rate in NGC 6946 is not a statistical anomoly but is rather a more representative view of the SN rate over the last $\sim 10^4$ yr.

While it is possible that NGC 6946 has a particularly high SN rate, we have not really determined any of the parameters in Equation 3.4 to a high degree of certainty. It is alternatively possible that NGC 6946 has a more typical SN rate, and one of the other parameters is not as adopted in the above calculations. In that event, $t_{[\mathrm{FeII}]}$ is the most likely parameter to vary. The timescale for which a SNR emits substantial radiation would vary greatly based on local envromental parameters like density and pressure. In denser or higher pressure environments, SNRs may evolve more quickly and so would have shorter lifespans. The ranges of theorized timescales for SNR evolution vary by at least an order of magnitude based on the various assumptions that go into these calculations. Table 3.6 reports the [Fe II] emission lifetimes associated with the various possible values for $L_{[\mathrm{Fe\ II}]}$ and η in NGC 6946. If NGC 6946 has a more typical SN rate of $\eta = 0.01$ yr^{-1}, then a more typical lifespan for a SNR would be 78,000 yr.

3.4.2 Radio, optical, X-ray sources and the [Fe II] SNRcs

Tables 3.4 and 3.5 indicate SNRcs that have associated counterparts in the radio, optical and/or X-ray. In Table 3.4, two columns indicate if the SNRc has counterparts from published and/or unpublished studies. In these columns, letters r, o and x are used to indicate 'radio', 'optical' and 'X-ray' while capital letters indicate sources that have been specifically reported as SNRs. All unpublished sources are tentative SNR candidates as well. Published sources are also listed in Table 3.5 where their alternate identification numbers and associated studies are indicated.

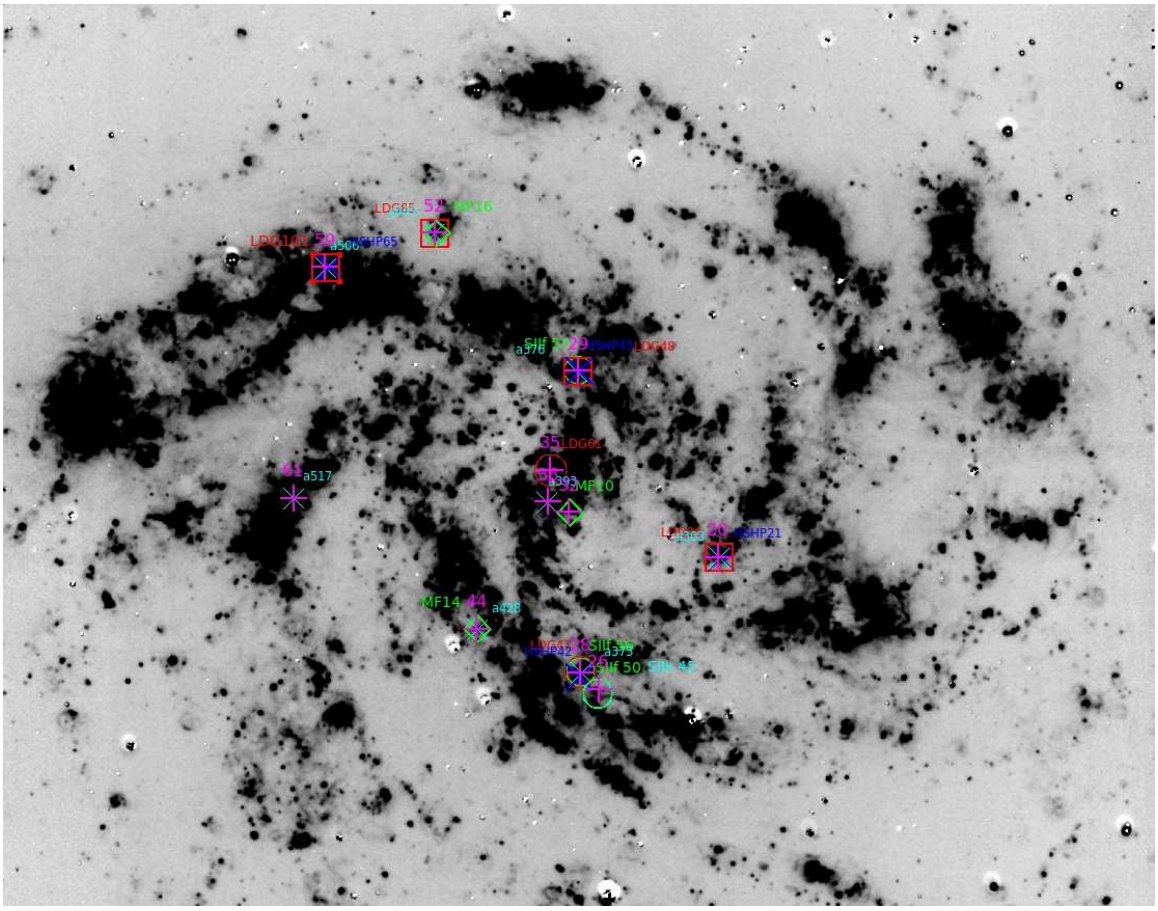

Figure 3.10 The 11 [Fe II] SNRcs which have counterparts in the radio, optical and/or X-ray are indicated here, plotted on an Hα map. In this figure, magenta crosses indicate [Fe II] SNRcs and red indicates radio (squares are specifically SNRs from Hyman et al. (2000) and Lacey & Duric (2001) while circles are other sources from Lacey et al. (1997)). Green indicates optical (diamonds are SNRs from Matonick & Fesen (1997), circles are unpublished SNRcs) cyan and blue indicate X-ray (cyan x's are unpublished tentative SNRcs, blue are sources from Holt et al. (2003)).

Eleven of the 72 [Fe II] SNRcs have counterparts, 6 of which have been specifically identified in published studies as SNRs. Figure 3.10 plots the 11 SNRcs and their associated counterparts. Figure 3.11 shows where these 11 SNRcs are located in the range of luminosities for the entire [Fe II] SNRc population. What becomes noticable from the plots in this figure is that SNRcs with counterparts appear to have significantly higher [Fe II] fluxes than the rest of the [Fe II] SNRc population. To illustrate this point, about 40% of the top 1/3$^{\rm rd}$ most [Fe II] luminous SNRcs have associated counterparts while only a few percent of the rest of the SNRcs have counterparts.

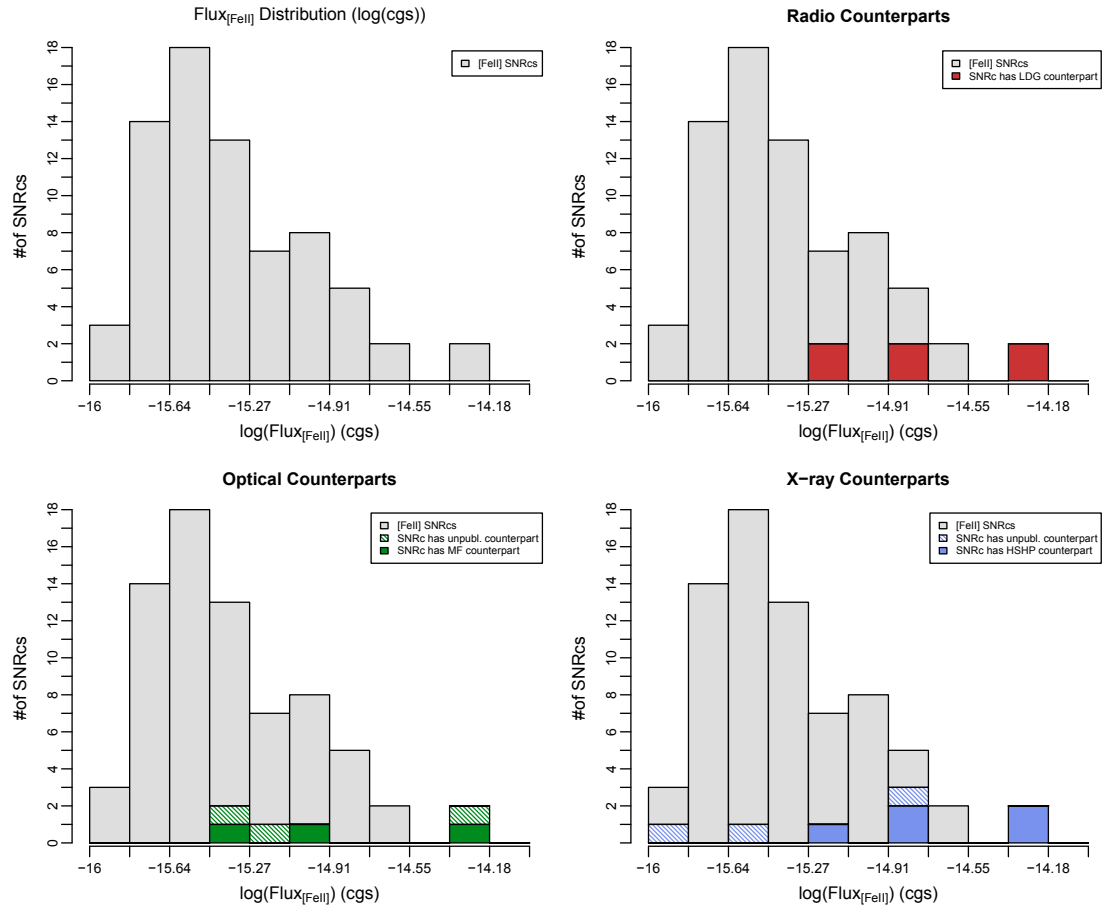

Figure 3.11 The number of [Fe II] SNRcs which have counterparts at various wavelengths are shown.

While a number of possible explanations exist for this, two particular reasons seem most plausible. We would expect any SNR to be radiating at other wavelengths as well, if it is a significant [Fe II] source. And even if the SNR was located in a dusty shrouded region, we would expect to at least see the radio emission from it. Considering this, either the radio, [S II] and X-ray emission of almost all of our faintest SNRcs is below the completeness limit of the associated studies or the emission is not there, in which case it would seem to be that it is less likely that our fainter SNRcs are actually SNRs.

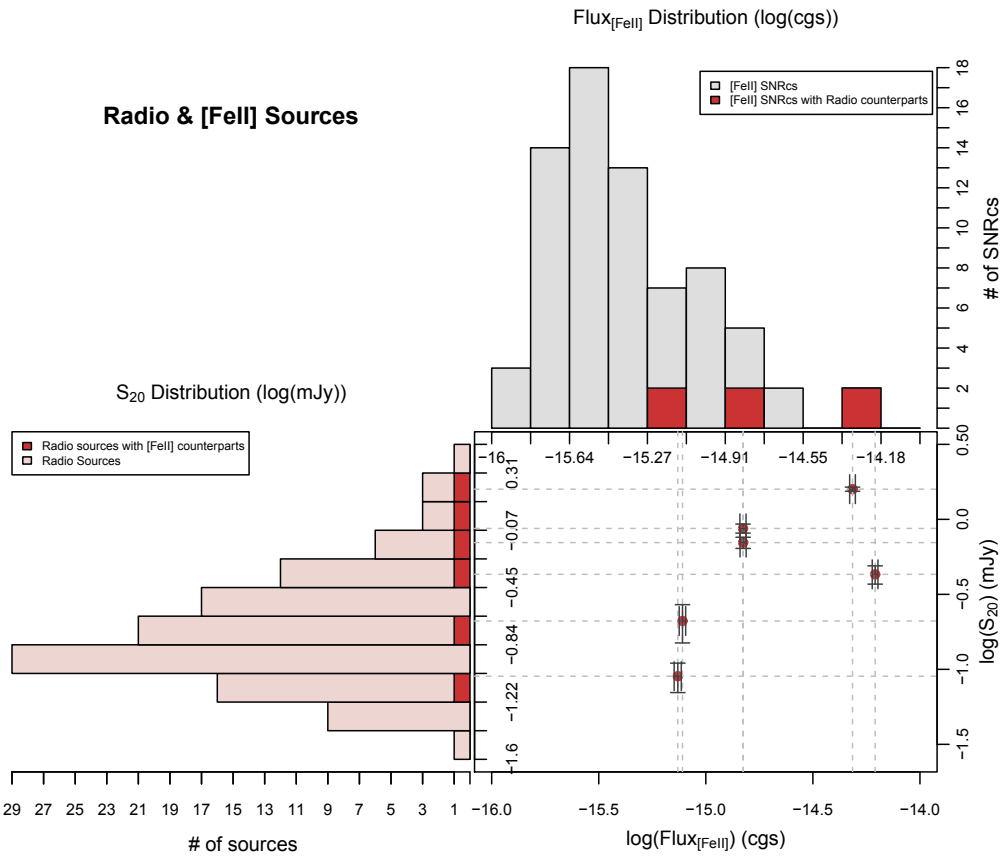

Figure 3.12 In this figure, a scatter plot displays the relationship between [Fe II] fluxes and integrated radio flux densities at 20 cm for the 6 objects which were identified to be both radio sources from Lacey et al. (1997) as well as being [Fe II] SNRcs. The histograms give context by displaying the distribution of [Fe II] fluxes for all 72 [Fe II] SNRcs (gray) as well as the flux densities for the 118 radio sources from Lacey et al. (1997) (light red). In these histograms, the bright red bars indicate the 6 objects from the scatter plot which are both radio sources and also [Fe II] SNRcs.

To further explore this subject, we can add in a comparison of how the [Fe II] flux is related to the emission at these other wavelengths and also where the SNRcs are located in the flux distributions of the published radio sources, optical SNRs and X-ray sources of NGC 6946. Figures 3.12 - 3.14 display this information for each wavelength regime. In these plots, it can be seen that the distribution of objects with [Fe II] counterparts in each of the populations examined much more closely mimics the overall distribution of all sources in the population than can be said for the inverse examination. Additionally, there may be

loose correlations between the [Fe II] flux and emission at each of the wavelengths examined. However, we are clearly working with small numbers such that these conclusions cannot be concrete.

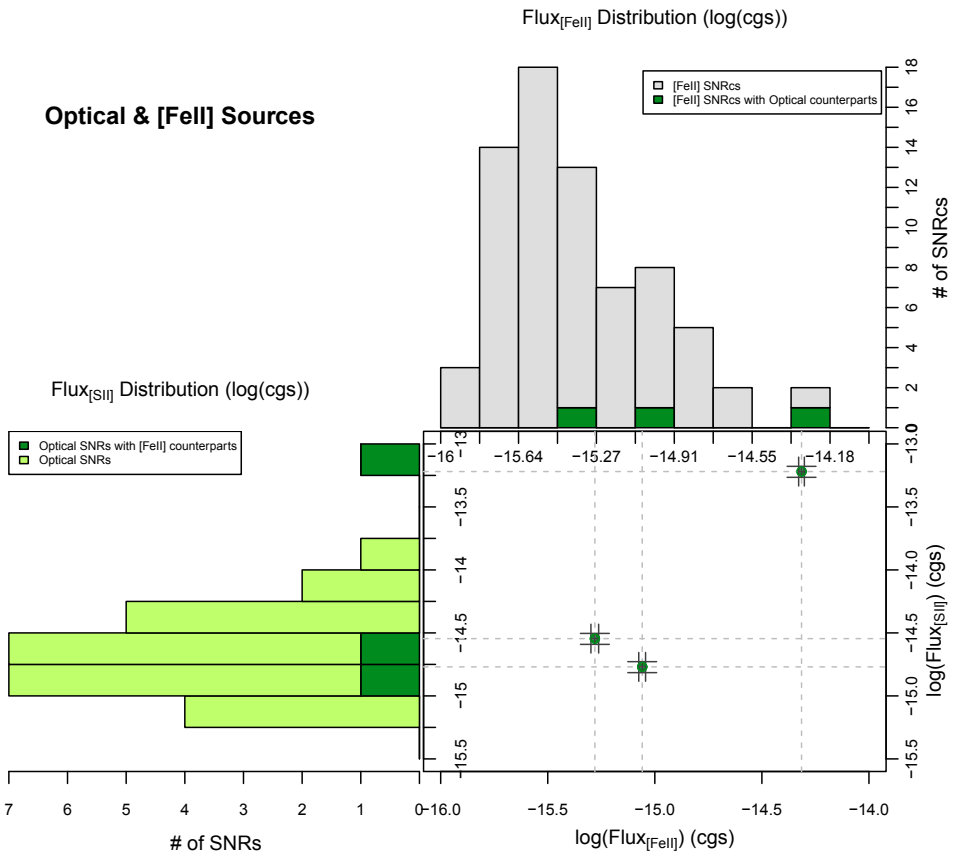

Figure 3.13 In this figure, a scatter plot displays the relationship between [Fe II] and [S II] fluxes for the 3 objects which were identified to be both optical SNRs from Matonick & Fesen (1997) as well as being [Fe II] SNRcs. The histograms give context by displaying the distribution of [Fe II] fluxes for all 72 [Fe II] SNRcs (gray) as well as the [S II] fluxes for the 27 optical SNRs from Matonick & Fesen (1997) (light green). In these histograms, the darker green bars indicate the 3 objects from the scatter plot which are both optical SNRs and also [Fe II] SNRcs.

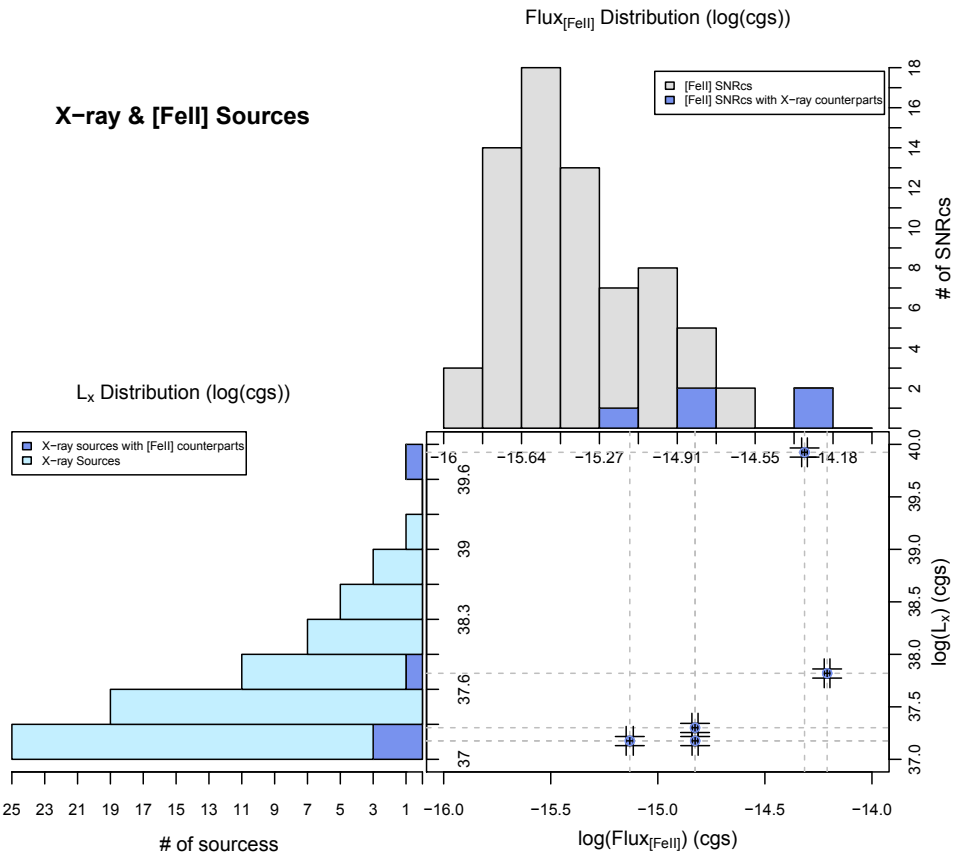

Figure 3.14 In this figure, a scatter plot displays the relationship between [Fe II] fluxes and X-ray luminosities for the 5 objects which were identified to be both X-ray sources from Holt et al. (2003) as well as being [Fe II] SNRcs. The histograms give context by displaying the distribution of [Fe II] fluxes for all 72 [Fe II] SNRcs (gray) as well as the luminosities for the 72 X-ray sources from Holt et al. (2003) (light blue). In these histograms, the dark blue bars indicate the 5 objects from the scatter plot which are both X-ray sources and also [Fe II] SNRcs.

3.4.2.1 [Fe II] SNRcs, Optical SNRs and Dust

In Figures 3.12 - 3.14, we compare only the objects that have measured fluxes for both of the plotted wavelengths. It would be informative to be able to compare the radio, optical and X-ray fluxes for all [Fe II] SNRcs, and reciprocally the [Fe II] flux for any and all radio, optical and/or X-ray SNRs or SNR candidates. To this end, we have begun a preliminary analysis of the [Fe II] emission from the optical SNRs reported in Matonick & Fesen (1997).

Of the 27 optical SNRs identified, 12 were located within our newly obtained and more deeply imaged [Fe II] mosaic. We placed uniformly sized apertures at the locations of those 12 optical SNRs and obtained measurements of the [Fe II] flux there. Figure 3.15 shows that aside from the 3 SNRcs already compared in Figure 3.13, none of the other 12 optical SNRs had detectable [Fe II] emission, and only upper limits can be plotted for those objects.

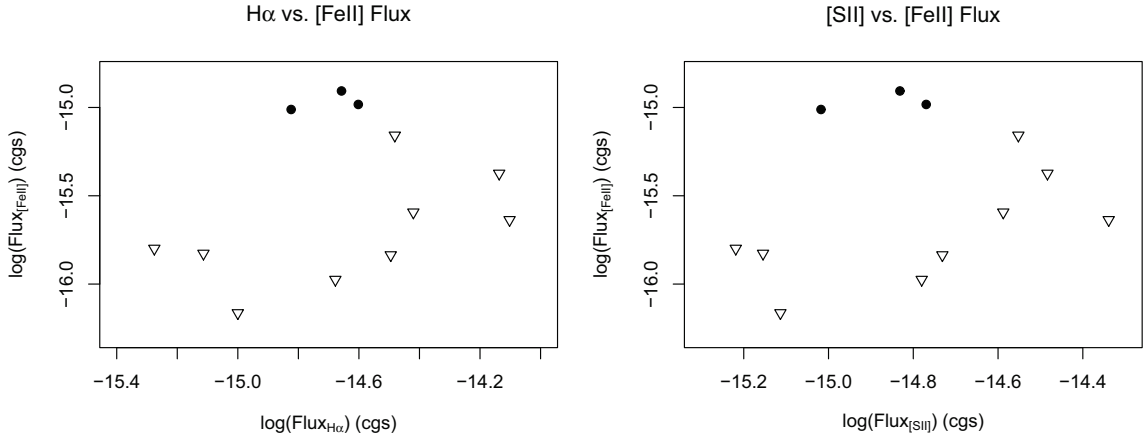

Figure 3.15 These graphs show the relationship between Hα (*left*) and [S II] (*right*) fluxes of optical SNRs versus the measured [Fe II] flux from our new WHIRC data. Solid circles indicate the 3 objects which were selected both as optical SNRs and also as [Fe II] SNRcs. Triangles indicate [Fe II] flux upper limits for optical SNRs that had a S/N < 4.4, and so were considered non-detections in [Fe II].

It is of most obvious interest to ask why we don't see many of the optical SNR candidates from Matonick & Fesen (1997) emitting significant [Fe II] emission, or, on the other hand, why Matonick & Fesen did not detect many of the [Fe II] SNRcs. To help understand this issue, Figure 3.16 shows the position of [Fe II] and [S II] selected SNRcs on an 8 μm map. Figure 3.17 shows the same 8 μm map colored in red with additional green showing visual emission at 5500 Å, both images were obtained as part of The Spitzer Infrared Nearby Galaxies Survey (SINGS) (Kennicutt et al. 2003). Both the 8 μm and 5500 Å images are useful in determining the location of dust lanes in NGC 6946.

A sample analysis was completed with the field shown in Figures 3.16 and 3.17. This field contains 41 [Fe II] selected SNRcs (indicated with crosses), 5 of which have either published or unpublished [S II] counterparts (marked specially as green crosses). The field also contains 13 of the optically selected SNRs from Matonick & Fesen (1997), indicated with white diamonds.

Blue circles were put around the [Fe II] SNRcs which were determined to lie in dusty regions, while green circles indicate SNRcs that were not in dusty regions. Based on this assessment, we find over 70% of the [Fe II] SNRcs with no optical counterparts are located in dusty regions. Conversely, only 20% of the [Fe II] SNRcs which have optical counterparts are confirmed to lie in dusty regions. Thus dust extinction may be limiting the [S II] emission from many of our SNRcs.

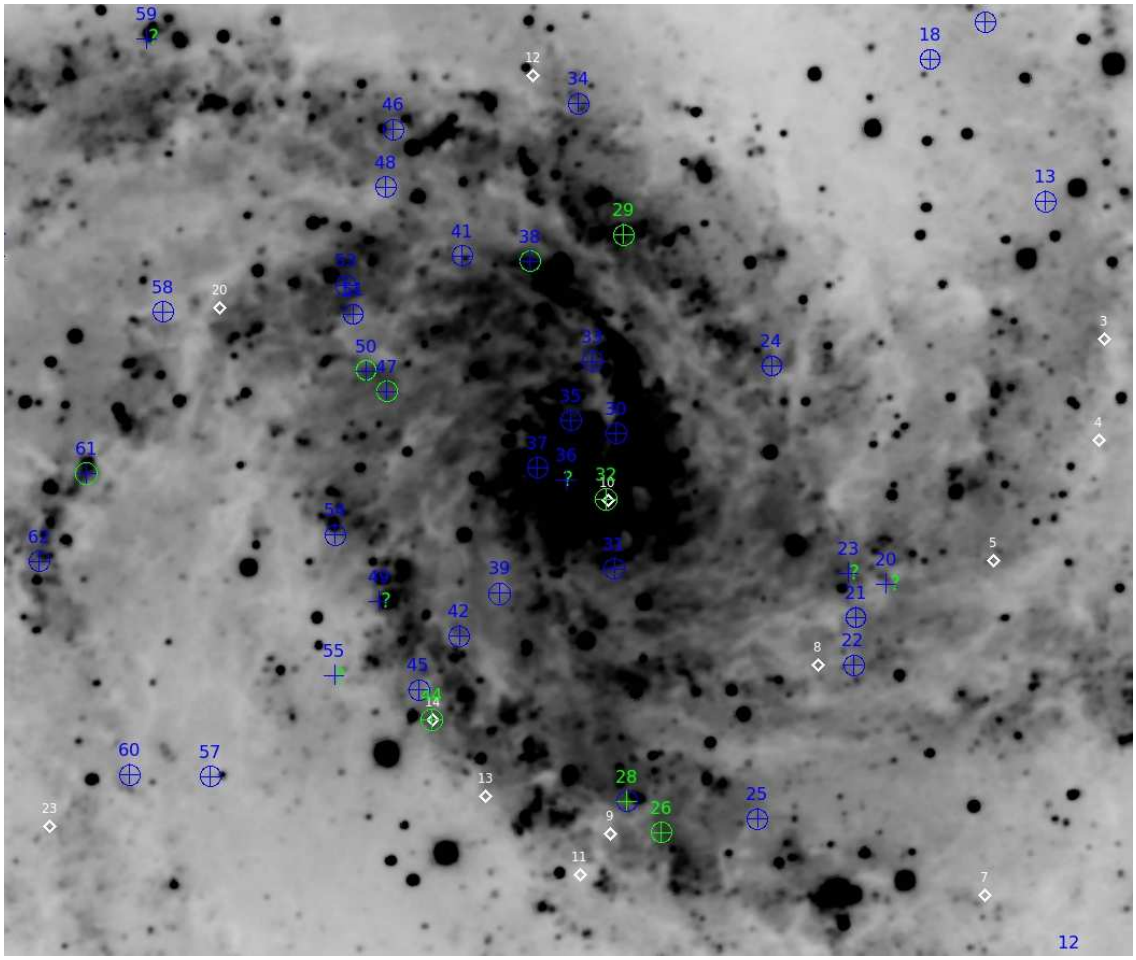

Figure 3.16 Above, crosses indicate 41 central [Fe II] selected SNRcs, 5 of which (colored green) have optically identified SNR or SNRc counterparts. The white diamonds indicate 13 of the 27 optical SNRs from Matonick & Fesen (1997). These are superimposed on a map of emission at 5500 Å (Kennicutt et al. 2003). By analyzing this map, blue circles were placed around [Fe II] SNRcs that appeared to be in dust lanes while green circles were paced around the [Fe II] SNRcs which appeared in regions of visual emission. Six question marks indicate SNRcs in ambiguous regions.

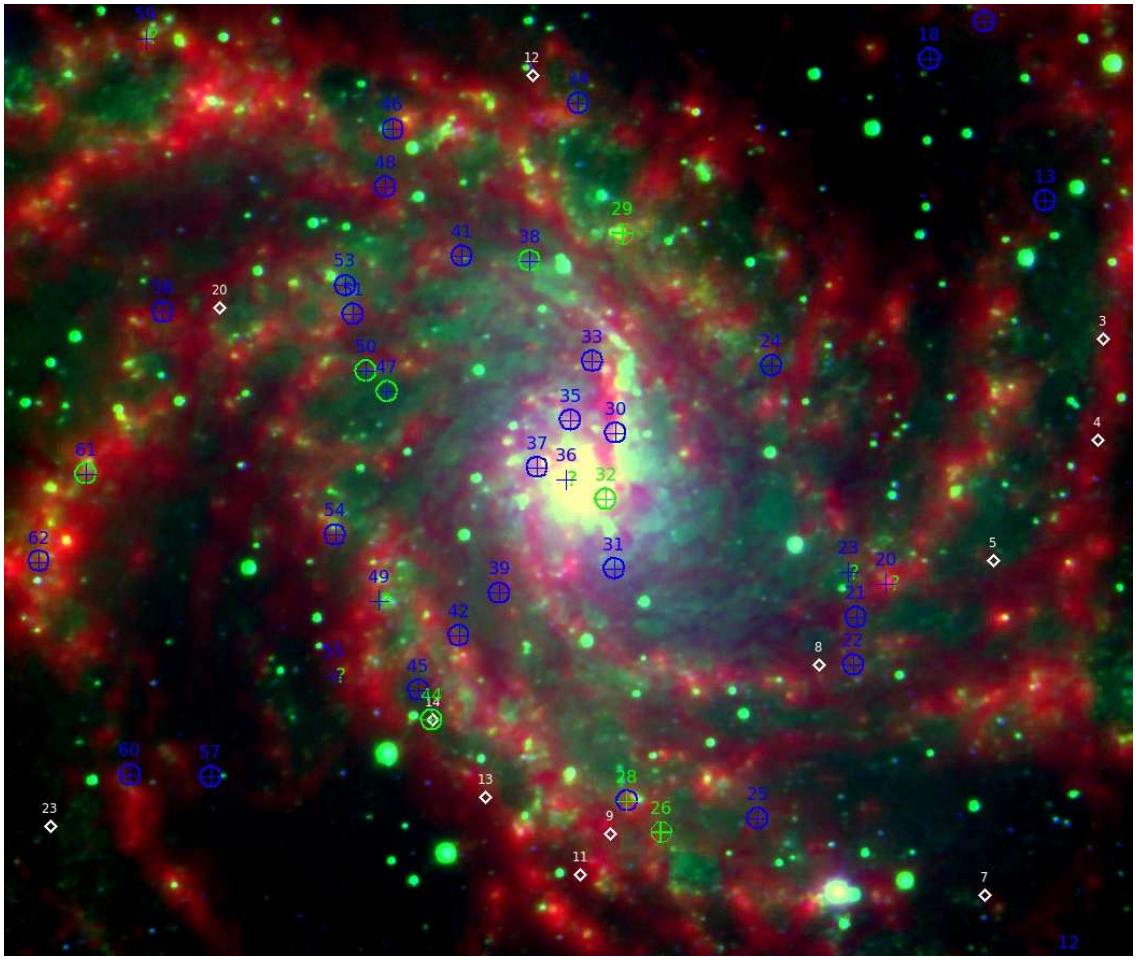

Figure 3.17 This figure is a two-color image where green shows the same 5500 Å emission as in Figure 3.16 while red indicates 8 μm emission, both images are from SINGS (Kennicutt et al. 2003). The circles, crosses and diamonds are as explained in the caption of Figure 3.16. Many of the [Fe II] SNRcs (more tha 70% of them) can be seen to be associated with red regions as opposed to green, thus are seen to lie in dusty areas.

3.5 Summary and Conclusions

We obtained new [Fe II] imaging of NGC 6946 with the WHIRC on the WIYN 3.5 m telescope to add to and verify the results from our initial investigation discussed in Chapter 2. Of the 13 originally identified SNRcs within our test field region, 10 were confirmed as valid [Fe II] SNRcs as per our criteria. This may indicate that the SNRcs with the lowest measured [Fe II] S/N are perhaps less reliable than those with higher S/N values.

[Fe II] flux measurements from the new images correlate well with those from the old imaging, which helps support the idea that despite questions of image quality, our flux measurements were and are largely accurate. We were able to identify 30 new [Fe II] SNRcs, however 6 of our previously identified candidates were eliminated and so our final list contained 72 [Fe II] SNRcs.

The [Fe II] luminosities for the 72 SNRcs ranged from 4.02×10^{35} to 2.09×10^{37} erg s^{-1}. The turn-over in the luminosity function indicates we are complete for SNRs down to a [Fe II] luminosity of about 1.18×10^{36} erg s^{-1}. Using the median $L_{[\mathrm{FeII}]}$ from our SNRc list as a representative value for a SNR's [Fe II] emission together with an estimate of the total [Fe II] luminosity for NGC 6946, we calculate a tentative SN rate to be $\eta = 0.078$ yr^{-1}. This supports the idea that NGC 6946 has an unusually high SN rate as is implied by the last century of astronomical observations that yield a measured rate of 0.09 yr^{-1}. However, if the SN rate of NGC 6946 is a more typical value such as $\eta = 0.01$, then that might imply that the the typical [Fe II] emission lifetime of a SNR is $\sim$ 78,000yr which is perhaps on the longer end of theorized lifespans.

11 of our 72 SNRcs have associated counterparts from radio, optical and/or X-ray studies, 6 of which were officially published as either radio or optical SNRs. We compared the radio, optical, [Fe II] and X-ray emission of these 11 sources and then compared their emission to the other objects found in each wavelength regime. Nearly none of the SNRcs in the bottom 2/3$^{\mathrm{rds}}$ of the [Fe II] flux distribution had conterparts, while $\sim$ 40% of the top 1/3$^{\mathrm{rd}}$ did have counterparts. This either implies that the associated radio, optical and/or x-ray fluxes for our fainter SNRcs are below the completeness limits of those associated studies, or that it is less probable that our fainter SNRcs are actually SNRs. There may be a loose correlation between the [Fe II] flux and emission at each of the wavelengths examined, however small number statistics prevent us from determining the strength of any such correlation.

An attempt to measure the fluxes for sources identified as optical SNRs by Matonick & Fesen (1997) was inconclsuive, but a visual inspection of optical and [Fe II] sources in relation to dust lanes indicates that a large number of the [Fe II] SNRcs are in dusty regions. Thus, dust is likely playing a role in diminishing the optical emission of many of the [Fe II] SNRcs. Continuing this analysis further in future studies could be invaluable to our understanding of NGC 6946, SNRs and the ISM. An ideal object for further study, NGC 6946 now has 66

new [Fe II] SNRcs independent from the 60 previously published optical and radio SNRs. These 126 SNRcs are shown in Figure 3.18. The connection between the emission from SNRs at different wavelengths is still poorly understood but investigating these 126 SNRcs with a multi-wavelength approach will most surely shed light on the matter.

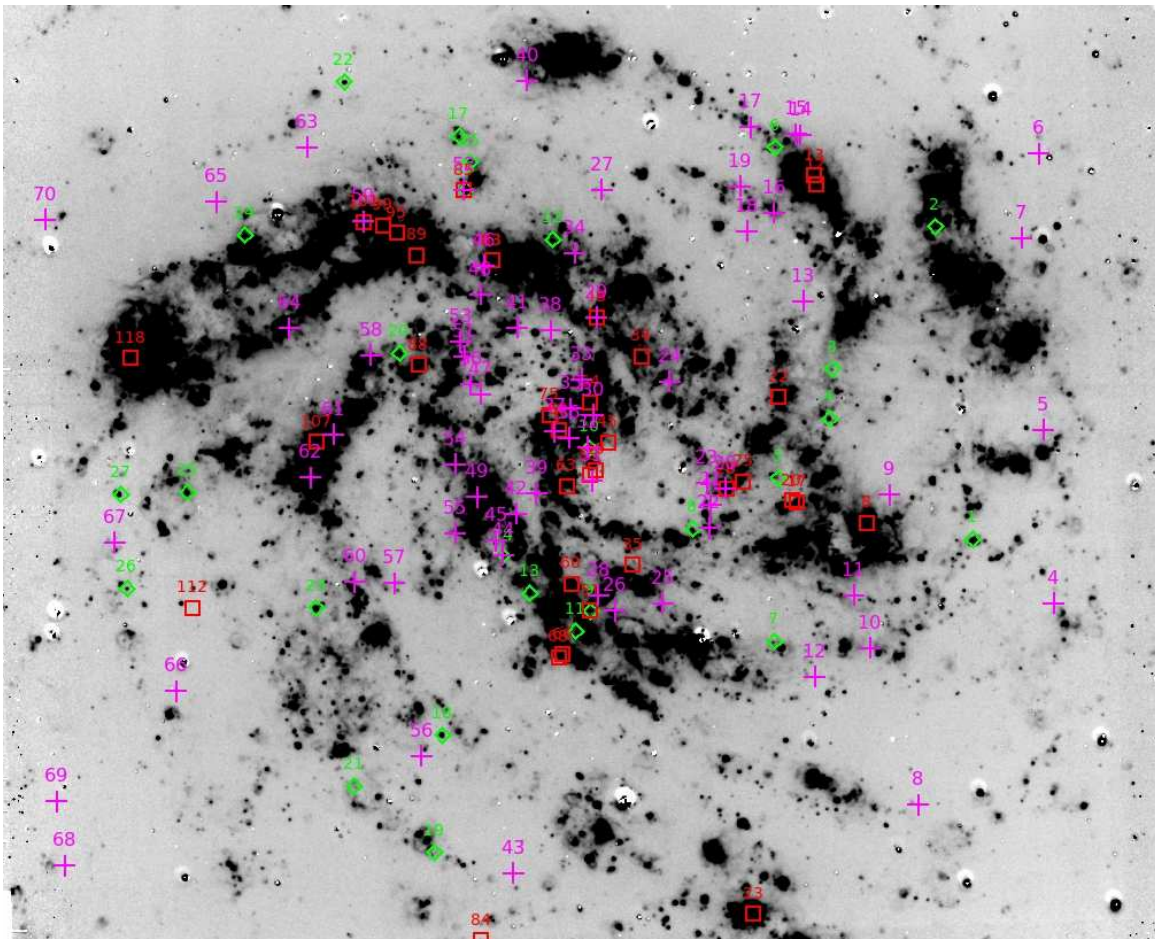

Figure 3.18 In this figure, magenta crosses mark the locations of our 72 final [Fe II] SNRcs, red squares show the locations of 35 radio identified SNRs from Hyman et al. (2000) and Lacey & Duric (2001) while green diamonds indicate optical SNRs from Matonick & Fesen (1997).

Chapter 4

Concluding Remarks

The main aim of this thesis was to identify and present a list of new SNR candidates (SNRcs) in NGC 6946 found using [Fe II] emission. Specifically, our method employed a new technique of measuring the continuum emission within the [Fe II] filter by using a specially designed narrowband $[\mathrm{Fe\,II}]_{\mathrm{Off}}$ filter adjacent to the [Fe II] band. Chapter 2 of this thesis reported the results of the initial investigation of this method and the initial list of SNRcs as was published in Bruursema et al. (2014). Chapter 3 described the follow-up observations that were taken in order to better understand the results and fill in gaps of the original study.

In the initial analysis described in Chapter 2, 48 SNRcs were identified within NGC 6946. However there was a clear difficulty in identifying candidates in the northern part of the galaxy and so this region was re-imaged which ultimately yielded a total of 72 [Fe II] SNRcs. Aside from the slight difference in luminosity ranges between the original 48 candidates and the final 72 candidates, all the conclusions drawn in Chapter 2 remain valid or were further supported by the second analysis.

These conclusions include the observation that the [Fe II] SNRcs of NGC 6946 generally had the point-like appearance we expected assuming most SNRs would have diameters less than about 40 pc. Also, the candidates largely trace the spiral arm structure of the galaxy, appearing to be associated with the denser, more active regions. Additionally, the spatial distribution of our candidates is qualitatively similar to the types of distributions for SNRcs found through different wavelength searches both within NGC 6946 and in galaxies such as M33 and M83.

From the final SNRc list in Chapter 3, the [Fe II] luminosities for our 72 SNRcs ranged from 4.02×10^{35} to 2.09×10^{37} erg s^{-1}, where we were complete down to a luminosity of 1.18 $\times10^{36}$ erg s^{-1}. This range indicates that our SNRcs have some of the highest measured [Fe II] luminosities, especially as compared to galactic SNRs. However the luminosity range is consistent with measurements found in other nearby starburst galaxies.

Using the measured [Fe II] luminosities for the SNRcs, we were able to explore the possible supernova (SN) rate of NGC 6946. Through our analysis, we estimated a rate of $\eta = 0.078$ yr^{-1} which supports the observational evidence that NGC 6946 has a higher SN rate than average (where the measured rate has been 0.09 yr^{-1} for the last 100 yrs). However, if we alternatively assume a more typical SN rate of 0.01 yr^{-1}, then we would have to estimate that the typical lifespan for SNRs in NGC 6946 is higher than is generally theorized, and would be $\sim$ 78,000 yr.

In all, 11 of our 72 [Fe II] SNRcs had identifiable counterparts from radio, optical and/or X-ray studies. Six of these 11 were specifically identified as SNRs in prior publications. Investigations into the emission of sources at these various wavelengths indicate that the faintest 2/3$^{\rm rds}$ of our [Fe II] SNRcs either have radio, optical and/or X-ray emission levels below the completeness limit of the previous associated studies, or perhaps are less likely to be actual SNRs. The former of these options helps support the observation that a loose correlation may exist between the [Fe II] emission and the emission at these other wavelengths. However, environmental factors will certainly contribute to a significant scatter such relationships as indicated by our finding that a large number of our SNRcs are clearly associated with the dustier regions of the galaxy.

We are confident that sources in our [Fe II] SNRc list are SNRs, however spectroscopic observations are needed to confirm this classification. Certainly, our brighest candidates are very likely to be SNRs, and in fact, 25% of the top 1/3$^{\rm rd}$ most luminous candidates have previously published counterparts that are specifically classified as SNRs through optical and/or radio studies. Our [Fe II] SNRcs were found in a blind search, using no a priori knowledge of the location of previously identified SNRs, so it is clear that our [Fe II] method is an effective way to identify SNRcs.

Bibliography

Alonso-Herrero, A., Rieke, G. H., Rieke, M. J., & Kelly, D. M. 2003, AJ, 125, 1210

Belley, J., & Roy, J.-R. 1992, ApJS, 78, 61

Blair, W. P., Winkler, P. F., & Long, K. S. 2012, ApJS, 203, 8

Bruursema, J., Meixner, M., Long, K. S., & Otsuka, M. 2014, AJ, 148, 41

Burton, M., & Spyromilio, J. 1993, Proceedings of the Astronomical Society of Australia, 10, 327

Carignan, C., Charbonneau, P., Boulanger, F., & Viallefond, F. 1990, A&A, 234, 43

Carpenter, J. M. 2001, AJ, 121, 2851

Cedrés, B., Cepa, J., Bongiovanni, Á., et al. 2012, A&A, 545, A43

Cedrés, B., Cepa, J., Bongiovanni, Á., et al. 2013, A&A, 560, A59

Dunne, B. C., Gruendl, R. A., & Chu, Y.-H. 2000, AJ, 119, 1172

Engelbracht, C. W., Rieke, M. J., Rieke, G. H., & Latter, W. B. 1996, ApJ, 467, 227

Evans, I. N., Primini, F. A., Glotfelty, K. J., et al. 2010, ApJS, 189, 37

Forbes, D. A., & Ward, M. J. 1993, ApJ, 416, 150

Gordon, S. M., Duric, N., Kirshner, R. P., Goss, W. M., & Viallefond, F. 1999, ApJS, 120, 247

Graham, J. R., Wright, G. S., & Longmore, A. J. 1989, Infrared Spectroscopy in Astronomy, 290, 169

Graham, J. R., Wright, G. S., & Longmore, A. J. 1990, ApJ, 352, 172

Greenhouse, M. A., Woodward, C. E., Thronson, H. A., Jr., et al. 1991, ApJ, 383, 164

Greenhouse, M. A., Satyapal, S., Woodward, C. E., et al. 1997, ApJ, 476, 105

Gusev, A. S., Sakhibov, F. H., & Dodonov, S. N. 2013, Astrophysical Bulletin, 68, 40

Holt, S. S., Schlegel, E. M., Hwang, U., & Petre, R. 2003, ApJ, 588, 792

Hyman, S. D., Lacey, C. K., Weiler, K. W., & Van Dyk, S. D. 2000, AJ, 119, 1711

Itoh, H., & Masai, K. 1989, MNRAS, 236, 885

Jarrett, T. H., Rho, J., Reach, W., & Appleton, P. 2008, Galaxies in the Local Volume, 163

Karachentsev, I. D., Sharina, M. E., & Huchtmeier, W. K. 2000, A&A, 362, 544

Keller, L. D., Jaffe, D. T., Pak, S., Luhman, M. L., & Claver, C. F. 1995, Revista Mexicana de Astronomia y Astrofisica Conference Series, 3, 251

Kennicutt, R. C., Jr., Armus, L., Bendo, G., et al. 2003, PASP, 115, 928

Kennicutt, R. C., Jr., Hao, C.-N., Calzetti, D., et al. 2009, ApJ, 703, 1672

Kokusho, T., Nagayama, T., Kaneda, H., et al. 2013, ApJ, 768, L8

Labrie, K., & Pritchet, C. J. 2006, ApJS, 166, 188

Lacey, C., Duric, N., & Goss, W. M. 1997, ApJS, 109, 417

Lacey, C. K., & Duric, N. 2001, ApJ, 560, 719

Larsen, S. S., Efremov, Y. N., Elmegreen, B. G., et al. 2002, ApJ, 567, 896

Lee, H.-G., Moon, D.-S., Koo, B.-C., Lee, J.-J., & Matthews, K. 2009, ApJ, 691, 1042

Li, Y., Crocker, A. F., Calzetti, D., et al. 2013, ApJ, 768, 180

Long, K. S., Blair, W. P., Kirshner, R. P., & Winkler, P. F. 1990, ApJS, 72, 61

Long, K. S., Blair, W. P., Winkler, P. F., et al. 2010, ApJS, 187, 495

Magnier, E. A., Bomans, D., Chu, Y.-H., et al. 1995, Bulletin of the American Astronomical Society, 27, 1348

Mathewson, D. S., & Clarke, J. N. 1973, ApJ, 180, 725

Matonick, D. M., & Fesen, R. A. 1997, ApJS, 112, 49

Meixner, M., Smee, S., Doering, R. L., et al. 2010, PASP, 122, 451

Morel, T., Doyon, R., & St-Louis, N. 2002, MNRAS, 329, 398

Mouri, H., Kawara, K., & Taniguchi, Y. 2000, ApJ, 528, 186

Oliva, E., Moorwood, A. F. M., & Danziger, I. J. 1989, A&A, 214, 307

Pannuti, T. G., Duric, N., Lacey, C. K., et al. 2000, ApJ, 544, 780

Rho, J., Reach, W. T., Koo, B.-C., & Cambresy, L. 2001, Young Supernova Remnants, 565, 197

Rosenberg, M. J. F., van der Werf, P. P., & Israel, F. P. 2012, A&A, 540, A116

Schlafly, E. F., & Finkbeiner, D. P. 2011, ApJ, 737, 103

Schlegel, D. J., Finkbeiner, D. P., & Davis, M. 1998, ApJ, 500, 525

Vanzi, L., & Rieke, G. H. 1997, ApJ, 479, 694

Vink, J. 2012, A&A Rev., 20, 49

Weiler, K. W., & Sramek, R. A. 1988, ARA&A, 26, 295

Woltjer, L. 1972, ARA&A, 10, 129

Vita

Justice Elisha Bruursema was born November 22, 1981 at RAF Lakenheath, England. Growing up in the midwest, she attended various schools in Missouri, Kansas and Nebraska and graduated summa cum laude from Marian High School (Omaha, NE) in May of 2000 where, in 1999, she had received an AAPT award for outstanding Physics Student of the Year.

She attended college at Arizona State University in Tempe, AZ where she completed a B.S. in Physics with an emphasis in Astronomy and also graduated through the Barrett Honors College where the title of her honors thesis was "Why Janey Can't Read Equations: An investigation of gender and physics at AS". While at ASU, Justice was awarded and supported by a number of scholarships, not the least of which were the ASU NASA Space Grant (2004) and the Stotzel Outstanding Senior Award (2004) for high achievement in the Physics Department. She served as the ASU Society of Physics Students President for the 2002-03 school year and was also awarded Teaching Assistant positions in physics classes during her last two years at ASU. She graduated in December of 2004, summa cum laude, and was appointed the college convocation speaker for the College of Liberal Arts and Sciences.

Justice began her graduate education in the fall of 2006, joining the Henry A. Rowland Department of Physics and Astronomy at The Johns Hopkins University in Baltimore, MD. She served as a teaching assistant while completing classes for her masters, and was awarded her Masters of Arts in Physics and Astronomy in 2009. In the following years, while working on various research projects in her PhD program, she served positions from 2009 to 2012 as the Graduate Representative Organization (GRO) Diversity Coordinator and GRO Guide Editor, and was involved in a number of outreach and education programs including serving as an astronomy instructor for the Center for Talented Youth at JHU in 2010. In 2014, she was awarded her PhD in Physics and Astronomy from JHU for her thesis work on using [Fe II] emission to search for supernova remnants in the starburst galaxy NGC 6946 under the supervision of Dr. Margaret Meixner (Space Telescope Science Institute).